Measurement of Transport Coefficients in Electrolytes applying Electrochemical Impedance Spectroscopy

Von der Fakultät für Maschinenbau
der Gottfried Wilhelm Leibniz Universität Hannover
zur Erlangung des akademischen Grades
Doktor-Ingenieur
Dr.-Ing.
genehmigte Dissertation

von
Dipl.-Ing. Pablo Radici

2022

Gedruckt bzw. veröffentlicht mit Unterstützung des Deutschen Akademischen Austauschdienstes (DAAD).

1. Referent: Prof. Dr.-Ing. Stephan Kabelac
2. Referentin: Prof. Dr.rer.nat. Cornelia Breitkopf
Tag der Promotion 27.04.2022

Affidavit

I hereby confirm that my thesis is the result of my own work. I did not receive any help or support from commercial consultants. All sources and/or materials used are listed and specified in the thesis.
Furthermore, I confirm that this thesis has not yet been submitted as part of another examination process neither in identical nor in similar form. Moreover, I confirm that parts of this thesis have been already published as:

- Manuscript at the peer-reviewed Journal *Solid State Ionics* with the title *A novel method to determine the transport coefficients of an YSZ electrolyte based on impedance spectroscopy.*
- Oral presentation at the national conference *DECHEMA Themodynamik Kolloquium 2021* with the title *Charakterisierung von Polymerelektrolytmembranen mittels Impedanz Spektroskopie unter Berücksichtigung der Thermodynamik irreversibler Prozesse*

Nevertheless, this thesis is not a cumulative dissertation.
Additionally, I confirm that I have not submitted any doctoral thesis previously.

Garbsen, August 5, 2022,

Pablo Radici

Acknowledgements

This thesis is the result of my four years as a research assistant at the Institute of Thermodynamics from the Leibniz University Hannover. In the first place I would like to thank Prof. Dr.-Ing. S. Kabelac for the opportunity to work at the Institute, his continuous guidance and fruitful scientific discussion, which made me grow enormously as a person as well as academically. In the same line, sincere thanks to the German Academic Exchange Service (DAAD), who funded my research; without their support this would have never been possible. I am sincerely grateful to my colleagues and friends Tobi, Vala and Jan for their support to my work, their generous contribution to my research and their patience while introducing me to the pillars of this thesis, Non-Equilibrium Thermodynamics and Impedance Spectroscopy. My work was possible thanks to my former students Nele, Maxi, Torben and Mohamed, who helped me developing the model and carrying out some measurements. Many thanks as well to all the colleagues who joined me on this four years journey from the beginning: Anja, Ruben, Max, Benny and the ones that got on board later on: Aydan, Marco, Conrad, Maike, Stegi, Robin and Sebastian. Without their comradeship it would have been unbearable. In the same line, the work carried out by Uwe and Karsten from the workshop made my experiments possible. Just as significant has been the support from my friends Steven, Kim, Basti and Christopher, remembering me taking a break from work. Over twelve thousand kilometres away a group of people guided me through thick and thin: my dearest friends Celi, Mauro, Cami, Pauli, Javi, Lia, Jose, Dana, Mari, Maca and Pedri: thanks for your friendship and nurturing my soul in the hardest times. A warm thanks to my beloved family, my siblings Mari, Cele and Juan, especially my parents, Hugo and Mirta, who have been always there for me and supported me no matter how crazy my ideas were, as well as my grandparents Hugo, Lili and Neri, and my godparents Mariana and Carlos, who cheered me up for every little step I took since I can remember. Equally important to me has been the support of my life partner, Fer, who encouraged me when I needed it the most: thanks for always being there and for your selfless love. Finally, I dedicate this thesis to my biggest fan of all, the one that never doubt me: grandma, wherever you are, you took a piece of me with you.

Zusammenfassung

Brennstoffzellen werden eine Schlüsselrolle bei der Etablierung einer emissionsfreien Energiematrix spielen. Der Elektrolyt ist Herz und Seele einer Brennstoffzelle; der Bestandteil, der ihre Funktion ermöglicht, aber auch ihre höchsten Verluste verursacht.
Elektrolyte wurden bisher fast ausschließlich mittels monokausaler klassischer Modelle untersucht und charakterisiert, z.B. durch das Ohmsche und Ficksche Gesetz. Diese Ansätze haben sich im Vergleich zu experimentellen Daten als teilweise, wenn auch nicht vollständig, unbefriedigend erwiesen. Eine alternative Beschreibung ist der multikausale Ansatz , der als Nichtgleichgewichts-Thermodynamik bekannt ist, wie er vom Physik-Nobelpreisträger Lars Onsager entwickelt wurde. Es hat sich gezeigt, dass der Ansatz zu einer höheren Übereinstimmung zu experimentellen Daten von Membranprozessen wie z.B. bei PEM-Brennstoffzellen führt.
In dieser Arbeit wurden die Elektrolytmaterialien von zwei kommerziell etablierten Brennstoffzellentypen untersucht: der oxidkeramischer Elektrolyt und der Polymerelektrolyt. Für beide Elektrolyte wurde je ein Nichtgleichgewichts-Modell entwickelt, deren definierte Transportkoeffizienten mit Hilfe der elektrochemischen Impedanzspektroskopie experimentell bestimmt werden. Dies stellt einen neuartigen Ansatz dar.
Ein Hoch- und ein Niedertemperaturprüfstand wurden dahingehend modifiziert, den zu prüfenden Elektrolyten Temperatur- und Konzentrationsgradienten aufzuprägen. Hieraus ergibt sich eine Kopplung der Transportprozesse, die die experimentelle Bestimmung der Transportkoeffizienten ermöglicht.
Die Messungen des oxidkeramischen Elektrolyten zeigten große Abweichungen gegenüber Literaturwerten, sodass nur eine qualitative Aussage möglicht ist. Der Ionentransportkoeffizient wurde bestimmt und der gekoppelte Transportkoeffizient wurde angenähert. Mögliche Verbesserungen zur Erhöhung der Zuverlässigkeit der Messungen und des Prüfstands wurden vorgeschlagen.
Die Charakterisierung des Polymerelektrolyten erwies sich aufgrund der Kopplung zwischen den Transportvorgängen des Elektrolyten und des Gasdiffusionsmediums als noch

anspruchsvoller. Darüber hinaus konnte eine Störeinkopplung des Prüfstands in die Messstrecke nicht verhindert werden, wodurch die Aussagekraft der Messungen verringert wurde. Die Ionenleitfähigkeit wurde direkt aus Impedanzspektren berechnet, während die gekoppelten Koeffizienten aus den Steigungen etablierter Kurven angenähert wurden. Die Ergebnisse wurden mit Literaturwerten verglichen, die aus monokausalen Modellen geschätzt wurden.

Keywords: Brennstoffzellen, Electrolyte, Polymerelektrolytmembran, Yttriumoxid stabiliziertem Zirkoniumdioxid, Electrochemische Impedanzspektroscopie, Thermodynamik irreversibler Prozesse.

Abstract

Fuel cells shall play a key role in the transition and establishment of a emission free energy matrix. The electrolyte is the heart and soul of a fuel cell, being the component that makes possible their functioning but also causing their highest losses.
Electrolytes have been studied and characterised up to date almost exclusively by means of mono-causal classical models, e.g. Ohm's Law and Fick's Law. These approaches have proved to be partially, when not entirely, unsatisfactory when compared to experimental data. Therefore it is proposed to study and measure the transport processes taking into consideration a multi-causal approach, known as Non-Equilibrium Thermodynamics, as proposed by the Nobel prize award physicist Lars Onsager. The approach has been proved to fit better experimental data of membrane processes, as e.g. in PEM fuel cells.
The two widespread types of fuel cells have been considered, so that two electrolytes were subject to investigation: the solid oxide electrolyte and the polymer electrolyte.
Both electrolytes were investigated in terms of Non-Equilibrium Thermodynamics. Models were developed to experimentally determine the transport coefficients defined by this theory by means of Electrochemical Impedance Spectroscopy, the novelty of this thesis.
Two test benches were modified to apply gradients in temperature or concentration, so that the coupled effects could be magnified thus making possible to measure the transport coefficients.
The measurements of the solid oxide electrolyte show large deviations compared to literature values, making possible only a qualitative analysis. The ionic transport coefficient was determined and the coupled transport coefficient was approximated. Possible improvements to increase the reliability of the measurements and the test bench were proposed.
The characterisation of the polymer electrolyte proved to be even more challenging because of the coupling between electrolyte and gas diffusion media. Moreover, the test bench introduced a distortion frequency, reducing the meaningfulness of the measurements. The ionic conductivity was calculated directly from impedance spectra while the coupled coefficients were approximated from the slopes of established curves. The results were compared to

literature values, estimated from mono-causal models.

Keywords: fuel cells, electrolytes, Proton Exchange Membrane, Yttria stabilized zirconia, electrochemical impedance spectroscopy, Non-Equilibrium Thermodynamics.

Contents

List of Figures

List of Tables

Nomenclature

Symbols and indices present in this dissertation are explained in this section. Further rarely used symbols and indices shall be dedined in this work directly before or after the corresponding equation.

List of Abbreviations

CL	Catalyst layer
EIS	Electrochemical Impedance Spectroscopy
GDL	Gas diffusion layer
HFR	High frequency resistance
LFR	Low frequency resistance
MFR	Middle frequency resistance
NET	Non-Equilibrium Thermodynamics
PEM	Proton Exchange Membrane
SOFC	Solid Oxide Fuel Cell

Constants

F	Faraday constant, 96485 $\frac{\mathrm{A \cdot s}}{\mathrm{mol}}$
k_B	Boltzmann constant, $1.380649 \cdot 10^{-23}$ $\frac{\mathrm{m^2 \cdot kg}}{\mathrm{s \cdot K}}$
R	Gas constant, 8.314 $\frac{\mathrm{J}}{\mathrm{mol \cdot K}}$

Greek symbols

α	Charge transfer coefficient
η	Efficiency

λ	Water content
μ	Chemical potential
ν	Stoichiometric factor
ω	Angular frequency
ϕ	Electro(chemical) potential
Π	Peltier coefficient
ψ	Phase shift
σ	Electrical or ionic conductivity
τ	Relaxation time
$\tilde{\mu}$	Electrochemical potential
ε	Permittivity
φ	Electro(static) potential

Superscripts

Θ	Standard conditions
A	Anode
am/ma	Interface anode-membrane
C	Cathode
cm/mc	Interface cathode-membrane
E	Electrolyte
el	electric/al
M	Membrane
R	Reaction

Latin symbols

A	Area
a	Activity of a substance

C	(Electric) Capacity
c	Concentration, either molar or volumetric
D	Diffusion coefficient
d	Thickness
E	Energy
E_{A}	Activation Energy
f	Frequency, while f_{i} corresponds to fugacity of species i
G	Gibbs free enthalpy
H	Enthalpy
I	Electric current
J	Molar flux
k	Thermal conductivity
L	Transport coeffient defined by NET. In singular cases, it refers to Inductivity
m	mass
n	Amount of substance
P	Power
p	Pressure
Q	Thermal energy (or heat)
R	(Electrical) Resistance
r	Reaction rate or specific resistance
S	Entropy
S	Seebeck coefficient
T	Temperature
t	Transport number
U	Gradient in electric potential or voltage

V	Volume
x	Molar fraction
Z	Electrical Impedance
z	Charge number

Subscripts

μ	Associated with transport of water
ϕ	Associated with transport of charge
0	Peak
b	Bulk
eff	Effective
gb	Grain boundary
irr	Irreversible
m	Molar
Naf	Nafion
O	Associated with transport of oxygen anions
OC	Open circuit
q	Associated with transport of thermal energy/heat
S	Saturated vapour
th	Thermodynamic
W	Water

Chapter 1

Introduction

Many people argue that climate change is a bourgeois concern born in the mid 20th century once basic needs had been satisfied. They claim that climate change is a geological cyclic process, resulting in an alternating global warming and cooling. Nothing could be further from the truth [1], [2].

Already in the Ancient Greece, philosophers pointed out in the 4th century BC that swamp draining made regions prone to freezing and that deforestation will lead to an increase of temperature due to the increased sunlight exposure of the ground [3]. In the 10th century, the Chinese published a theory of climate change over centuries, after discovering petrified bamboos in a dry region thousands of kilometres away from the tropical region were they usually are found [4]. Four hundred years after, the Europeans described alterations of the Mediterranean Region over the last millennium due to forest clearing, irrigation and grazing [5].

During the 19th century, diverse theories were suggested to explain and locate the cyclic climate change: biblical ice ages/floods, fluctuations in the composition of atmospheric gases, volcanic activity, the gravitational forces from the Sun and the Moon, etc. At the end of the century, Arrhenius studied the effect of CO_2 in the atmosphere, calculating that halving the CO_2 known to be at the atmosphere at that time would cause an ice age and doubling it would increase the Earth mean atmospheric temperature by about $5 - 6\,\mathrm{K}$ [6].

The 20th century was characterised for the increasing concern on the anthropological contribution to the CO_2 concentration in the atmosphere; many geologists were and are still sceptic about it, arguing that the time and mass scale of Earth are out of range to the humankind, despite the stunning evidence of the catalyst effect human activity is showing [7]. Every renamed scientific agency emphasised their concern during the 60s and 70s: the US Atomic Energy Commission, the NATO, [8] the American Petrol Institute, [9] the UN Conference on

Human Environment, the US National Research Council... the pressure accumulated resulted in the 1992 Rio Summit, which led to the establishment of the UN Framework Convention on Climate Change, UNFCCC.
The UNFCCC stipulates that the delegates of the member countries meet every four years at the Conference of the Parties, COP. At this instance one of the most celebrated agreements was achieved, the 1997 Kyoto Protocol, aimed to reduce the greenhouse gas emissions, admitting the consequences of human activity on global warming. The countries who have signed this Protocol, commit to the reduction of their emissions from 2008 and on. Despite the initial joy, the US, responsible for 50% of the worldwide greenhouse gases emissions, refused to ratify this vital Protocol in 2008, so that no binding reductions were imposed [10].
The frustration after the retrieval of the US, Russia and Japan as well as the exponential growth in CO_2 emissions observed between 1990 and 2010 encouraged the COP15 to finally resume responsibility and actively do something to mitigate climate change, resulting in the most ambitious treaty up to date: the Paris Agreement. It stipulates that the mean global temperature should not rise more than 2 K, ideally 1.5 K compared to pre-industrial levels. Moreover, it aims to reach net-zero emissions in 2050. It was signed so far by 195 countries. Such an ambitious goal shall require every possible effort to reduce emissions and neutralise the emissions that cannot be avoided. Europe accounts for 10% of the worldwide emissions, while Germany is the largest CO_2 producer of the continent [11]. Almost half of the carbon is emitted by Germans to generate either electricity or thermal energy. Luckily, there is one electrochemical device that can yield electricity and thermal energy without carbon being involved: the fuel cell. Fuel cells are the key to a sustainable energetic matrix, being able to generate heat and electricity from fuel chemical energy without intermediate steps, thus increasing the total electricity yield when compared to the combination of combustion-heat engine-generator and avoiding CO_2, keeping in mind that the best carbon for the Earth atmosphere is the carbon that is never produced. Fuel cells can be, depending on their electrolyte type, adapted to both stationary and mobile applications, so that they can be used for power generation or the transport sector. The largest flaw of Paris Agreement is the exclusion of the air and maritime transport sector, where the fuel cell also will be of major impact.

A fuel cell is basically an electrolyte sandwiched between two electrodes. The heart of a fuel cell is the electrolyte, which presents the highest losses and thus reduces the energy conversion efficiency. Optimising the electrolyte is of vital importance to increase their efficiency. Electrolytes have been studied intensively the last five decades, and an enormous advance has been achieved in material science and in the Electrochemistry. The investigations have

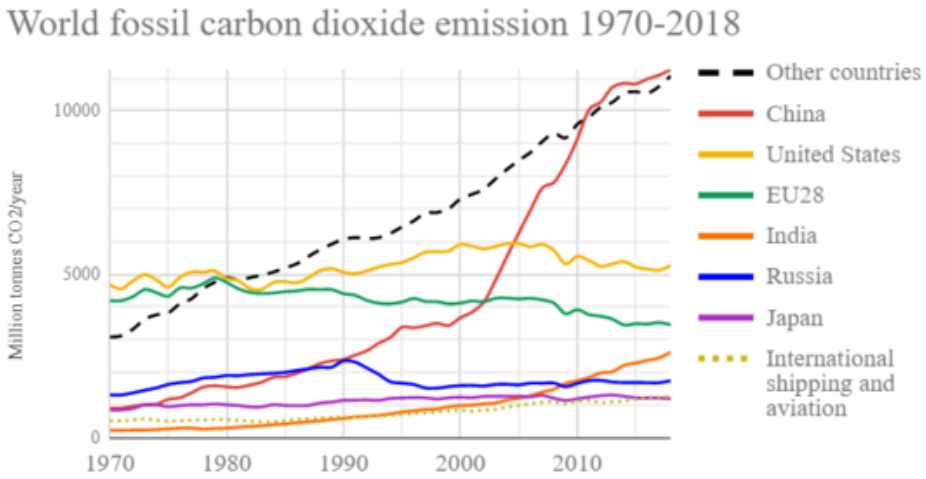

Figure 1.1: Historical carbon CO_2 emissions given by country/sector. Figure by Tomastvivlaren

considered the transport processes in the electrolyte (and in the other components of a fuel cell) to be mono-causal: the charge is transported through the electrolyte due to an electric potential, thermal energy is transported due to a temperature potential or difference and so on. As fuel cells are membrane devices, i.e. their electrolyte is thin compared to the gradients they are exposed to, side effects have been observed. Instead of modeling the fuel cell in a systematic manner, investigations developed a vast literature of new pseudo-thermodynamic quantities to explain what was being empirically obtained [12]. A new universe of empirical values such as water content or transport numbers was born.

It has been shown that the coupling effects in membrane processes cannot be neglected [13], [14]. Rather than correcting mono-causal equations by means of "effective" transport coefficients, it would be desirable to study fuel cells from a multi-causal point of view, as proposed by a theory called Non-Equilibrium Thermodynamics (NET). The basic idea of the NET theory is that every thermodynamic force (temperature differences, concentration gradients, electric potentials) influences every transport mechanism. The resulting transport coefficients have been calculated by Molecular Dynamics and approximated by classical transport coefficients (such as ionic conductivity, Peltier coefficient or the thermal conductivity). The literature on NET-defined transport coefficients being directly measured is very limited. Previous works of this research Institute approximated the transport coefficients with mono-causal ones (as it has been stated in the literature for years) and compared the model with experimental work carried out, as depicted in Fig. 1.2. The comparison concluded that the larger the gradient, the larger the deviation from the model was. Even though the

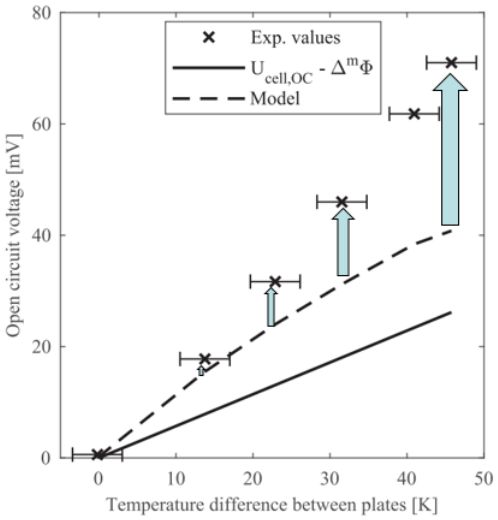

Figure 1.2: Observed deviation of the predicted Open Circuit Voltage of a modeled Thermocell (given by Marquardt [15] from experimental data [16]

mono-causal coefficients are obtained empirically, the model based on them failed to predict the behaviour of the fuel cell in conditions that differ from open circuit condition and constant temperature condition. It became clear that the transport coefficients for applying the NET theory must be determined experimentally.

Fuel cells have been characterised experimentally widely by means of Electrochemical Impedance Spectroscopy (EIS) since the mid 1980s, when MacDonalds [17] made this measurement procedure popular. EIS is a technique that, under certain circumstances, allows the separation of losses caused in a fuel cell or in an electrolyte. Since fuel cells are electrochemical devices, an electric quantity, such as impedance, delivers information about its chemical processes, which are more difficult to determine directly. That is what makes EIS so attractive. The experimental determination of transport coefficients making use of EIS is the question raised. EIS is a technology present in almost every fuel cell laboratory; developing a way to determine intriguing and almost unknown transport coefficients with an accessible device becomes extremely interesting.

In this study, two types of electrolytes were modeled using NET, their transport mechanisms were approximated with EIS and they were characterised using this technique. The coupling effect was clearly visible and the transport coefficients were either calculated or approximated and, when possible, validated with literature values. This thesis opens a door to an exciting concept to be broadened and enhanced in the following years.

Chapter 2

Theoretical background

2.1 Fuel Cells

A fuel cell is an electrochemical device capable of converting the internal energy of a fuel directly into electrical energy. Fuel cells avoid intermediate energy conversions subject to losses when compared to the classical conversion path of combustion, heat engine and electrical generator, i.e. they are not limited by the Carnot efficiency. Furthermore, they present little to no mechanical losses, since they have no moving parts [19].
The fuel cell function principle is based on the redox reaction of water formation:

$$H_2 + \frac{1}{2}O_2 \rightarrow H_2O \tag{2.1}$$

Should the reactants of reaction 2.1 make direct contact, as observed in Fig. 2.1 (a), a spontaneous combustion takes place and the chemical energy turns completely into heat.

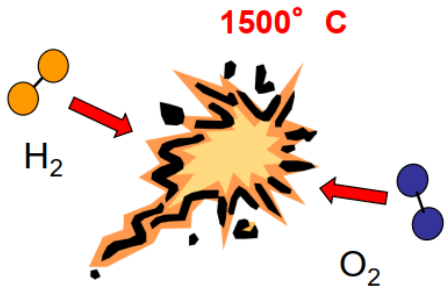

(a) Combustion reaction of hydrogen

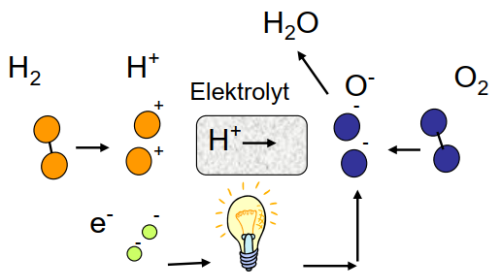

(b) Local separation of half-reactions to gain electricity from the chemical reaction

Figure 2.1: Two possible outcomes of hydrogen making contact with oxygen/air as given by Kabelac and Hanke-Rauschenbach [18].

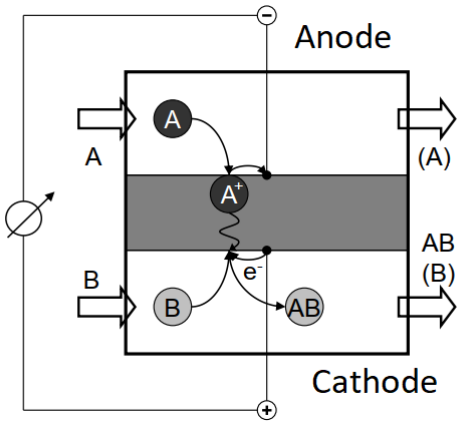

Figure 2.2: Schematic representation of a general fuel cell [18].

The function principle of a fuel cell consists on the local separation of the half-reactions involved, so that the produced electron flow can be directed into an external circuit and used as direct current, as depicted in Fig. 2.1 (b). The presented reaction is now an electrochemical reaction.

Components of fuel cells

A fuel cell, as any other electrochemical cell, consists of three main parts: two electrodes, an electrolyte and an external electric circuit, as seen in Fig. 2.2. The electrolyte is the heart of a fuel cell, since it does not only keep the reactants separated to avoid combustion but also allows ions to move between electrodes *through* the electrolyte. Ideally, the electrolyte is also not permeable to electrons, so that they must take the external circuit to complete the electrochemical reaction.

As per definition anode is the electrode where the oxidation take place, i.e. where a reactant A loses its electrons becoming oxidised. On the contrary, cathode is the electrode where the reduction take place, i.e. where a reactant B gains electrons becoming reduced into AB:

$$\text{Anode:} \qquad \mathrm{A} \rightarrow \mathrm{A}^{+} + \mathrm{e}^{-} \tag{2.2}$$

$$\text{Cathode:} \qquad \mathrm{B} + \mathrm{A}^{+} + \mathrm{e}^{-} \rightarrow \mathrm{AB} \tag{2.3}$$

There are several types of fuel cells, distinguished by their electrolyte types and operation temperature ranges. The electrolyte type defines the charge carrier, as depicted in Fig. 2.3. This dissertation focuses on the two widespread types of fuel cells: the proton exchange membrane (PEM) fuel cell and the solid oxide fuel cell (SOFC). Table 2.1 summarizes the

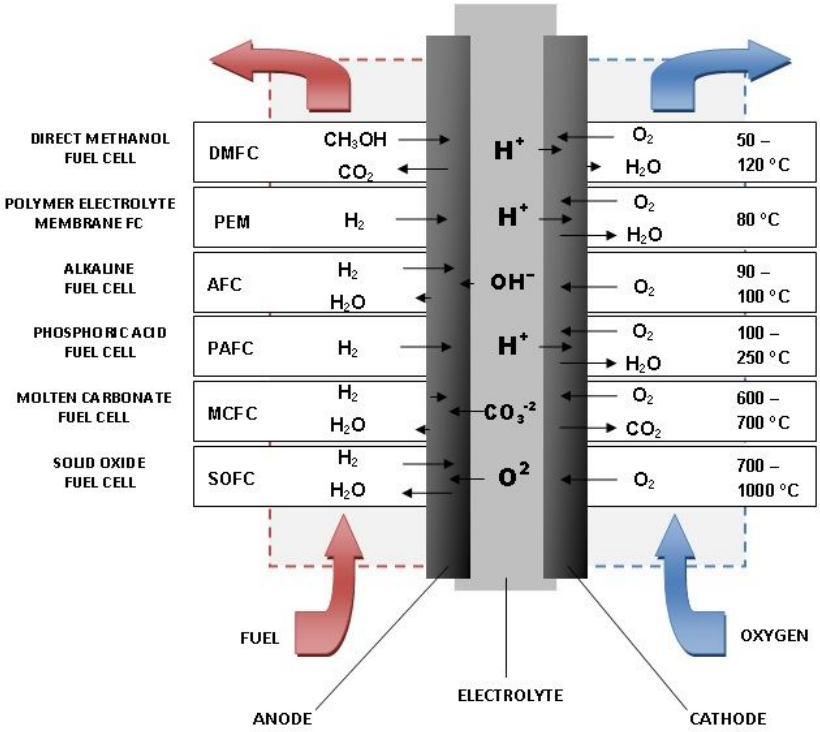

Figure 2.3: Types of fuel cell, named after their electrolyte [20].

Table 2.1: Comparison of the two widespread types of fuel cells: PEM and SOFC

FC type	Anode	Electrolyte	Cathode
PEM	$H_2 \rightarrow +2H^+ + 2e^-$	Polymer	$\frac{1}{2}O_2 + 2H^+ + 2e^- \rightarrow H_2O$
SOFC	$H_2 + O^{2-} \rightarrow H_2O$	Solid oxide	$\frac{1}{2}O_2 + 2e^- \rightarrow O^{2-}$

key facts of them including the half reactions that result from applying Eqs. 2.2-2.3.

Electrolyte

As previously stated, the electrolyte is the heart of the fuel cell and has three main tasks: the local separation of the supplied gases, the conduction of the ions and electronic isolation. As it can be extracted from Table 2.1, each type of fuel cell have different charge carriers, which means their electrolytes must be different. The nature of both electrolytes and the ion diffusion mechanisms will be treated in next chapter.

Electrodes

The electrodes have also multiple functions. Firstly, they have to be porous, so that they ensure that the gases supplied arrive at the catalyst layers located on both sides of the

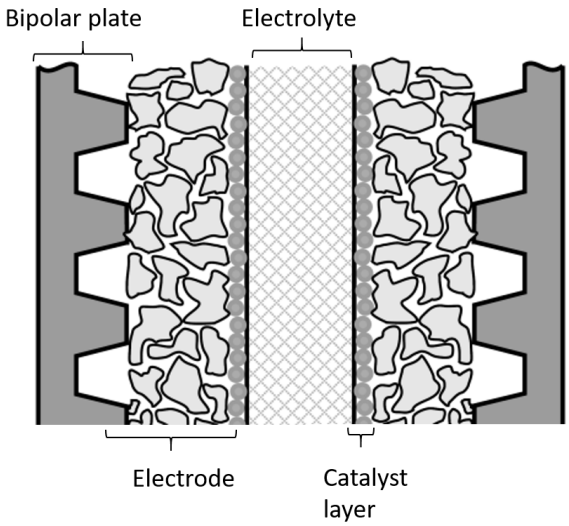

Figure 2.4: Components of a generalised fuel cell, originally depicted by Kabelac and Hanke-Rauschenbach [18] and thereafter modified.

electrolyte, where the half reactions take place. Secondly, they must be electric conductive and form a path to the current collectors (known as bipolar plates), so that the electrons can easily arrive or leave the catalyst layers. They must be additionally chemically resistant to the either oxidising or reducing environment of the electrode.

Catalyst layers

The half reactions that make possible the local separation of a redox reaction do not necessarily take place spontaneously. As it will be explained in Sec. 2.3, these reactions must overcome an activation barrier, which can be reduced by using catalysts. A catalyst layer is then applied between the electrode and electrolyte. The interface electrode-catalyst layer-electrolyte forms what is known as a triple phase boundary (TPB), which must comply with the following conditions:

- being porous to facilitate gas transport
- being electrically conductive for fast electronic motion
- being conductive to ions to promote the diffusion into or out from the electrolyte

Catalyst layers must also be chemically resistant as well as chemically, mechanically and thermally compatible with the materials used both for electrode and electrolyte. In case of PEMFC, the most common catalyst is platinum. As for SOFCs, there are different

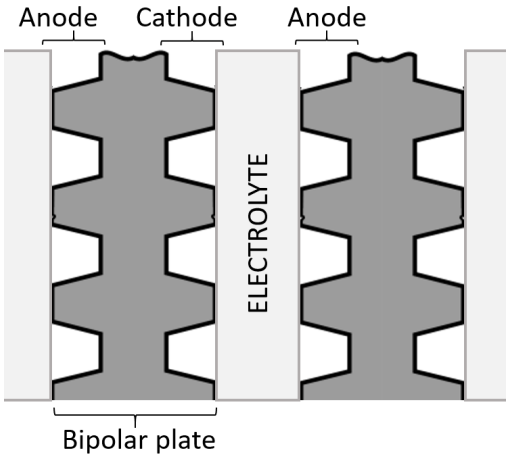

Figure 2.5: Side view of a bipolar plate, modified from Kabelac and Hanke-Rauschenbach [18].

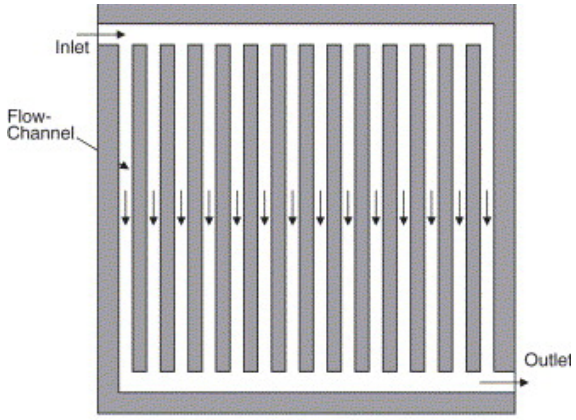

Figure 2.6: Front view of a bipolar plate, making visible the flow field pattern according to Li and Sabir [21].

options, being nickel the most common anode catalyst, and similarly LSM/LSCF (lanthanum strontium manganite and lanthanum strontium cobalt ferrite) for the cathode side.

Current collectors - bipolar plates

The current collectors enhance the external path for electrons from anode to cathode, therefore they must be electrically conductive. Since they face the electrodes, they must also be resistant to both reduction and oxidation, as well as mechanically stable since they assure the compression of the other layers contributing to the fuel cell sealing. In real fuel cells the current collectors are part of the electrodes, because they are designed as flow fields with a double function: supplying gas and conducting electrons, as shown in Fig. 2.6. The ribs or channels are in contact with the electrode while the hollows supply the gases. In case fuel cells are stacked to increase the total output power, the current collector of one cell is at the same time the cathode of its neighbouring cell, so that the mentioned flow fields are present at both sides of the device and thus receiving the name of *bipolar plates*, as depicted in Fig. 2.5. In most cases, the bipolar plates are also part of the cooling system of the fuel cell, having passages for the cooling fluid inlet and outlet.

2.2 Thermodynamics of fuel cells

A fuel cell is constantly supplied with hydrogen and oxygen/air, so that it can be modeled as an open system. Considering the fuel cell in a steady state, the net energy of the system

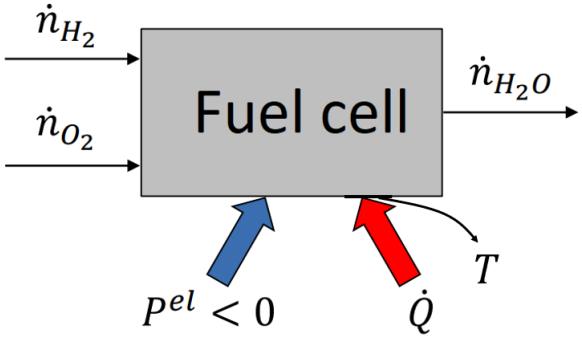

Figure 2.7: Fuel cell energy balance for the general case [18].

remains constant: $\frac{dE}{dt} = 0$. The system boundaries are chosen to circumvent the fuel cell, and the electric and thermal power, P^{el} and $\dot{Q}$, respectively, are considered as net fluxes, as depicted in Fig. 2.7. The following rule has been considered: superscripts note the *location*, e.g. electrolyte while subscripts mark the element, e.g. water. Applying the first law of Thermodynamics for the molar case and neglecting the contributions of potential and kinetic energy, it follows:

$$\frac{dE}{dt} = 0 = P^{\mathrm{el}} + \dot{Q} + \dot{n}_{\mathrm{H_2}} H_{\mathrm{m,H_2}} + \dot{n}_{\mathrm{O_2}} H_{\mathrm{m,O_2}} - \dot{n}_{\mathrm{H_2O}} H_{\mathrm{m,H_2O}} \tag{2.4}$$

In a similar manner the second law becomes:

$$\frac{dS}{dt} = 0 = \frac{\dot{Q}}{T} + \dot{n}_{\mathrm{H_2}} S_{\mathrm{m,H_2}} + \dot{n}_{\mathrm{O_2}} S_{\mathrm{m,O_2}} - \dot{n}_{\mathrm{H_2O}} S_{\mathrm{m,H_2O}} + \dot{S}_{\mathrm{irr}} \tag{2.5}$$

The thermodynamic temperature T is the temperature at the system boundary, where $\dot{Q}$ is crossing. The concept of molar reaction enthalpy $\Delta^{\mathrm{R}} H_{\mathrm{m}}$ and molar reaction entropy $\Delta^{\mathrm{R}} S_{\mathrm{m}}$ are introduced taking into consideration the stoichiometric factors ν_{i}:

$$\Delta^{\mathrm{R}} H_{\mathrm{m}} = \sum_{\mathrm{i}} \nu_{\mathrm{i}} H_{\mathrm{m,i}}, \tag{2.6}$$

$$\Delta^{\mathrm{R}} S_{\mathrm{m}} = \sum_{\mathrm{i}} \nu_{\mathrm{i}} S_{\mathrm{m,i}}. \tag{2.7}$$

The stoichiometric factors ν_{i} result from the corresponding overall chemical reaction, Eq. 2.1 to give $\nu_{\mathrm{H_2}} = -1$, $\nu_{\mathrm{O_2}} = -1/2$ and $\nu_{\mathrm{H_2O}} = 1$, i.e. the reactants are considered negative and the products positive. The conservation of mass, when expressed in molar fluxes gives:

$$\dot{n}_{\mathrm{H_2}} = 2\dot{n}_{\mathrm{O_2}} = -\dot{n}_{\mathrm{H_2O}} \tag{2.8}$$

Introducing Eq. 2.8 in Eq. 2.4 under consideration of Eq. 2.6 results in:

$$\frac{dE}{dt} = 0 = P^{\mathrm{el}} + \dot{Q} - \dot{n}_{\mathrm{H_2}} \Delta^{\mathrm{R}} H_{\mathrm{m}} \tag{2.9}$$

In a similar manner the second law results:

$$\frac{dS}{dt} = 0 = \frac{\dot{Q}}{T} - \dot{n}_{\mathrm{H_2}} \Delta^{\mathrm{R}} S_{\mathrm{m}} + \dot{S}_{\mathrm{irr}} \tag{2.10}$$

In the reversible case, it is possible to calculate the thermal power $\dot{Q}$ from the reaction entropy using Eq. 2.10. If this is then introduced into the first law, the *reversible* electric power $P^{\mathrm{el}}_{\mathrm{rev}}$ can be obtained making use of Gibbs free enthalpy $G_{\mathrm{m}} = H_{\mathrm{m}} - TS_{\mathrm{m}}$:

$$P^{\mathrm{el}}_{\mathrm{rev}} = -\dot{n}_{\mathrm{H_2}} \Delta^{\mathrm{R}} G_{\mathrm{m}} \tag{2.11}$$

The Gibbs free enthalpy sets the maximum obtainable electric power. This upper limit is, of course, technically not possible, since reversibilities could be reduced but not completely avoided. The fraction of *available* free enthalpy G to the theoretical enthalpy H is known as the thermodynamic efficiency η_{th} of a fuel cell:

$$\eta_{\mathrm{th}} = \frac{\Delta^{\mathrm{R}} G_{\mathrm{m}}}{\Delta^{\mathrm{R}} H_{\mathrm{m}}} \tag{2.12}$$

The open circuit voltage (OCV): the Nernst equation

The fuel cell potential or voltage is given by the potential difference between electrodes:

$$U_{\mathrm{cell}} = \phi^{\mathrm{C}} - \phi^{\mathrm{A}} = \Delta\phi^{\mathrm{C}} - \Delta\phi^{\mathrm{A}} - \Delta\phi^{\mathrm{M}} \tag{2.13}$$

The potential results from a charge separation at the reaction layers while no net electric (or ionic) current is flowing. Since the fuel cell is based on an electrochemical reaction, its resulting open circuit voltage (OCV) or $U_{\mathrm{cell,0}}$ should be reached when the reactants and products are ready to go, but the flow of charge charriers is interrupted. The initial state is given by a minimum in the Gibbs free enthalpy:

$$\mathrm{d}G = -S\mathrm{d}T + V\mathrm{d}p + \sum_{\mathrm{i}} \mu_{\mathrm{i}} \mathrm{d}n_{\mathrm{i}} \stackrel{!}{=} 0, \tag{2.14}$$

which only holds when every term is zero, as T, p and all n_{i} are independent variables. The infinitesimal change in the amount of substance of the third term can be replaced by the

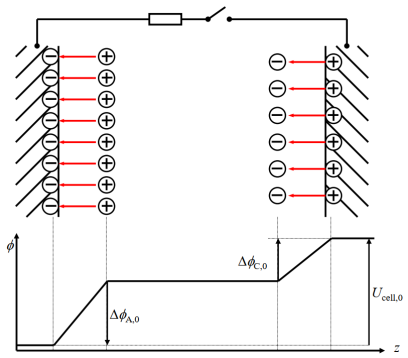

Figure 2.8: Schematic representation of the Nernst potential due to charge separation [18].

equality $\mathrm{d}n_\mathrm{i} = \mathrm{d}\xi \cdot \nu_\mathrm{i}$, but the extent of reaction ζ is zero when there is no reaction. Since the reaction is not chemical but electrochemical, the chemical potential μ_i ought to be replaced by the electrochemical potential $\tilde{\mu}_\mathrm{i} = \mu_\mathrm{i} + z_\mathrm{i} F \phi$, z_i being the charge number (not to be confused with the number of electrons n), so that it follows:

$$0 = \sum_\mathrm{i} \tilde{\mu}_\mathrm{i} \nu_\mathrm{i}. \tag{2.15}$$

Applying the condition of minimum Gibbs free enthalpy given in Eq. 2.15 to the anode ($\mathrm{H_2} \rightarrow 2\mathrm{H^+} + 2e^-$) and considering that the charge of a proton is $+1$ and of an electron -1:

$$0 = -\mu_{\mathrm{H_2}} + 2(\mu_{\mathrm{H^+}} + F\phi^\mathrm{ma}) + 2(\mu_{\mathrm{e^-}} - F\phi^\mathrm{A}). \tag{2.16}$$

Reordering this equation gives the anode potential:

$$\Delta\phi^\mathrm{A} = \phi^\mathrm{A} - \phi^\mathrm{ma} = \frac{-\mu_{\mathrm{H_2}} + 2\mu_{\mathrm{H^+}} + 2\mu_{\mathrm{e^-}}}{2F}. \tag{2.17}$$

Similarly for the cathode:

$$\Delta\phi^\mathrm{C} = \phi^\mathrm{C} - \phi^\mathrm{mc} = \frac{\frac{1}{2}\mu_{\mathrm{O_2}} + 2\mu_{\mathrm{H^+}} + 2\mu_{\mathrm{e^-}} - \mu_{\mathrm{H_2O}}}{2F}. \tag{2.18}$$

The cell potential can now be obtained using Eq. 2.13:

$$U_\mathrm{cell,0} = \frac{\frac{1}{2}\mu_{\mathrm{O_2}} + \mu_{\mathrm{H_2}} - \mu_{\mathrm{H_2O}}}{2F}. \tag{2.19}$$

Taking into consideration the definition of chemical potential and assuming ideal gas (iG) behaviour $\mu_{\mathrm{i}}^{\theta,\mathrm{iG}}(T,p,x) = \mu_{0,\mathrm{i}}^{\theta,\mathrm{iG}}(T,p^\theta) + R_{\mathrm{m}}T\ln\frac{f_{\mathrm{i}}(T,p,x)}{p^\theta}$, the cell potential can be rewritten:

$$U_{\mathrm{cell},0} = \frac{\frac{1}{2}\mu_{\mathrm{O_2}}^{\theta,\mathrm{iG}} + \mu_{\mathrm{H_2}}^{\theta,\mathrm{iG}} - \mu_{\mathrm{H_2O}}^{\theta,\mathrm{iG}}}{2F} + \frac{R_{\mathrm{m}}T}{2F}\ln\frac{(f_{\mathrm{H_2}}/p^\theta)\cdot(f_{\mathrm{O_2}}/p^\theta)^{1/2}}{(f_{\mathrm{H_2O}}/p^\theta)}. \tag{2.20}$$

Given that the first term equals the negative reaction Gibbs enthalpy $-\Delta^{\mathrm{R}}G_{\mathrm{m}}^{\theta}(T)$ due to Euler's equation $G_{\mathrm{m}} = \sum_{\mathrm{i}} x_{\mathrm{i}}\mu_{\mathrm{i}}$ for given (T,p^θ) at a standard pressure p^θ, and generalising the second term for k species taking part in the reaction results in:

$$U_{\mathrm{cell},0} = \frac{-\Delta^{\mathrm{R}}G_{\mathrm{m}}^{\theta}(T)}{2F} + \ln\prod_{\mathrm{i}=1}^{k}\left(\frac{f_{\mathrm{i}}}{p^\theta}\right)^{\nu_{\mathrm{i}}}, \tag{2.21}$$

which is known as the Nernst equation and is depicted in Fig. 2.8. Writing the equation in this manner allows a more detailed study. It is observable that the higher the temperature T are, the lower is the OCV $U_{\mathrm{cell},0}$, since the Gibbs reaction enthalpy decreases at increasing temperature. This fact is, in actual fuel cells, counteracted by an improvement of kinetics at higher temperature [22], so that a high temperature is *desired*. Material properties play also a role limiting the operation temperatures. The second term predicts a higher OCV at high pressures, which holds true in reality. Nevertheless, material properties also limit the operation pressure, and the fact that gases must be compressed at expense of the electric power generated by the fuel cell leads to limitations in high pressure practical applications [23].

2.3 Kinetics: the Butler-Volmer equation

Most electrochemical reactions can be modeled by means of the Butler-Volmer equation. It is not in the scope of this thesis to deduce this equation, it is taken from the literature [24]. Kinetics plays an essential role at the electrodes of a fuel cell, whereas no electrochemical reaction takes place in the electrolyte.

The Butler-Volmer equation provides a relationship between the reaction rate r_{k}, i.e. how fast a reaction takes place, and the reaction overpotential η_{k}, i.e. how much electric potential is *consumed* to cause or *activate* the reaction $\eta_{\mathrm{k}} = E^{\Theta} - E_{\mathrm{eq,k}}$.

The electrochemical reaction rate is dependent on, among others, temperature and concentration [24]. In its most general approach, the Butler-Volmer equation can be expressed

as:

$$r_{\mathrm{k}} = (a \cdot d) \cdot \frac{j_0^{\mathrm{ref}}}{nF} \left\{ \prod_{\mathrm{k=ox}} \left(\frac{c_{\mathrm{i}}}{c_{\mathrm{i}}^{\mathrm{ref}}} \right)^{\beta_{\mathrm{i,k}}} \cdot \exp\left[- \frac{\alpha_{\mathrm{k}} |n_{\mathrm{k}}| F}{RT} \cdot \eta \right] - \prod_{\mathrm{k=red}} \left(\frac{c_{\mathrm{i}}}{c_{\mathrm{i}}^{\mathrm{ref}}} \right)^{\gamma_{\mathrm{i,k}}} \cdot \exp\left[- \frac{(\alpha_{\mathrm{k}} - 1) |n_{\mathrm{k}}| F}{RT} \cdot \eta \right] \right\}. \tag{2.22}$$

At each electrode k reactions can take place, being involved i species in each of them. The k^{th} reaction rate r_{k} results from the *forward* reaction rate $r_{\mathrm{k,f}}$, given by the first term, and the *backward* reaction rate $r_{\mathrm{k,b}}$ in the second term. The directions are defined for the reduction reaction, i.e.:

$$\mathrm{Ox} + ze^- \xrightarrow{r_{\mathrm{k,f}}} \mathrm{Red}, \tag{2.23}$$

$$\mathrm{Ox} + ze^- \xleftarrow{r_{\mathrm{k,b}}} \mathrm{Red}. \tag{2.24}$$

The fraction $\frac{c_{\mathrm{i}}}{c_{\mathrm{i}}^{\mathrm{ref}}}$ gives the dependency of the reaction rate on the concentration of the i species, since the concentration is dependent on time and space $c_{\mathrm{i}} = f(\overrightarrow{r}, t)$.
Furthermore, the following coefficients are to be determined experimentally:

- α_{k} is called the charge transfer coefficient or symmetry factor.
- $\beta_{\mathrm{i,k}}$ and $\gamma_{\mathrm{i,k}}$ are the reaction orders of the reactions, i.e. they determine the (power) time dependency of the reaction rate.
- $(a \cdot d)$, called electrode roughness [22], describes the electrode surface availability, a being the active inner surface per volume unit (in $m^2_{\mathrm{active}}/m^3$) and d the electrode thickness.

Both the SOFC and the PEMFC, when fed with hydrogen, perform one single reaction ($k = 1$) at each electrode. It is known that, in both cases, activation losses in the cathode are greater than in the anode, i.e. the cathode reaction rate is the limiting factor for the fuel cell performance [22], [23]. The cathode reaction rate r_{C} given by Butler-Volmer is illustrated exemplary in Fig. 2.9 versus the overpotential η_{C}.

In order to experimentally determine the above listed parameters and coefficients, it becomes necessary to split up the equation. In case of great overpotentials, either the back or the forward reaction rate becomes predominant (if $\eta >> 0 \rightarrow r_{\mathrm{k,f}} << r_{\mathrm{k,b}}$; if $\eta << 0 \rightarrow r_{\mathrm{k,f}} >> r_{\mathrm{k,b}}$) and only one term of the equation is considered, what is known as the Tafel equation approximation, as observed in Fig. 2.10 (a). On the other hand, if the overpotential is small, tending to zero, the exponential function can be approximated to a linear function (if $\eta \approx 0 \rightarrow \exp(\eta) \approx 1 + \eta$), as depicted in 2.10 (b).

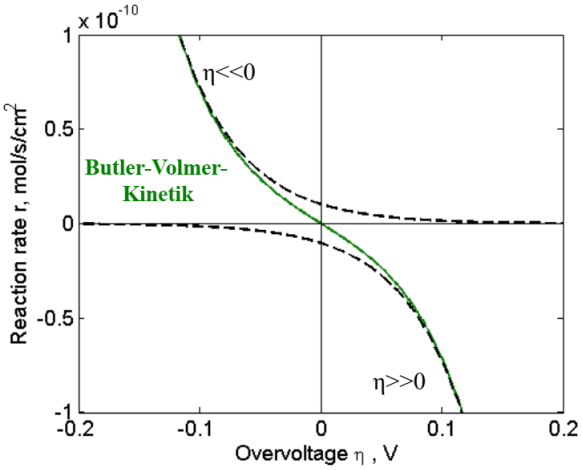

Figure 2.9: Cathode reaction rate r_C vs. the overpotential $\eta_C = E^{\Theta} - E_{eq}^{C}$ [18].

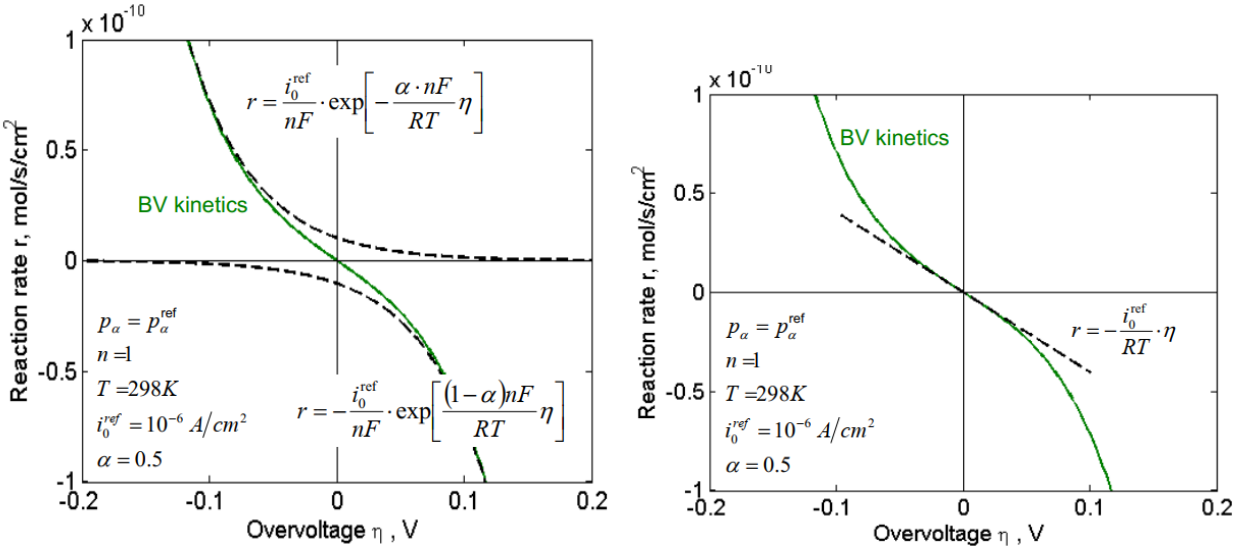

(a) Tafel equation **(b)** Linear approximation

Figure 2.10: Approximations of the Butler-Volmer equation [18]

2.4 Transport of mass, charge and thermal energy

Fuel cells are typically described in terms of classical mono-causal equations. The transport of thermal energy in electrolytes, for example, can well be described using Fourier law of conduction:

$$\dot{\boldsymbol{Q}} = -k(T) \cdot \nabla T, \tag{2.25}$$

since both polymer and solid oxide electrolytes are solids and therefore no convective heat transfer takes place. The heat flux $\dot{Q}$ has only one cause, the gradient of the temperature ∇T as the single driving force. Radiation could, however, play a role in solid oxide electrolytes, although previous studies have shown that its contribution within the dimensions of a solid oxide cell is negligible.

The ion transport in solid oxide ceramics occurs through defects in the lattice [25]. The diffused particles *jump* from one defect to the next one, thus *moving* through the material. Depending on the solid structure, it allows the diffusion of cations, anions and/or electrons. Diffusion can be approximated, in its simplest mono-causal way, with the Fick law of diffusion:

$$\boldsymbol{J}_{\mathrm{i}} = -D_{\mathrm{ij}}(p,T)\nabla c_{\mathrm{i}}^{\mathrm{j}}, \tag{2.26}$$

where the mass flux of species i is proportional to the gradient of the concentration of i in the medium j and the proportionality factor is given as the diffusion coefficient D_{ij}.

The transport or charge can be modeled using Ohm's law: an electric current, either electronic or ionic, is mono-causally driven by an electric potential:

$$\boldsymbol{j} = -\sigma(T)\nabla\phi, \tag{2.27}$$

where the proportionality coefficient is called electric or ionic conductivity σ. The conduction mechanisms in non-metallic solids are different than in metals. The ionic conductivity is caused mainly by defects in the solid lattice. The ionic conductivity σ_{i} in a solid can be described as:

$$\sigma_{\mathrm{i}} = |z_{\mathrm{i}}| \cdot F \cdot \nabla c_{\mathrm{i}} \cdot u_{\mathrm{i}}, \tag{2.28}$$

being z_{i} the charge number, c_{i} the molar concentration of ion i and u_{i} the mobility of the ion or charge carrier, which is defined as:

$$u_{\mathrm{i}} = \frac{\boldsymbol{w}_{\mathrm{i}}}{\nabla\phi}, \tag{2.29}$$

i.e. it is proportional to the velocity $\boldsymbol{w}_\mathrm{i}$ of the ions i and to the inverse of the electric potential as the driving force.

2.5 Coupled effects

The transport of ions has been so far presented in two different manners, both as mass and charge. This indicates that a transport of ions can be initiated either by a gradient in concentration of this species or by a gradient in potential or both. Their nature makes it necessary to consider the coupling of both effects to calculate the net flux, which can be accomplished by introducing the electrochemical potential $\tilde{\mu}$, as previously mentioned, so that it can be stated:

$$\boldsymbol{J}_\mathrm{i} = -\tilde{D}_\mathrm{ij} \nabla \tilde{\mu}_\mathrm{i} \tag{2.30}$$

in which $\tilde{D}_\mathrm{ij}$ is the electrochemical diffusion coefficient, different than the (chemical) diffusion coefficient since it is multi-causal: it could happen that chemical and electrical potential have the same magnitude and different direction, so that no transport takes place.
One of the well known coupling effects is the thermoelectricity, which is function principle of thermocouples. In this case a temperature gradient causes an electric potential under open circuit conditions:

$$(\nabla \boldsymbol{\phi})_{\mathrm{j}=0} = S(T) \nabla \boldsymbol{T}, \tag{2.31}$$

being S the Seebeck coefficient of the material. The Seebeck coefficient is positive when the temperature gradient is opposite to the electrochemical potential gradient. The thermoelectricity can also be expressed in terms of the Peltier effect, where a thermal energy flux is driven by an electric current $\dot{Q} = \Pi(T)\boldsymbol{I}$. The interplay between them is given by Thomson second relation $\Pi = TS$. Measuring the Peltier coefficient of electrolytes is, however, more difficult than measuring the Seebeck coefficient, since heat fluxes cannot be directly measured (which is given for electric potentials) and keeping a constant temperature while heat is flowing through the system is impractical [26].
In a similar manner, the gradient in temperature could also cause a mass transport, effect that is known as thermodiffusion or Soret effect:

$$\boldsymbol{J}_\mathrm{i} = -S_\mathrm{T}(T) \nabla \boldsymbol{T}, \tag{2.32}$$

where S_T is called the Soret coefficient. Analogously the heat flux caused by a gradient in the concentration (or, more precisely, a gradient in the chemical potential of the species i) is called Dufour effect $\dot{Q} = S_\mathrm{D} \nabla c_\mathrm{i}$ and S_D is the Dufour coefficient. They are not as widespread

and well investigated as thermoelectricity, as they are considered to be of minor relevance. Couple effects have been studied by classic Thermodynamics as particular conditions for few applications, mostly when their effect cannot be neglected: either when the coefficient is noticeable or when the (coupled) driven force is large. A more systematic approach that covers the coupling of transport mechanisms with a more systematic approach is given by Non-Equilibrium Thermodynamics, which will be introduced in the following section.

2.6 Non-Equilibrium Thermodynamics (NET)

Based on the works of Onsager [27], [28], for which he was awarded a Nobel price in Chemistry in 1968, Non-Equilibrium Thermodynamics is the effort of many researchers to explain and model systems that are not in global equilibrium [14].
In such systems, this theory redefines the second law of Thermodynamics considering that a *local* equilibrium is given. The entropy of a real system can only increase; in the theoretical case of a reversible process entropy remains constant. The key assumption of NET is an ambiguous view on a local element: there is a non-equilibrium situation with gradients and transport processes going on, but the Gibbs fundamental equation (which is derived for a thermodynamic equilibrium situation) still holds true. The law of conservation for the entropy flux J_s in an infinitesimal small element reads:

$$\frac{\partial s}{\partial t} = -\nabla J_\mathrm{s} + \dot{\sigma}, \tag{2.33}$$

where J_s is the volumetric entropy density and $\dot{\sigma}$ is the volumetric entropy production. The latter plays a key role in the NET theory.
Applying Gibbs fundamental relation to the previously defined infinitesimal volume $\mathrm{d}V$:

$$\mathrm{d}u = T\mathrm{d}s + \sum_\mathrm{j} \mu_\mathrm{j} \mathrm{d}c_\mathrm{i}, \tag{2.34}$$

so that the first term of Eq. 2.33 can be obtained by solving for $\mathrm{d}s$ from Eq. 2.34 and differentiating it on behalf of time:

$$\frac{\partial s}{\partial t} = \frac{1}{T}\frac{\partial u}{\partial t} - \frac{1}{T}\sum_\mathrm{j} \mu_\mathrm{j} \frac{\partial c_\mathrm{i}}{\partial t}. \tag{2.35}$$

The concentration rate is given by:

$$\frac{\partial c_{\mathrm{i}}}{\partial t} = -\nabla J_{\mathrm{j}} + \nu_{\mathrm{j}} r, \tag{2.36}$$

where J_{j} is the flux of species j, ν_{j} the stoichiometric factor of species j in the chemical reaction and r_{j} the reaction rate. The definition of Gibbs reaction enthalpy (see Eq. 2.21) makes possible to sum up:

$$\Delta^{\mathrm{R}} G_{\mathrm{m}} = \sum_{\mathrm{j}} \nu_{\mathrm{j}} \mu_{0,\mathrm{j}}. \tag{2.37}$$

The inner energy rate from Eq. 2.35 can be obtained from the energy conservation law:

$$\frac{\partial u}{\partial t} = -\nabla J_{\mathrm{q}} - j \nabla \phi, \tag{2.38}$$

where J_{q} is the heat flux, j the electric current and $\nabla\phi$ the electric potential. Introducing the measurable heat flux $J_{\mathrm{q}}^{'} = J_{\mathrm{q}} - \sum_{\mathrm{j}} H_{\mathrm{j}} J_{\mathrm{j}}$ and replacing Eqs. 2.38 and 2.36 in 2.35 and thereafter in Eq. 2.33, making use of the differentiation product rule and solving for $\dot{\sigma}$, it follows the basic equation for the local entropy production rate:

$$\dot{\sigma} = J_{\mathrm{q}} \nabla \frac{1}{T} + \sum_{\mathrm{j}} J_{\mathrm{j}} \Big(-\frac{1}{T} \nabla \mu_{0,\mathrm{j}} \Big) + j \Big(-\frac{1}{T} \nabla \phi \Big) + r \Big(-\frac{\Delta^{\mathrm{R}} G_{\mathrm{m}}}{T} \Big). \tag{2.39}$$

As observed in Eq.2.39, the entropy production rate $\dot{\sigma}$ can be understood and therefore now defined as the product sum of conjugated fluxes $J_{\mathrm{i}} = J_{\mathrm{q}}, J_{\mathrm{j}}, j, r$, and forces $X_{\mathrm{i}} = \nabla \frac{1}{T}, -\frac{1}{T} \nabla \mu_{\mathrm{j}}, -\frac{1}{T} \nabla \phi, -\frac{\Delta^{\mathrm{R}} G}{T}$ [14]:

$$\dot{\sigma} = \sum_{\mathrm{i}} \boldsymbol{J}_{\mathrm{i}} \cdot \boldsymbol{X}_{\mathrm{i}}. \tag{2.40}$$

The fluxes J_{i} are dependent on all forces X_{i} [13]:

$$\boldsymbol{J}_{\mathrm{i}} = \sum_{\mathrm{j}} L_{\mathrm{ij}} \cdot \boldsymbol{X}_{\mathrm{j}}. \tag{2.41}$$

The proporcionality coefficients L_{ij} in Eq. 2.41 are called phenomenological coefficients, transport coefficients or simply conductivities.

NET offers a general description of homogeneous systems where coupled processes cannot be neglected, such as mass and charge in the electrolyte. Moreover, it can also be extended to heterogeneous systems, where phase boundaries are present. This fact makes possible to consider the coupling of chemical reactions at interfaces, as it happens at the electrode surfaces [13]. In the most general case, fuel cell electrolytes are subject to a thermal energy

flux J_q, a mass flux $\boldsymbol{J}_\mathrm{k}$ for every species k and a charge transport $\boldsymbol{j}$, driven by gradients in the temperature $\nabla\frac{1}{T}$, chemical potential $\frac{1}{T}\nabla\mu_\mathrm{k}$ and electric potential$\frac{1}{T}\nabla\phi$:

$$\boldsymbol{J}_\mathrm{q} = -L_\mathrm{qq}\nabla\frac{1}{\boldsymbol{T}} - \sum_\mathrm{k} L_\mathrm{qk}\frac{1}{T}\nabla\boldsymbol{\mu_\mathrm{k}} - L_{\mathrm{q}\phi}\frac{1}{T}\nabla\boldsymbol{\phi}, \tag{2.42}$$

$$\boldsymbol{J}_\mathrm{k} = -L_\mathrm{kq}\nabla\frac{1}{\boldsymbol{T}} - \sum_\mathrm{k} L_\mathrm{kk}\frac{1}{T}\nabla\boldsymbol{\mu_\mathrm{k}} - L_{\mathrm{k}\phi}\frac{1}{T}\nabla\boldsymbol{\phi}, \tag{2.43}$$

$$\boldsymbol{j} = -L_{\phi\mathrm{q}}\nabla\frac{1}{\boldsymbol{T}} - \sum_\mathrm{k} L_{\phi\mathrm{k}}\frac{1}{T}\nabla\boldsymbol{\mu_\mathrm{k}} - L_{\phi\phi}\frac{1}{T}\nabla\boldsymbol{\phi}. \tag{2.44}$$

These equations will be the starting point of the next chapter, where a specific case and appropiate boundary conditions will be applied for different electrolytes studied in this work. For both cases, the fluxes shall be considered one-dimensional in the direction of the y-cordinate, across the electrolyte (which surface area is given by xz), considering that transport in other directions might be present but negligible small, so that the vector fluxes $\boldsymbol{J}_\mathrm{i}$ can be replaced with scalar fluxes J_i and the gradient ∇X_j is reduced to a total derivative $\frac{\mathrm{d}X_\mathrm{j}}{\mathrm{d}y}$. Furthermore, the inverse temperature dependency shall be reconfigured to gain simplicity by means of the mathematical relation $\frac{\mathrm{d}}{\mathrm{d}y}\left(\frac{1}{T}\right) = \frac{1}{T^2}\frac{\mathrm{d}T}{\mathrm{d}y}$.

2.7 Characterisation techniques

As is true for any other device, the real performance of fuel cells deviate from their theoretical behaviour. Characterisation is essential to optimise their design, reducing losses. Among the different characterisation methods *ex situ* and *in situ* techniques can be distinguished. The former evaluate the performance of a component or group of components standing alone, while the latter study them under operating conditions. Widespread ex situ techniques worth mentioning are:

1. Porosity determination: the gas diffusion in the electrodes depends on their pore structure, hence the importance of their porosity determination. Some of them are nonetheless destructive techniques [23].

2. Imaging: aided by different imaging techniques, such as Infrared (IR), Screening electronic microscopy (SEM), Transmission Electronic Microscopy (TEM) or X-Ray, the microscopic structure of electrodes, electrolytes or catalysts can be determined.

3. X-Ray Difraction (XRD): with this method it is possible to determine the composition and crystal structure of components.

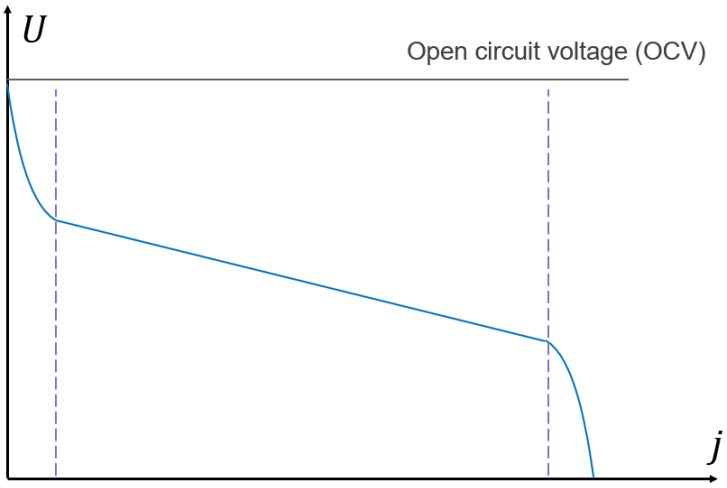

Figure 2.11: U-j characteristics of a PEM fuel cell modified from [18].

4. Thermal conductivity: there are mainly two methods to obtain the thermal conductivity of the different layers of a fuel cell; the termed transient methods and the constant heat flux techniques [29].

5. Brunauer-Emmett-Teller (BET) surface area measurement. The active surface area of a catalyst is of extreme importance to reduce activation losses. With this techique it is possible to accurately determine the surface area of many types of materials [30].

6. Gas permeability: testing gas permeability is important to examine the goodness of electrodes as well as verifying that electrolytes present low to none.

On the other hand, *in situ* techniques have the main advantage of taking into consideration the interplay between all electrochemical forces during the measurement as well as junction effects, while their drawback consists of the difficulty to separate the individual contribution of components to the total loss. According to O'Hayre [23] the most common methods are:

- U-j Characteristics: the steady state cell voltage is recorded while the current is increased slowly. An example of the obtained curve for a PEM fuel cell can be found in Fig. 2.11.

- Cyclic Voltammetry (CV): the applied voltage to the cell is swept between two values and the current response is recorded resulting in a cyclic voltammogram, as depicted exemplary in Fig. 2.12.

- Current interrupt measurement: a current is imposed to the cell for a short time at $t = 0$, and the voltage response is measured until it reaches a steady state. The

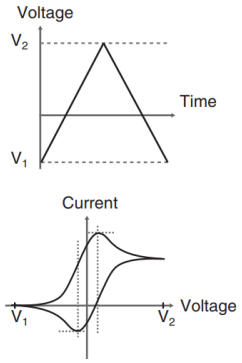

Figure 2.12: Function principle of cyclic voltammetry, taken from [23].

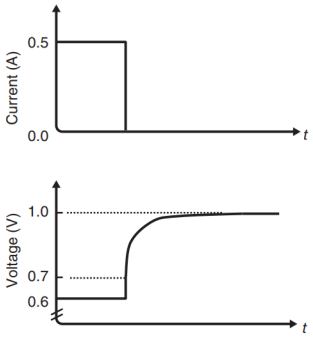

Figure 2.13: function principle of current interrupt, taken from [23].

diagram obtained is given as an example in Fig. 2.13. It allows to determine the dynamic behaviour of the cell, useful for the estimation of the parameters defined by Butler-Volmer in Eq. 2.3.

- Electrochemical Impedance Spectroscopy (EIS): a frequency dependent sinusoidal signal is applied, and the frequency dependent response is measured. This method is explained in detail in next section, as it is the characterisation technique chosen for this dissertation.

2.8 Electrochemical Impedance Spectroscopy (EIS)

Electrochemical Impedance Spectroscopy (EIS) is a powerful tool to differentiate the source of losses, given the condition of sufficient distance between relaxation times of the different electrochemical processes.
The method consists in applying a periodic electrical signal, either a current or a voltage, to an electrochemical system and measuring its periodic response. If the applied signal is a current, it is called galvanostatic EIS; when periodic voltage is applied it is known as potentiostatic EIS.
Let for instance potentiostatic serve as an example to explain the function principle of EIS. The excitation is given by a voltage of constant amplitude and varying frequency $U(\omega) = U_0 \cdot \sin(\omega \cdot t)$. The periodic response of the sample should be a current $I(\omega, \psi) = I_0 \cdot \sin[\omega \cdot t + \psi(\omega)]$, so that the quotient of both quantities results in the frequency dependent impedance $\underline{Z}(\omega, \psi)$:

$$\underline{Z}(\omega, \psi) = \frac{U(\omega)}{I(\omega, \psi)} = Z_0(\omega) \cdot e^{-i\psi} = Z_0 \cdot \cos(\psi) - i\, Z_0 \cdot \sin(\psi) \tag{2.45}$$

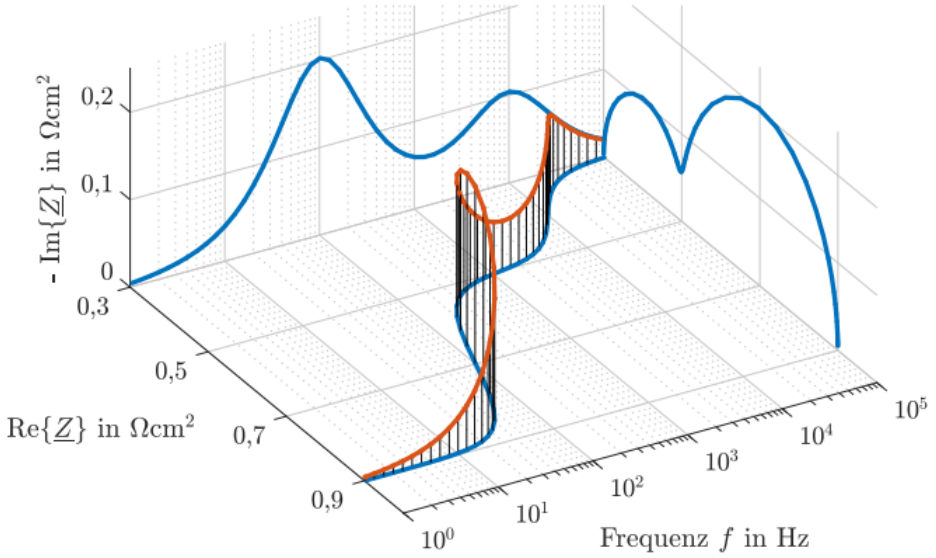

Figure 2.14: 3D representation of impedance dependency $Z(\omega, \psi)$ as given by Hollmann [31].

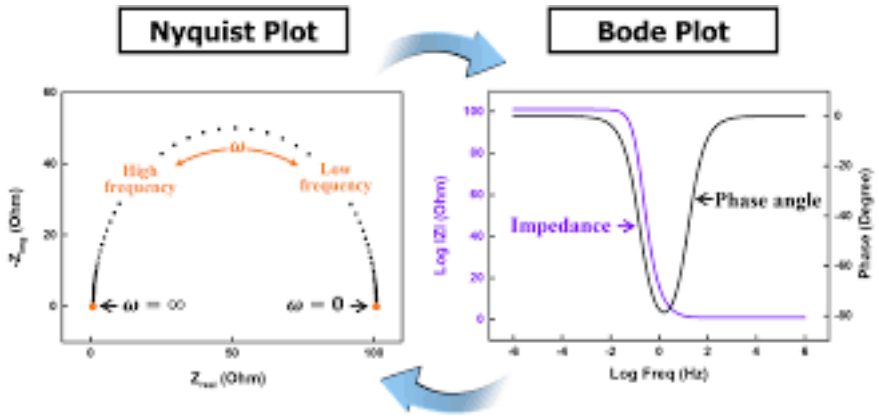

Figure 2.15: 2D diagrams of impedance curves $Z(\omega, \psi)$ as given by Choi et al. [32].

As seen from Eq. 2.45, the impedance curves have two variables, so that a 3D representation is needed for its complete understanding, as depicted in Fig. 2.14. Such representations are, however, rare. Widespread are Nyquist plots, and seldom, Bode plots. Both are exemplary depicted in Fig.2.15. The former are intended to represent the complex nature of impedance, plotting the negative imaginary part $-\mathrm{Im}\underline{Z}$ versus the real part $\mathrm{Re}\underline{Z}$, whereas the latter plot the frequency dependency of both the magnitude $|Z|(\omega)$ and phase shift $\psi(\omega)$ of the impedance.

The characterisation of complex electrochemical systems such as fuel cells using EIS usually consists in measuring its impedance and deduce an equivalent (electric) circuit, as known within electrical engineering. This behaviour shall be first explained, in order to understand the limitations of this approach.

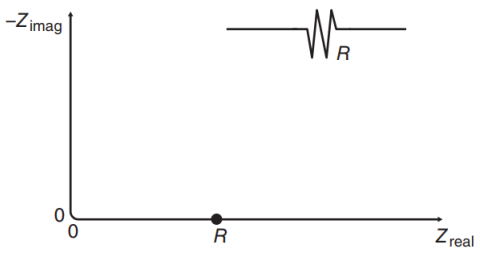

Figure 2.16: Nyquist plot of a single resistor R according to [23]

2.8.1 EIS and equivalent circuits

The impedance Z_k is defined as a complex number, where the real part is given by the resistance R_k and the imaginary part by the reactance $X_\mathrm{k} = X_\mathrm{L} - X_\mathrm{C}$:

$$Z_\mathrm{k}(\omega) = R_\mathrm{k} + i(X_\mathrm{L} - X_\mathrm{C}) \tag{2.46}$$

Applying EIS to a pure ohmic resistor R_k would result in a single dot on the abscissa, since resistors show no frequency dependence, as shown by Fig. 2.16. If the resistor is now connected in series to a capacitor C_k, the impedance results:

$$Z_\mathrm{k}(\omega) = R_\mathrm{k} - iX_\mathrm{C} = R_\mathrm{k} - i\frac{1}{\omega C_\mathrm{k}} \tag{2.47}$$

More relevant to electrochemical cells becomes the parallel connection between resistor and capacitor:

$$Z_\mathrm{k}(\omega) = \frac{1}{1/R_\mathrm{k} + i\omega\, C_\mathrm{k}} \tag{2.48}$$

The impedance curve of both RC circuits are given in Fig. 2.17. While the series connection shows a straight line, the parallel circuit results in a semicircular behaviour. As stated before, the latter is of interest, due to the nature of fuel cells. The high concentration of opposite charge carriers at both sides of the electrolyte, as explained in detail in Sec. 2.3, causes a double layer effect, similar to a plates capacitor, where one side presents a negative charge while the other one is positively charged. If a non conductive material lies between them, from the Coulomb'Law this shall cause an electric field E, explaining the analogy to the capacitor C_k. Furthermore, the resistor R_k can be understood as the electrode resistance R_k to the reaction kinetics when this reaction can be simplified with the Tafel approximation [23]. The overpotential can then be expressed as:

$$\eta_\mathrm{k} = -\frac{RT}{\alpha n F}\ln i_0 + \frac{RT}{\alpha n F}\ln i \tag{2.49}$$

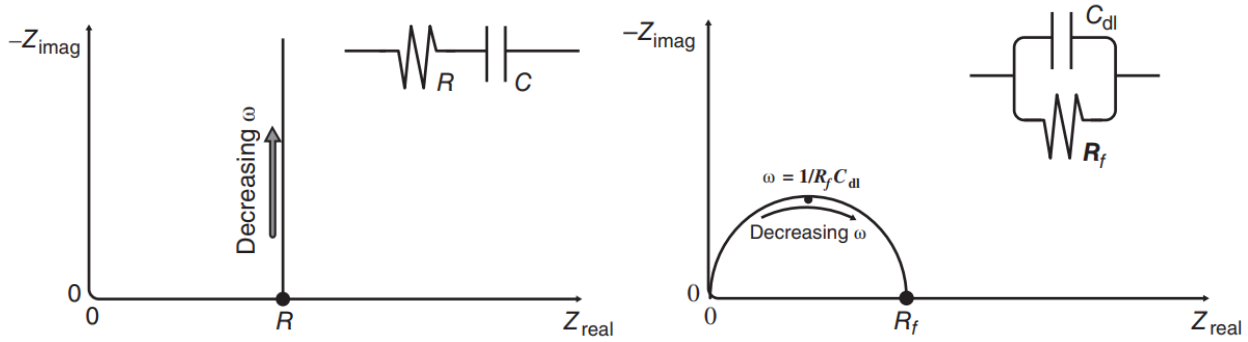

(a) Series circuit **(b)** Parallel circuit

Figure 2.17: Nyquist plots of RC circuits, according to [23].

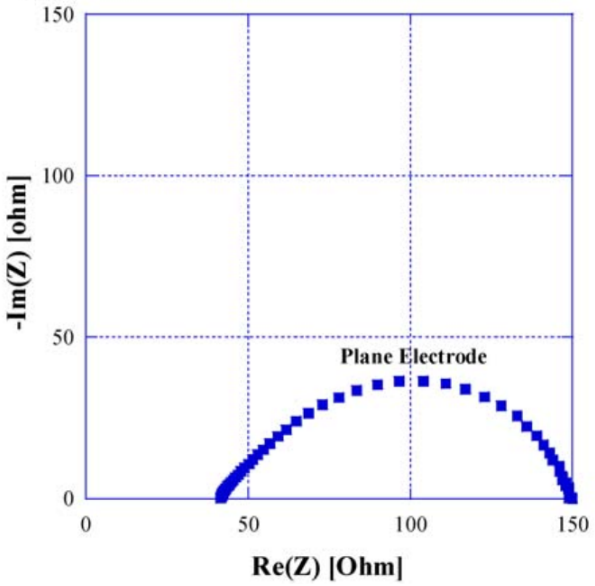

Figure 2.18: Nyquist plot of a single cell formed by a 3YSZ electrolyte and brushed Pt-electrodes measured at $T = 973\,\mathrm{K}$ as given by Lee et al. [33].

Considering that at small perturbations, as usual when applying EIS, the electrode impedance $Z = \frac{U}{I}$ can be approximated to $Z = \frac{dU}{dI}$ i.e., to the slope of the $U - j$ response, the resulting impedance is independent of the resistance and the electrode resistance R_k can be estimated as:

$$Z_\mathrm{k} = R_\mathrm{k} = \frac{RT}{\alpha n F}\frac{1}{i} \tag{2.50}$$

In that case, the diameter of the semicircle is given by the resistance R_k and from the frequency at the apex ω_a it is possible to estimate the relaxion time $\omega^{-1} = \tau = R_\mathrm{k} C_\mathrm{k}$.

Real electrodes can seldom be modeled with $R//C$ elements, e.g. the Nyquist Plot of a 3YSZ electrolyte with Pt-electrodes at $T = 973\,\mathrm{K}$, given by Lee et al [33]. In most cases

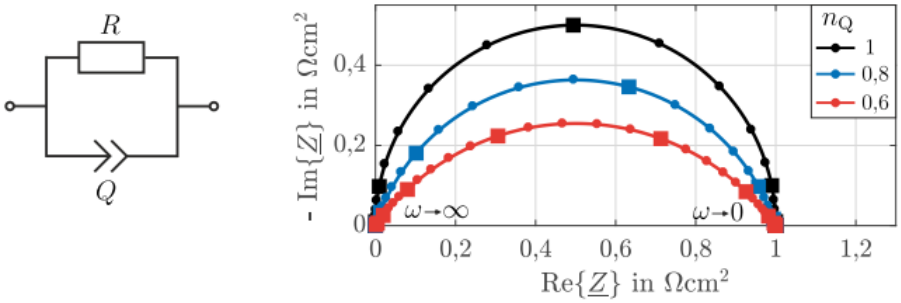

Figure 2.19: Nyquist plot of a $R//CPE$ element, taken from [31].

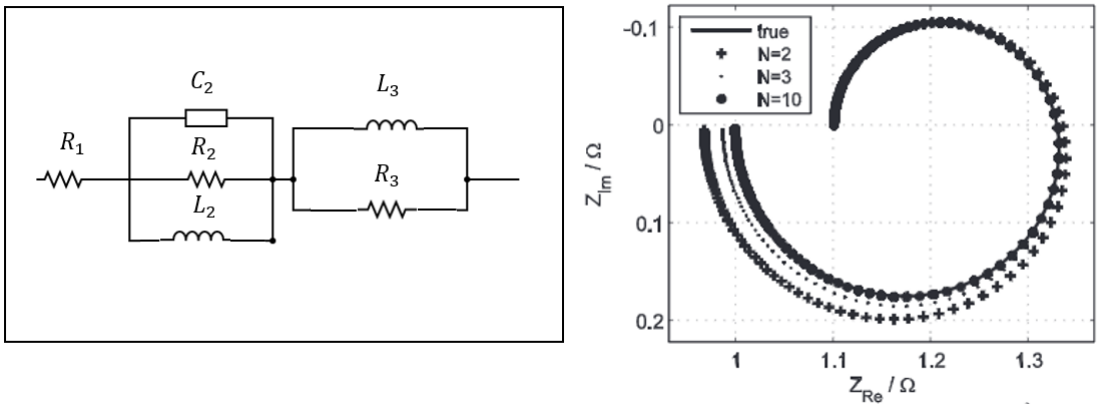

Figure 2.20: Electrical circuit from passive elements $R_\mathrm{i}, C_\mathrm{i}$ and L_i connected as shown in the left part. In the right part, the approximation of the real system with N number of $R//C$ elements. Taken from Schoenleber et al. [34].

they present an arc behaviour, as shown in Fig. 2.19. At this point, a divergence must be highlighted. Following the state-of-the-art EIS characterisation, it was proposed to introduce a new passive element, a constant phase element (CPE) to model this arc as a parallel connection to a resistor, $R//CPE$. The limitations of this approach are presented in the following section.

2.8.2 Limitations of the equivalent circuit approach

The impedance arc measured from real systems can be fitted to several idealized equivalent circuits, either the parallel connection $R//CPE$ presented before or a number N of $R//C$ elements, as proposed by Schoenleber et al. [34] and depicted in Fig. 2.20.

The lack of uniqueness between electrochemical systems and their equivalent circuit represents the greatest limitation of this approach, because wrong conclusions could be drawn. Following the example given by Schoenleber [34], a Nyquist plot of an electric circuit consisting

of resistors, capacitors and inductors, was obtained. Afterwards it is demonstrated that the obtained Nyquist plot can be fitted by a series connection of $R//C$ elements. Moreover, the quality of the fitting can be increased by increasing the number of the $R//C$ elements. The analogy as a basis for the characterisation thus proves to be insufficient. If EIS ought to be implemented to determine the conductivities L_{ij}, another approach must be introduced, rather than applying the established equivalent circuit method.

Chapter 3

Electrolyte materials

The performance of fuel cells as explained in Sec. 2.1 is constrained by technical issues, since it is very difficult to find or develop materials that fit all of the requirements. Since this thesis focuses on electrolytes, several materials, both state of the art materials and recently discovered materials will be explained in this chapter, along with their advantages and disadvantages. Special focus will be given to the electrolyte materials that are to be modeled and characterised in the following chapters, i.e. 3YSZ as a solid oxide electrolyte for high temperature fuel cells and electrolysers (SOFC) and Nafion®as a polymer electrolyte for low temperature fuel cells and eletrolysers (PEM).

3.1 The solid oxide electrolyte

Ions are conducted in solid oxides via defect hopping mechanisms [23]. The defect density in natural oxides is, however, low. In order to increase this density, ceramic oxides are doped with small quantities of other ceramics. Even doped oxides present a low ionic conductivity at ambient conditions, a quality that increases at increasing temperatures. They become suitable as ion conductors at temperatures of $1000 - 1300\,\mathrm{K}$, that is why they are colloquially known as *high temperature* fuel cells. Although this fact reduces their suitability for some applications, it turns out to be a kinetic advantage when compared to PEM fuel cells, presenting significantly lower activation overpotentials. Moreover, at such temperatures there is a wider range of inexpensive catalysts for the electrodes' reactions.
The defects caused by the doping process can promote ionic or electronic conductivity or both. Widespread ceramics like YSZ (yttria-stabilized zirconia) or GDC (gadolinia-doped ceria) are anion conducting. While YSZ presents excellent chemical inertness and stability, as well as high fracture toughness and negligible electronic conductivity [23], GDC shows a significant

higher ionic conductivity, which brings along a high electronic conductivity under reducing conditions, a fact that makes them questionable on behalf of its applicability in fuel cells. To overcome this difficulty, YSZ/GDC multilayers electrolytes have been introduced, achieving power densities of $400\,\mathrm{mW/cm^2}$ [35] at $T = 673\,\mathrm{K}$. Furthermore, other multilayer electrolytes, i.e. BSFSb-SDC, have shown power densities of over $1000\,\mathrm{mW/cm^2}$ at $T = 823\,\mathrm{K}$. On the other hand, there are also proton conducting ceramics, like established YCB and YZB (yttria and ceria-stabilized baria and yttria and zirconia-stabilized baria) and $Ba_7Nb_4MoO_{20}$ which is in a developing stage [36]. These materials will be explained in Sec. 3.1.3.

3.1.1 Yttria stabilized zirconia (YSZ)

As already mentioned, yttria-stabilized zirconia is the state of the art electrolyte for solid oxide fuel cells. Small amounts of yttrium oxide (usually no more than 10% Vol.) are mixed with zirconium oxide to obtain the precursor powder. A zirconium atom becomes chemical stable by bonding to four oxygen atoms, i.e. Zr^{4+}, whereas an yttrium atom only needs three for the same purpose Y^{3+}. By incorporating small amounts of yttrium oxide in the zirconium oxide, yttrium atoms replace some zirconium in the crystal structure. To maintain the electrical neutrality, the oxygen atoms must *jump* through the lattice, as observed in Fig. 3.1. Thus, doping these oxides increases the defect density, increasing the ionic conductivity of the ceramic. Increasing the dopant concentration increases the ionic conductivity until a certain maximum, after which conductivity decreases again; this value lies between $4 - 10\%$ depending on the author [23], [37]. Several theories explaining this behaviour have been proposed, going beyond the scope of this thesis.

Preserving electroneutrality in the doped ceramic means that for every oxygen being incorporated to the oxide (and producing an excess or deficit of charge) electron holes must be produced, allowing electronic conduction. In the Kröger-Vink notation this doping process can be expressed:

$$Y_2O_3 \longleftrightarrow 2\,Y' + V_O^{\bullet\bullet} + 3\,O_O^{\times} \tag{3.1}$$

As previously mentioned, the ionic conductivity of solid oxides is strongly dependent on temperature, a fact that can be modeled with the Arrhenius equation:

$$\sigma^{\mathrm{E}}T = \sigma_0^{\mathrm{E}} \exp\Big(-\frac{E_{\mathrm{A}}}{RT}\Big) \tag{3.2}$$

This assumption can be observed in light of experimental data, depicted in Fig. 3.2, as the ionic conductivity versus the inverse of temperature. The y-axis is often in a logarithmic

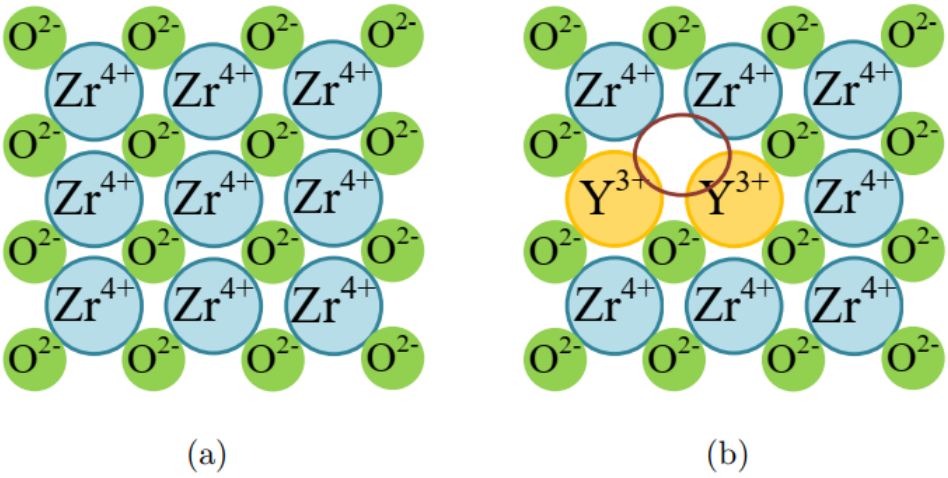

Figure 3.1: Representation of valence for (a) pure ZrO_2 and (b) ZrO_2 doped with Y_2O_3. Figure from Geesmann [38]

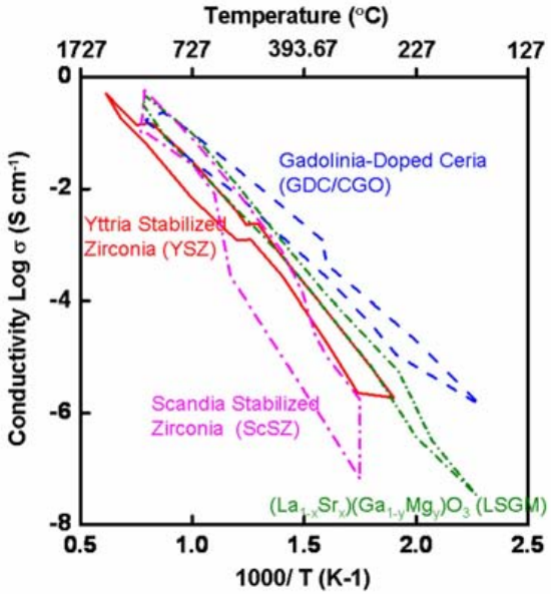

Figure 3.2: Fields of Ionic conductivity σ of different solid oxides versus temperature according to Guan and Liu [39].

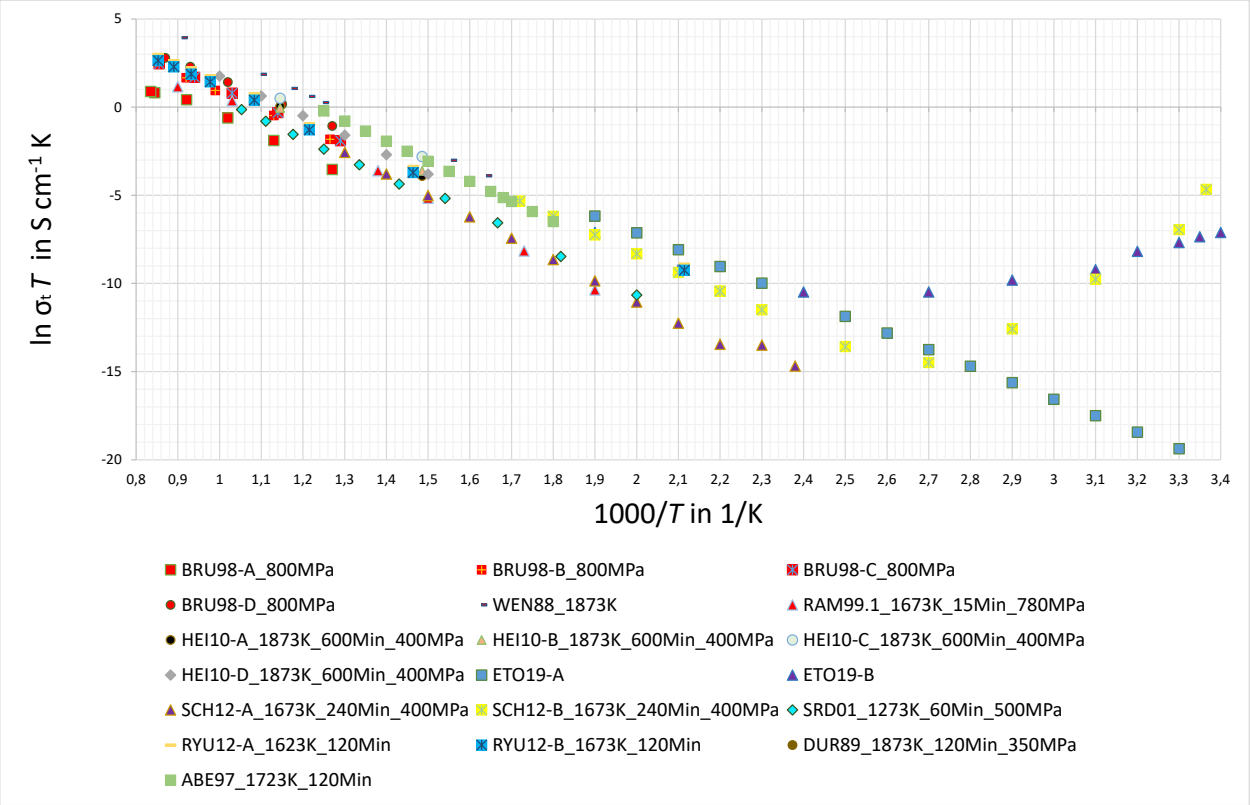

Figure 3.3: Literature reported values for the total conductivity of 3YSZ, showing the data scattering and a possible linear fit. Figure designed by Aldesoki [40] and modified afterwards for this thesis. Raw data from Brune et al. (BRU98) [41], Heiroth et al. (HEI10) [42], Scherrer et al. (SCH12) [43], Ryu et al. (RYU12) [44], Abend et al. (ABE97) [45], Etoh et al. (ETO19) [46], Duran et al. (DUR89) [47], Weller et al. (WEN88) [48], Ram et al (RAM99) [49] and Srdic et al. (SRD01) [50]

scale to show the exponential dependence and the x-axis is usually enlarged by a factor 10^3 for convenience. As it can be observed, fields rather than lines are depicted: the reported values are scattered in the literature. It is believed that the manufacturing process of both the precursor powder and the pellet influence the electrical and mechanical properties of the electrolyte. The data scatter can be observed in Fig. 3.3.

3.1.2 Other anion conducting solid oxides

Doped ceria presents a higher ionic conductivity than stabilized zirconia. Cerium oxide CeO_2 is usually doped with samarium Sm or gadolinium Gd, achieving a maximum conductivity at dopant concentrations of $10 - 20\%$, after which it decreases at increasing concentrations. As explained by O'Hayre et al [23], if the dopant concentration is too high, a high interaction between ions takes place as a result of an elastic tension caused by the mismatch between the

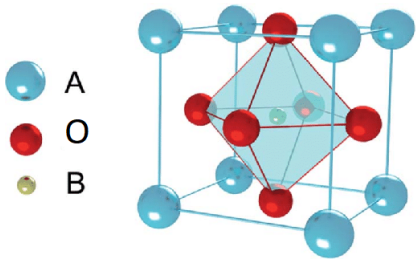

Figure 3.4: Lattice structure of a perovskite with the general formula ABO_3 according to Chen et al. [51].

size of dopant ion and host ion. Thus, to achieve high ionic conductivity, the crystal lattice must remain as unchanged as possible and the doping ion must have a similar size to the host ion. In that sense GDC lattice is more homogeneous than the YSZ one.
Nevertheless, GDC also presents disadvantages: the reducing ambient of the cathode promotes the reaction $Ce^{4+} + e^- \rightarrow Ce^{3+}$ at the expense of the oxygen ion formation. Moreover, the thermal expansion coefficient of cerium oxide increases in reducing conditions, resulting in possible breakdown. This fact also limits the development of multilayer electrolytes, since the different thermal expansion of both YSZ and GDC introduces a possible failure, as well as the extra contact resistance.
Another oxide structure acting as a promising ion conducting material is given by perovskites, which follow the general formula ABO_3, being A and B the metal atoms and O is the oxygen. [36] Its lattice structure can be seen in Fig. 3.4
Depending on the dopant, perovskites can conduct oxygen anions and/or protons. Proton conducting perovskites will be dealt with in the next section. One of the most extensively studied oxides is lanthanum gallate ($LaGaO_3$), whose high ionic conductivity is achieved by replacing some lanthanum atoms by strontium, calcium or barium atoms. The *minimum* lattice distortion rule previously discussed seems to apply also for this material, so that strontium emerges as the most suitable choice. The oxygen vacancy can further be increased by adding divalent cations, such as Mg^{2+}, to replace some gallium. This leads to a family of complex oxides known as LSGM, general formula $La_{1-x}Sr_xGa_{1-y}Mg_yO_{3-\delta}$. [23]. LSGM conductivity lies between the conductivity of YSZ and GDC, being more expensive than GDC but more resistant to reduction. Furthermore, its thermal expansion properties are similar to the ones of YSZ, presenting less mechanical issues. However, the main disadvantages of LSGM are given by its chemical reactivity: it reacts with the common materials for electrodes, such as nickel in the anode and cathode materials under oxidizing conditions.
Another promising family of materials is associated to polymorphism, the existence of more than one crystal structure, like bismut oxide (Bi_2O_3) and the family of LAMOX compounds

($La_2Mo_2O_9$). Bismut oxide presents a monoclinic structure α at room temperature that turns into a cubic type δ when heated above $T = 1000\,\mathrm{K}$. This configuration has a much higher ionic conductivity than the α structure. Doping the oxide with rare elements (Y,Dy,Er) has proved successful to stabilize the high temperature phase at low temperatures. [23] Nevertheless, they are unstable at temperatures below $T = 700\,\mathrm{K}$, being up to date not suitable for intermediate temperature applications. LAMOX, as well as bismute oxides, change their phase at $T \approx 900\,\mathrm{K}$ increasing its ionic conductivity. Similarly, the stabilization of this high temperature phase at lower temperatures becomes possible by doping with elements like $\mathrm{Bi}, \mathrm{W}, \mathrm{V}$. The main difference is given by the conduction mechanism, known as lone-pair substitution (LPS). It consists of a valence electron not shared nor coupled to other atoms [23], which in this case are believed to act as structural elements of the crystal [52]. LAMOX compounds are in a developing stage, facing challenges related to their reduction easiness and degradation.

3.1.3 Proton conducting solid oxides

Among proton conducting solid oxides it can be distinguished between perovskites and perovskites derivatives.
Among perovskites the proton conduction is obtained from the hydration of the oxide[36]:

$$\mathrm{H_2O} + \mathrm{V_O^{\bullet\bullet}} + \mathrm{O_O^{\times}} \longleftrightarrow 2\,\mathrm{OH_O^{\bullet}}\,. \tag{3.3}$$

so that water molecules place themselves in the oxygen vacancies in the lattice, releasing protons $\mathrm{H^+}$; the protons are not entirely free, since they are bonded to oxygen ions in hydroxyl ions $\mathrm{OH^{\bullet}}$. This binding energy is, nevertheless, not large, so that the protons can jump from one oxygen ion to its neighbour. The process can be considered as lattice diffusion similar to oxygen motion rather than the vehicle mechanism proposed in polymers (see Sec. 3.2). Their highest conductivities are seen at intermediate temperatures, above which the anion conductivity becomes dominant [23]. Widespread perovskites proton conducting oxides are $BaCeO_3$ and $BaZrO_3$ doped with Y, Yb, Er, Mo [36].
Derivatives of perovskites can be formed by introducing defects or layering the ABO_3 lattice with structural motifs [36]. Hexagonal perovskites are obtained from mixing face-sharing and corner-sharing BO_6 octahedra, which previously resulted from piling up hexagonal and cubic layers of AO_3. Among this group of perovskites it is worth mentioning $Ba_7Nb_4MoO_{20}$ and $Ba_eEr_2ZrO_{13}$, which become proton conducting when hydrated, being their main disadvantage their mixed conductivity. Ruddlesden–Popper (RP) structures are promising perovskites with

the general formula $A_{n+1}B_nO_{3n+1}$. RP oxides are obtained alternating n layers of corner-sharing BO_6 octahedra with AO layers.[36] Relevant for fuel cells due to good chemical and mechanical properties are RP oxides of the types A_2BO_4 or $A_3B_2O_7$ (with $A = Sr, La, Nd, Pr$ and $B = Fe, Ni$) which present triple conductivity, ie. protonic, electronic and anionic, being suitable for the interface electrode-electrolyte. Last but not least, brownmillerite perovskites ($A_2B_2O_5$) result in layers of corner-sharing octahedra and tetrahedra formed in ordered rows. In this group $Ba_2In_2O_5$ can be named, usually doped with silicate, phosphate or sulphate; its electronic conductivity as well as its chemical and mechanical instability makes it unsuitable for fuel cell applications.

3.2 The polymer electrolyte

Ionic conduction in polymers is not as easily understandable as in oxides. The widespread theory of chain conduction is based on attraction and repulsion of charge sites depending on their polarisation, as well as the availability of free volume: if a high cationic conductivity is desired, the polymer should present a high density of negative charged sites, so that one site attract the cation and the motion occurs when the next charged site obtains the cation from its neighbour. The ions need the polymer to present free volume in its lattice, so that they can *jump* from one charged site to the next one; completely dense polymers are not suitable for this purpose. However, most polymers do present certain free volume. Similar to doping oxides, increasing the density of charged sites increases the ionic conductivity but decreases mechanical stability [23].

Another possible explanation for ionic conduction in polymers is the vehicle mechanism. The vehicle mechanism is based on the transport of other species through the free volume of the polymer. The other species called the *vehicle*, gives the ions a *ride*, i.e. it takes the ions with them. One of the most common vehicles in polymers is water; if the ion motion is given exclusively by water molecules, the conduction process can be modeled analogously to aqueous electrolytes [23]. Both mechanisms are depicted in Fig. 3.5 (b).

There is only a limited selection of polymers used in PEMFC electrolytes. The widespread material is a perfluorinated polymer, commercially known as Nafion, which will be explained in detail in the following section. Other established and promising polymers are presented in Sec. 3.2.2.

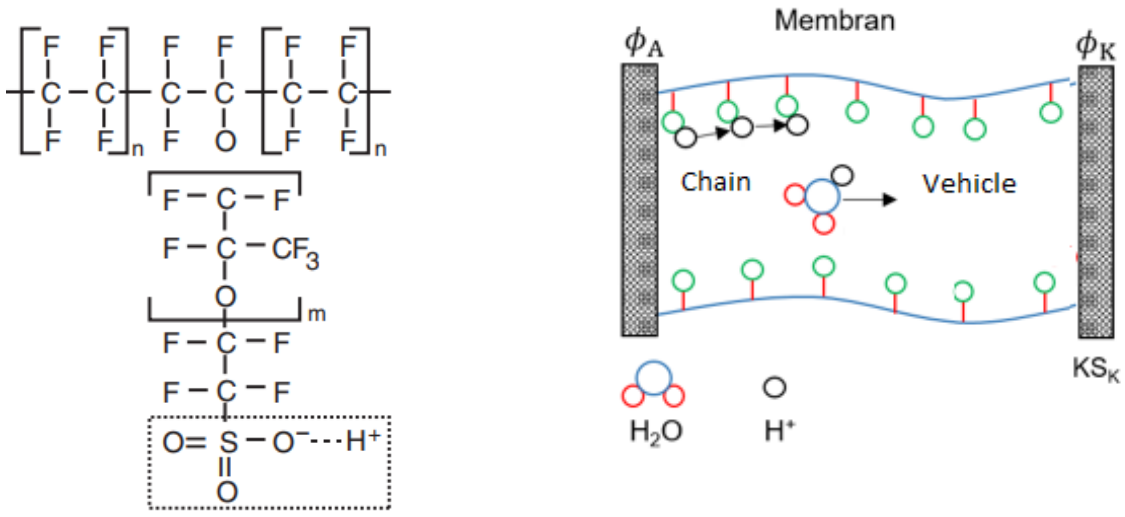

(a) Structure of Nafion

(b) Proposed conduction mechanisms in Nafion: chain mechanism top left and vehicle mechanism in the center.

Figure 3.5: Schematic representation of Nafion, according to O'Hayre et al. [23] and Gottschalk [53].

3.2.1 Nafion®

Perfluorinated polymers like Nafion are the *state of the art* electrolyte for PEM and direct methanol fuel cells [54]. Nafion is a brand name, originally developed by Dow Chemicals. Its structure consists of a modification of polytetrafluoroethylene, better known as Teflon® adding sulphonic acid functional groups, $SO_3^-H^+$, as it can be seen in Fig. 3.5 (a).

The teflon forms a backbone for mechanical strength, and the sulphonic acid groups add charge sites for the ionic conductivity [55]. It is considered that both the chain and the vehicle mechanisms contribute to the conductivity of Nafion, where the free volumes form paths big enough for water molecules to move, while the walls of these paths become polarised with the sulphonic acid chains. If the polymer is well hydrated, the protons H^+ abandon the sulphonic ion SO_3^- to form hydronium H_3O^+, leaving the acidic chain. If enough water is present in the polymer, the ions move inside the polymer exclusively through water, as if the polymer were aqueous, thus exhibiting an ionic conductivity comparable to aqueous electrolytes. Moreover, the teflon molecules that care for the mechanical stability are hidrophobic, so that they increase the formation of paths and the transport of water by repelling the water molecules. Thus, this dependency of ionic conductivity on hydration is defined as the water content λ^M. From the NET perspective, this an important example of coupled processes and can therefore be modeled favourably following Eq. 2.41.

One of the most famous studies of Nafion was carried out at Los Alamos National Laboratory (USA) by the research group of Zawodzinski and Springer. The water content λ^M is defined

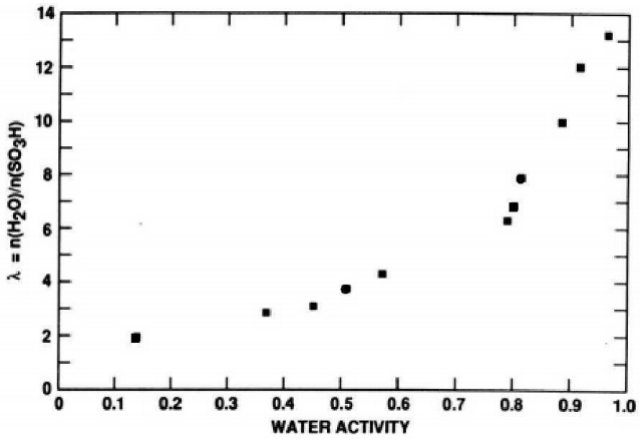

Figure 3.6: Experimental results for nafion N117 membrane water content λ^{M} versus water activity $a_{\mathrm{w}} = \frac{p_{\mathrm{W}}}{p_{\mathrm{W}}^{\mathrm{S}}}$ at $T = 303\,\mathrm{K}$, given by Zawodzinski et al. [56].

as the ratio of the number of water molecules to the number of charge $SO_3^-H^+$ sites.[12] Zawodzinski et al. [56] measured the dependency of water content on the water activity a_{H_2O} for a N117 membrane at $T = 303\,\mathrm{K}$ and their results are depicted as dots in Fig. 3.6. The referred activity a is the thermodynamical activity, which in this case is approximated to the fugacity for gases, i.e. the ratio of the partial pressure of water and the saturation pressure of water at the same temperature. The water saturation of nafion depends on the water phase, showing a much higher saturation when in equilibrium with liquid water ($\lambda^{\mathrm{M}} = 22$) than with water vapour ($\lambda^{\mathrm{M}} = 14$). Later on, his colleague Springer et al. [12] proposed a polynomial of third grade (continuous line in Fig. 3.7) to approximate the isothermal at $T = 303\,\mathrm{K}$ for the vapour equilibrium:

$$\lambda^{\mathrm{M}}(T = 303\,\mathrm{K}) = 0.043 + 17.81a - 39.25a^2 + 36a^3 \qquad \text{for } 0 < a < 1. \tag{3.4}$$

Although the curve was obtained only for one temperature, they considered it to be also applicable to higher temperatures. The group [56] also measured the ionic conductivity σ^{M} at different water activities and by fitting the data it was obtained: $T = 303\,\mathrm{K}$:

$$\sigma^{\mathrm{M},303} = 0.5139\lambda^{\mathrm{M}} - 0.326 \qquad \text{for } \lambda^{\mathrm{M}} > 1. \tag{3.5}$$

The coupling of water flux and ions motion plays a role in the conductivity, which was defined by the transference number t, commonly used in diffusion in solids. The transference number, in this case, represents the number of water molecules dragged per proton H^+. [56] Springer, Zawodzinski et al. [12] estimated the transference number proportional to the water

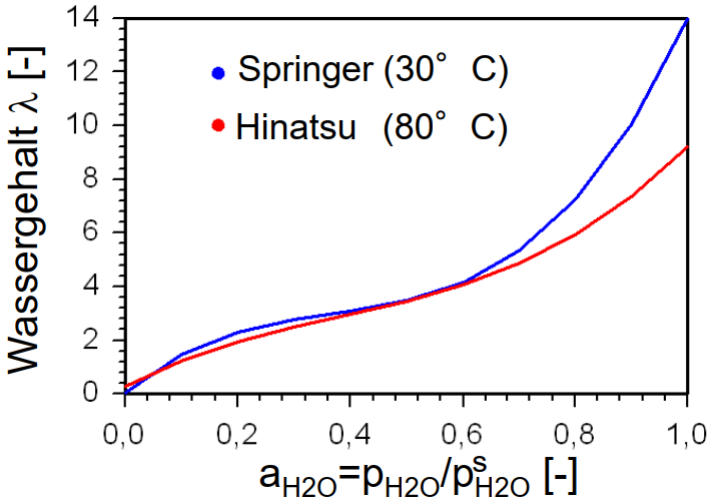

Figure 3.7: Approximation of nafion membrane water content on water activity for $T = 303\,\mathrm{K}$ by Springer [12], Eq. 3.4 and $T = 353\,\mathrm{K}$ by Hinatsu [57], Eq. 3.8

content from two measurements at $T = 303, 323\,\mathrm{K}$:

$$t = \frac{2.5}{22}\lambda^{\mathrm{M}}, \tag{3.6}$$

based on the water content of $t = 2.5$ measured from a membrane in equilibrium with liquid water, $\lambda^{\mathrm{M}} = 22$. Later on, Fuller and Newman [58] obtained a completely different curve for $t = f(\lambda^{\mathrm{M}})$ in equilibrium with water vapour at $T = 298\,\mathrm{K}$, which made Los Alamos measure the transport number for the same water activity range, so that Zawodzinski, Davey et al [59] obtained a constant value of $t = 1.03$ at $T = 303\,\mathrm{K}$ independent of water content, refuting the previous approximation. The approaches are depicted in Fig. 3.8. As for the ionic conductivity, it was proposed to be exponentially dependent on temperature, similar to an Arrhenius equation, as previously explained in Sec. 3.1.1. By measuring the conductivity of fully hydrated membranes for two temperatures, an activation energy was obtained and assumed to hold for all temperatures:

$$\sigma^{\mathrm{M}}(T) = \sigma^{\mathrm{M},303} \exp\left[1268\left(\frac{1}{303} - \frac{1}{T}\right)\right] \tag{3.7}$$

Other studies, e.g. Hinatsu et al., [57] have measured the water content dependency on water activity at $T = 353\,\mathrm{K}$ for N117, proposing the following Equation:

$$\lambda^{\mathrm{M}}(T = 353\,\mathrm{K}) = 0.300 + 10.8a - 16.0a^2 + 14.1a^3 \qquad \text{for } 0 < a < 1, \tag{3.8}$$

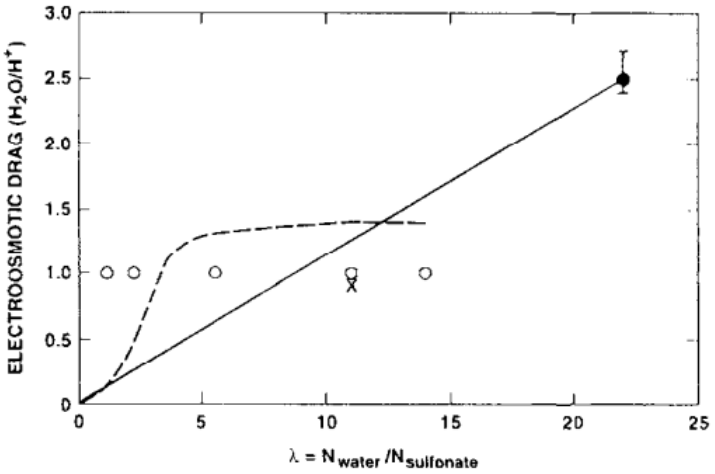

Figure 3.8: Transference number t of a Nafion membrane vs. water content λ^{M}. (-) the approach of Springer [12], Eq. 3.6 (-.-) the approach of Fuller and Newman [58] and (o) the approach of Zawodzinski [59].

showing that the assumption of water content dependence on water activity proposed in Eq. 3.4 for the temperature range $303 \leq T \leq 353$ does not necessarily hold true, as depicted in Fig. 3.7. As pointed out by Maldonado Sanchez [60], pre-treatment history plays a key role in the water sorption of nafion: drying the membrane at temperatures $T > 370\,\mathrm{K}$ sets a maximum water content at a certain water activity, which can be overcome by avoiding previous thermal treatments.

Moreover, the linear dependence of ionic conductivity on water content from Eq. 3.5 contrasts with the polynomial second grade proposed by Neubrand [62] given by Eq. 3.9, as it can be seen in Fig. 3.9. It becomes necessary to investigate polymer electrolytes in a more formal manner, since empirical equations are too scattered. Non-Equilibrium Thermodynamics might overcome this difficulty.

$$\sigma^{\mathrm{M}} = 0.03637(\lambda^{\mathrm{M}})^2 + 0.14177\lambda^{\mathrm{M}} - 0.034 \tag{3.9}$$

As mentioned before, the properties of Nafion membranes, e.g. water content, are dependent on factors like thermal history or preparation procedure. The N117 membrane, which has been described so far, is obtained by (melt) extrusion. This procedure contributes to its mechanical strength but increases its ionic resistance. If the Nafion electrolyte is prepared by dispersion casting, e.g. Nafion N211, thinner membranes are obtained, presenting a higher ionic conductivity but also a higher hydrogen crossover. The water content dependence on water activity for N211 was measured by Peron et al. [63] and is given in Fig. 3.10. It can be seen that, when compared to N117, a larger water sorption is obtained. Moreover, a greater

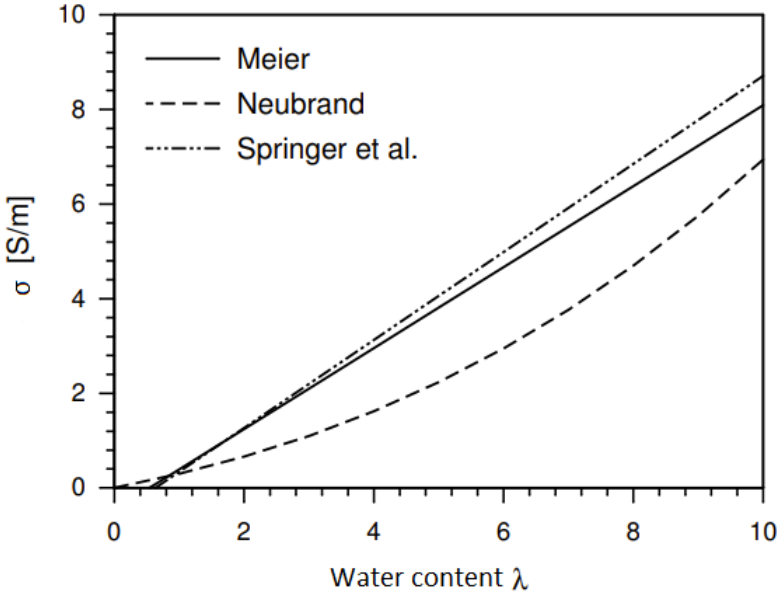

Figure 3.9: Ionic conductivity dependency on water content, according to Siemer [61].

ionic conductivity was also measured, as depicted in Fig. 3.11.

3.2.2 Other polymer electrolyte materials

One alternative to Nafion is given by polyetheretherketones (PEEKs), which make use of aromatic hydrocarbon polymers instead of perfluorinated polymers for the backbone, making the polymer less expensive and more environmental friendly (they are easier to recycle) and improving the water sorption of the electrolyte, since their density of polar groups is higher. Also they can be implemented at higher temperatures. On the other hand, PEEK has a poorer chemical and thermal stability as well as a higher ionic resistance when compared to nafion operation temperatures. In this case, the polymer results from ether and kethone units and the ionic conductivity is obtained by adding sulphonic acid functional groups, similar to nafion. Nevertheless, at temperatures of $T = 333 - 353\,\mathrm{K}$, PEEKs show a lower protonic conductivity, [64] around 30% of Nafion, which increases up to 50% when additives, such as phosphotungstic acid (PWA), are incorporated. At (PEM) high temperatures of $T > 420\,\mathrm{K}$ nafion and PEEKs show a similar ionic conductivity [23].
Following aromatic hydrocarbon based polymers, it is worth mentioning another material, the phosphoric acid doped polybenzimidazole (PBI). Its structure is similar to PEEK but the adding sulphuric acid to the hydrocarbon, a strong acid like phosphoric acid (H_3PO_4). The conduction mechanism does not rely on the sulphonic functional groups but on the interplay

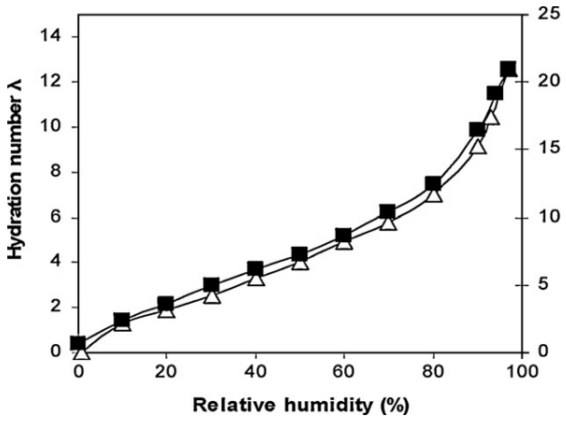

Figure 3.10: Water content dependency on water activity, according to Peron et al. [63]

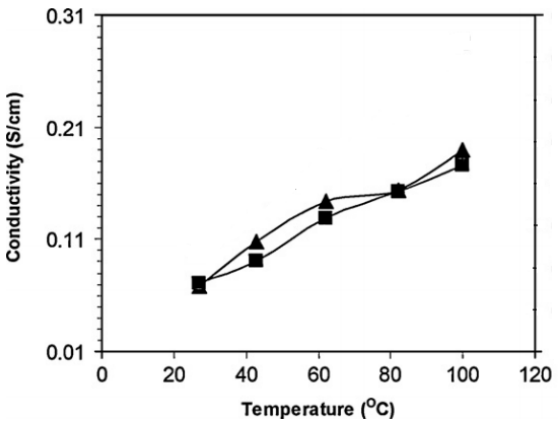

Figure 3.11: Ionic conductivity dependency on temperature, according to Peron et al. [63]

base-acid, since the polymer is relatively basic and the acid is a strong one; the conduction is believed to occur via the vehicle mechanism, free of acid [23]. When compared to Nafion it shows several advantages, such as its ionic conductivity is similar but almost independent on water content, a better thermal and mechanical stability and its extremely lower cost. On the other hand, the acidic environment reduces its durability and the kinetic of the cathodic reaction; finding suitable catalysts is also challeging.

Last but not least, the doping of nafion with inorganic substances has been tried, giving birth to polymer-inorganic composite membranes. It can be achieved by either incorporating hydroscopic oxides (like silica or titania) to increase water uptake (by increasing the operation temperature) or by adding proton-conducting materials (such as phosphates or heteropolyacids) to reduce the ionic resistance. Even though these composites improve water sorption, its ionic conductivity lies still below that of nafion and they are just as dependent on hydration as nafion [23].

Chapter 4

Modeling the electrolyte

This chapter presents the implementation of Non-Equilibrium Thermodynamics to model the transport mechanisms within electrolytes, which are the objects of this thesis. The solid oxide electrolyte consists of a 3%mol yttrium oxide stabilized zirconium oxide, commonly known as yttria-stabilized zirconia with the composition $(Y_2O_3)_{0.03}(ZrO_2)_{0.97}$. The samples consists of pellets of 5 mm and 10 mm, having an active area of $(40 \cdot 40)$ mm.
The polymer electrolyte consists of Nafion membranes of the type N1110, which is extruded. Thus they belong to the N117 family, which is the most characterised membrane so far. The electrolyte has a thickness of $d^{\mathrm{M}} = 1.27$ mm, more details can be found in Sec. 5.2.1.

4.1 Modeling the solid oxide electrolyte

This section is based on previously published works, one poster at the European Fuel Cell Forum 2020 and one manuscript in the Journal *Solid State Ionics* [65] with the title *A novel method to determine the transport coefficients of an YSZ electrolyte based on impedance spectroscopy.*

4.1.1 EIS applied to 3YSZ electrolytes

A real YSZ electrolyte cannot be directly used for electrical characterisation using EIS, since the solid oxide does not conduct electricity, thus making it necessary to create an electric contact. Since at both surfaces of the electrolyte the ions might readily be formed and adsorbed, it is important to use a compatible metal for the electric contact, one that can work both as contact and catalyst of the ion formation. Among the most used metals are

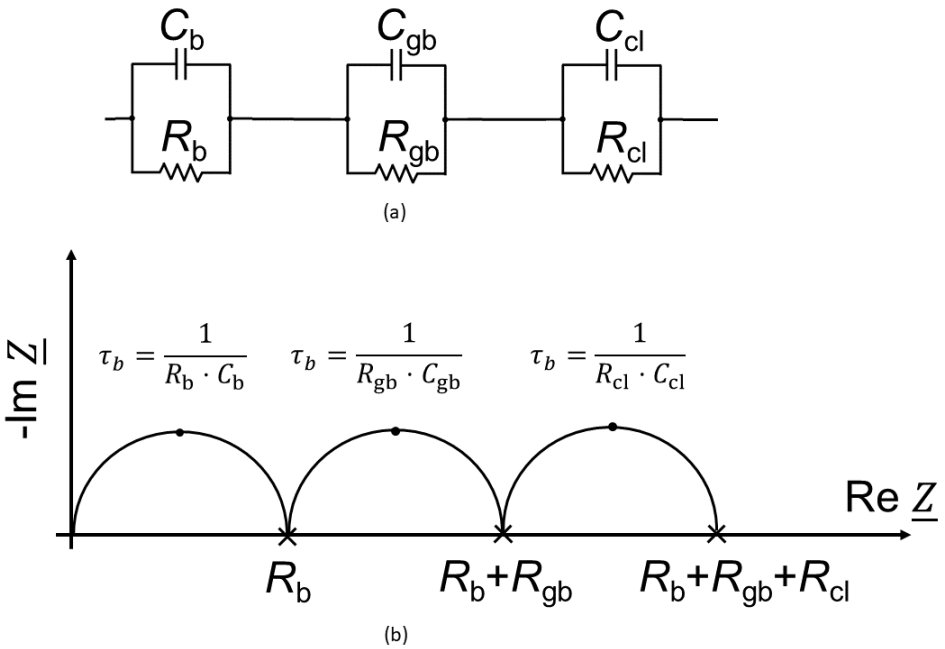

Figure 4.1: Model of a single cell with symmetric electrodes and a YSZ-electrolyte [66]. (a) Equivalent circuit and (b) Resulting Nyquist-Plot when EIS is measured.

worth mentioning, gold, [67], [68] silver [69] and platinum [70].

This test object can be, in the simplest case, approximated by an equivalent circuit of three $R//C$ elements in series; every element consisting of a resistance R connected to a capacitor C in parallel, as depicted in Fig. 4.1 (a). As mentioned in Sec. 2.8.1, when EIS is applied to a $R//C$ element, this results in a semicircle in the Nyquist plot. Therefore the 3YSZ electrolyte should show a Nyquist plot similar to the one observed in Fig. 4.1 (b). However, one condition must be accomplished: the relaxation times $\tau = \frac{1}{R \cdot C}$ of the electrochemical processes must be separated from each other at least by one order of magnitude, [17] ideally three orders.

The three elements represent the bulk conductivity σ_{b}, the grain boundary conductivity σ_{gb} and the catalyst layer conductivity σ_{cl} or interface Me | YSZ or YSZ | Me, with Me = Au, Ag, Pt, i.e. where the process $\frac{1}{2}\mathrm{O}_2 \rightleftharpoons \mathrm{O}^{2-}$ takes place. Real examples of these three semicircles are scarce in the literature, eg. the Nyquist Plot of a 3YSZ electrolyte with Pt-electrodes measured at $T = 973\,\mathrm{K}$ by Lee et al [33]. When compared to the theoretical curve shown in Fig. 4.1 (b), one arc instead of three semicircles is seen in the experimental result. There are some factors that influences the shape and size of the semicircles obtained in experimental studies:

- Powder preparation: precursors used, organic compounds involved, in some cases: laser

power and wave length.

- Pellet fabrication: sintering method, sintering temperature, pressure applied.
- Crystal structure: cubic, tetragonal, monoclinic, rhombohedric.
- Grain size (associated with the crystal structure).
- Measuring/operating temperature

The effect of all of these factors are beyond the scope of this study, they can, however, help understanding the scattering of the results obtained for the conductivity of YSZ, as previously shown in Fig. 3.3. Only the last factor, ie. the operation temperature will be taken into account, since it is the only one that can be controlled during the experiments.
The arc observed in Fig. 2.18 can be fitted with equivalent circuit presented in Fig. 4.1 (a). In that case, the first semicircle, associated to the bulk impedance is considerably smaller than the grain boundary impedance, while the relaxation time of interface impedance appears to be similar to the conductivity in the grain boundary. When the measuring temperature decreases, the bulk conductivity becomes dominant and the sizes of the semicircles are inverted, as shown by El-sayed Ali et al [71] in Fig. 4.2. Although it is not to be compared quantitatively, as the authors performed their measurements with a 8YSZ electrolyte, the temperature effect is observed. The bulk and grain boundary conductivities dependence on temperature are plotted in Figs. 4.3 and 4.4.

The data from both figures is summed up in Table 4.1, from which it can be seen that the scattering of experimental data for 3YSZ does not only apply for the total ionic conductivity σ (see Fig. 3.3 for reference) but also for the bulk conductivity σ_{b} and for the grain boundary conductivity σ_{gb}, since their reported activation energies are also scattered. The mean bulk activation energy results $(0.84 \pm 0.09)\,\mathrm{eV}$, while the grain boundary activation energy equals $(1.09 \pm 0.11)\,\mathrm{eV}$
As mentioned before, it is beyond the scope of this thesis to determine which factors influence which part of the ionic conductivity. Up to this point and as far as known, there is no conclusive statement in this sense. It has been, however, point out, that both the precursor obtaining process as well as the pellet shaping play a key role in the crystal structure and thus on the ionic conductivity. Nevertheless, different authors have employed similar powders and similar mechanical methods for the pellets to measure a different ionic conductivity. Since the focus of this study lies in the characterisation method, these factors shall not be taken into account. For the purpose of validation the large standard deviation ought to be considered.

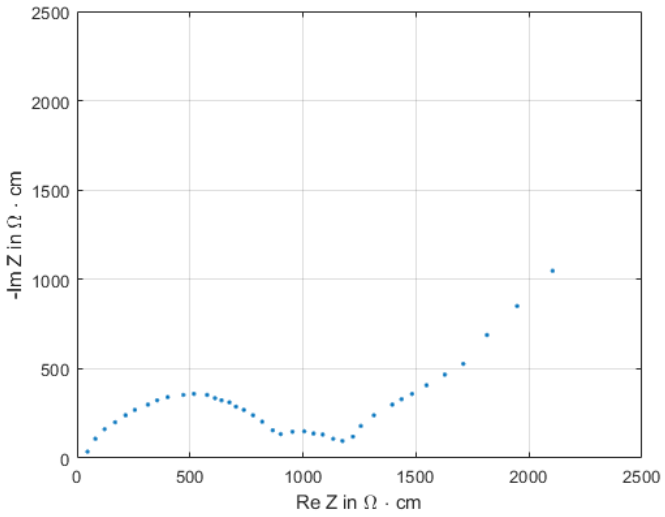

Figure 4.2: Nyquist-Plot of an 8YSZ electrolyte with Pt-electrodes, measured at 773 K, as given by M. El-sayed Ali et al. [71].

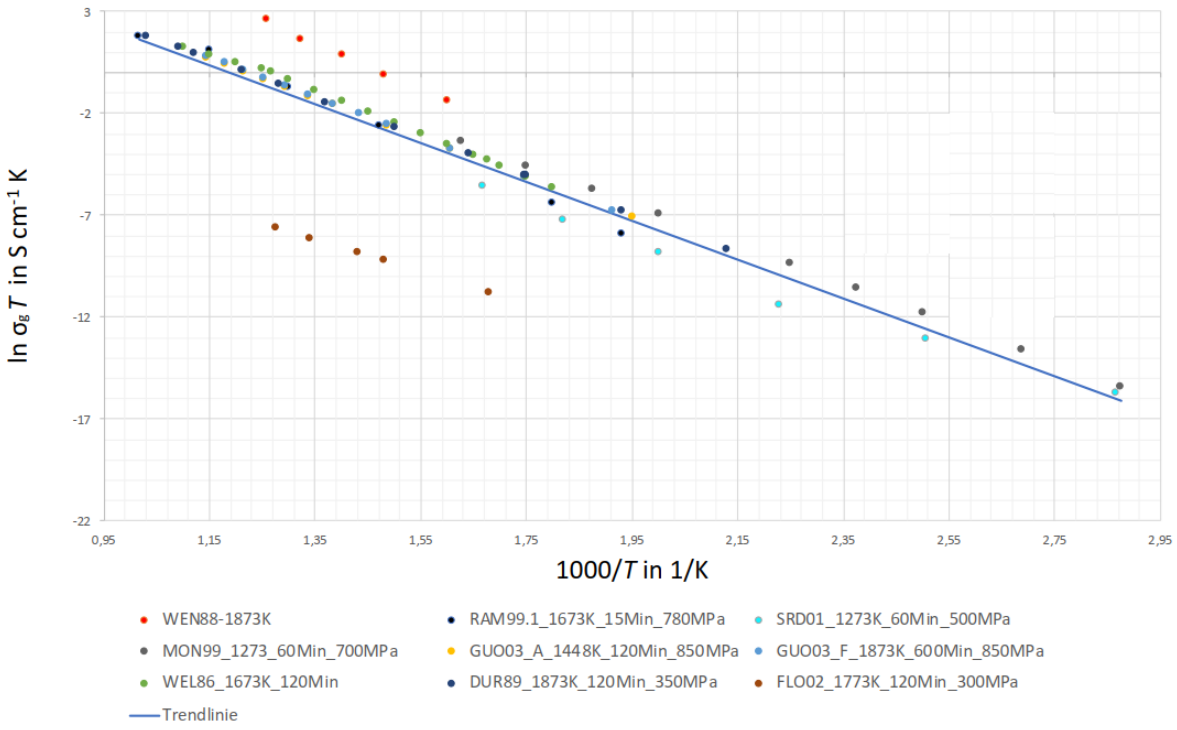

Figure 4.3: Bulk conductivity σ_b vs. temperature for an 3YSZ electrolyte

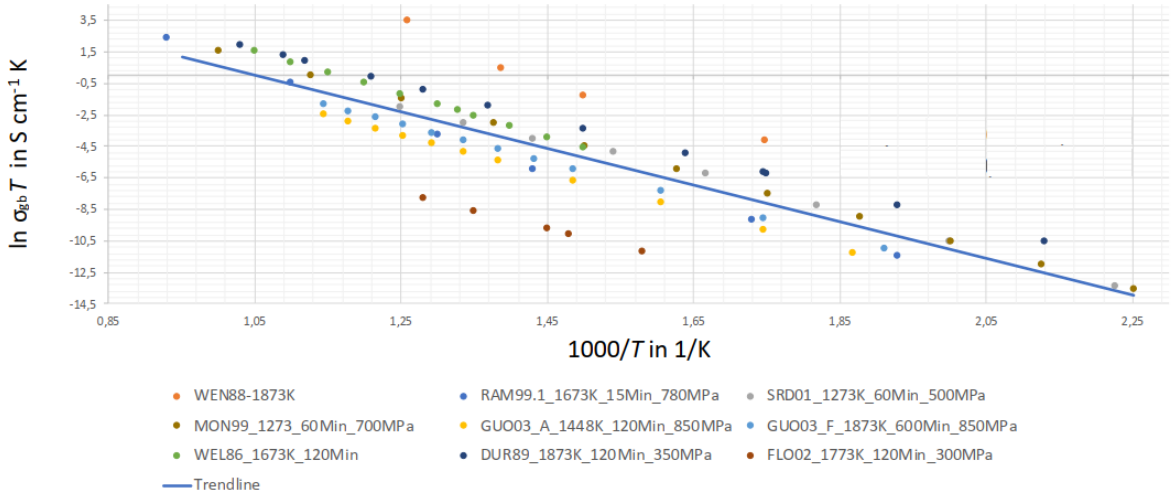

Figure 4.4: Grain boundary conductivity σ_{gb} vs. temperature for an 3YSZ electrolyte

Table 4.1: Activation energies E_{A} in eV found in literature for bulk and grain boundary conductivities

Study	Bulk Activation Energy E_{A}	Grain boundary Activation Energy E_{A}
WEN88 [48]	0.97	1.30
RAM99 [49]	0.97	1.21
SRD01 [50]	0.78	1.00
MON99 [72]	0.83	1.04
GUO03 [73]	0.84-0.85	1.03-1.05
WEL86 [48]	0.62-0.92	1.17
CIA94 [74]	0.91	1.07
FLO02 [75]	0.67	0.99
DUR89 [47]	0.82	0.98

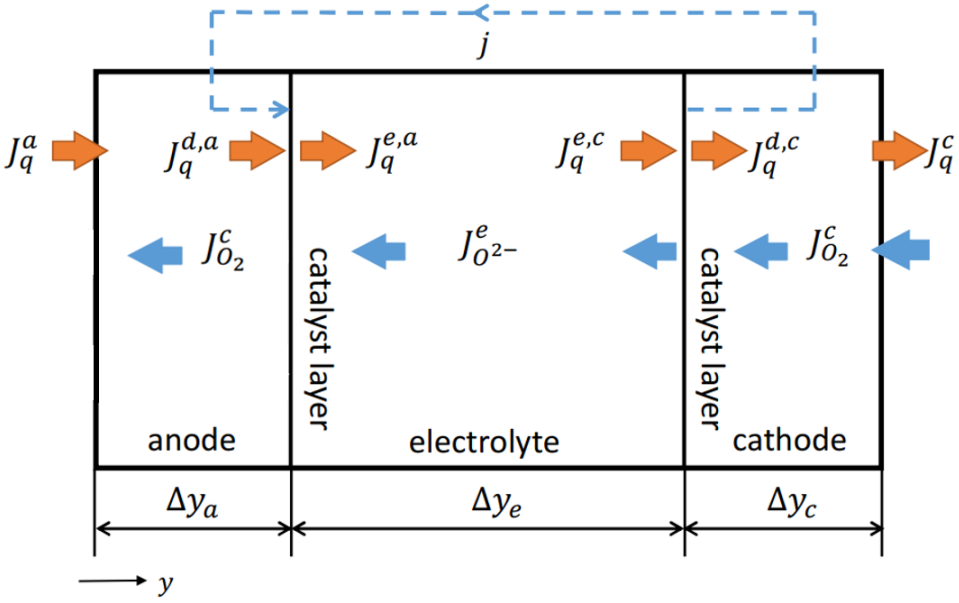

Figure 4.5: Scheme of the fluxes through a solid oxide electrolyte with two oxygen/air electrodes

4.1.2 NET applied to 3YSZ electrolytes

The starting point to derive the model equations to describe the transport mechanisms of fluxes within the frame of Non-Equilibrium Thermodynamics are Eqs. 2.42-2.44. Due to the conservation of charge, the electronic current $\boldsymbol{j}$ measured externally(anode to cathode) must equal to the sum of electronic current and ionic currents $\sum \boldsymbol{J}_\mathrm{k}$, where k stands for every possible type of ion. In the case of YSZ $k = \mathrm{Zr}^{4+}, \mathrm{Y}^{3+}, \mathrm{O}^{2-}$[76]. Nevertheless, for the temperatures studied electronic conductivity is negligible small, as it has been shown in MD simulations [77] as well as experimentally, [78] proving to be at least 3 orders of magnitude smaller than ionic conductivity. Furthermore cation diffusion can also be neglected, [79] since it requires temperatures $T > 2000\,\mathrm{K}$ to be observable [25]. As a consequence, the external current and the anionic current are proportional to each other $\frac{j}{zF} = J_{\mathrm{O}^{2-}}$. As the driving force for the electric current the electrostatic potential shall be expressed as $\mathrm{d}\varphi$ to differentiate it from electric potential $\mathrm{d}\phi$. The relation between electrostatic potential and electric potential is given in the next paragraph. The Eqs. 2.42-2.44 applied to the solid oxide electrolyte returns as:

$$J_\mathrm{q} = -L_\mathrm{qq}\frac{1}{T^2}\frac{\mathrm{d}T}{\mathrm{d}y} - L_\mathrm{qO}\frac{1}{T}\frac{\mathrm{d}\mu_{\mathrm{O}^{2-}}}{\mathrm{d}y} - L_{\mathrm{q}\varphi}\frac{F}{T}\frac{\mathrm{d}\varphi}{\mathrm{d}y}, \tag{4.1}$$

$$J_{\mathrm{O}^{2-}} = -L_\mathrm{Oq}\frac{1}{T^2}\frac{\mathrm{d}T}{\mathrm{d}y} - L_\mathrm{OO}\frac{1}{T}\frac{\mathrm{d}\mu_{\mathrm{O}^{2-}}}{\mathrm{d}y} - L_{\mathrm{O}\varphi}\frac{F}{T}\frac{\mathrm{d}\varphi}{\mathrm{d}y}, \tag{4.2}$$

$$j = -L_{\varphi q}\frac{F}{T^2}\frac{\mathrm{d}T}{\mathrm{d}y} - L_{\phi O}\frac{F}{T}\frac{\mathrm{d}\mu_{O^{2-}}}{\mathrm{d}y} - L_{\varphi\varphi}\frac{F}{T}\frac{\mathrm{d}\varphi}{\mathrm{d}y}. \tag{4.3}$$

As expressed in Sec. 2.5, the electrochemical nature of ions makes Eq. 4.2 equivalent to Eq. 4.3. Aided by the Onsager relations $L_{O\varphi} = L_{\varphi O}$ and $L_{q\varphi} = L_{\varphi q}$, equating coefficients lead to [76] $L_{\varphi\varphi} = z^2 L_{OO}$, $L_{\varphi O} = zL_{OO}$ and $L_{\varphi q} = zL_{Oq}$, reducing the number of coefficients necessary to describe the electrolyte. The electric potential ϕ is defined proportional to the electrochemical potential $\phi = \mu_{O^{2-}}/(zF)$, so that the thermodynamic fluxes can be expressed as [65]:

$$J_q = -L_{qq}\cdot\frac{1}{T^2}\frac{\mathrm{d}T}{\mathrm{d}y} - L_{qO}\cdot\frac{zF}{T}\frac{\mathrm{d}\phi}{\mathrm{d}y}, \tag{4.4}$$

$$J_{O^{2-}} = -L_{Oq}\cdot\frac{1}{T^2}\frac{\mathrm{d}T}{\mathrm{d}y} - L_{OO}\cdot\frac{zF}{T}\frac{\mathrm{d}\phi}{\mathrm{d}y}. \tag{4.5}$$

Let the electrolyte control volume be so macroscopic thin such that the differential of the thermodynamic functions $\varkappa = T, \mu, \phi$ can be considered as differences $\mathrm{d}\varkappa \approx \Delta\varkappa$, ie. the driving forces are independent on the thermodynamic function profile $X_j \neq \varkappa(y)$. In that case, the conductivities L_{ij} can be considered as bulk properties of the electrolyte. Experimentally this means that only small gradients are to be applied to the electrolyte, and that the thickness of the electrolyte approximates its differential $\mathrm{d}y \approx d^E$. The thermodynamic fluxes result then:

$$J_q = -L_{qq}\cdot\frac{1}{T^2}\frac{\Delta T}{d^E} - L_{qO}\cdot\frac{zF}{T}\frac{\Delta\phi}{d^E}, \tag{4.6}$$

$$J_{O^{2-}} = -L_{Oq}\cdot\frac{1}{T^2}\frac{\Delta T}{d^E} - L_{OO}\cdot\frac{zF}{T}\frac{\Delta\phi}{d^E}. \tag{4.7}$$

Making use of the previously stated equality $\frac{j}{zF} = J_{O^{2-}}$, Eq. 4.7 can be rewritten solving for the electric current, which is actually what is measured by performing EIS experiments:

$$j = -L_{Oq}\cdot\frac{zF}{T^2}\frac{\Delta T}{d^E} - L_{OO}\cdot\frac{(zF)^2}{T}\frac{\Delta\phi}{d^E}. \tag{4.8}$$

This implies that by means of EIS it is possible to measure the conductivities L_{OO} and L_{Oq}. If additional conditions are applied, it would be also possible to determine L_{qq}. For example, if the net heat flux J_q in Eq. 4.6 is experimentally set to zero, solving for the temperature difference and then replacing in Eq. 4.8, obtaining:

$$j = -\underbrace{\left(L_{OO} - \frac{L_{Oq}^2}{L_{qq}}\right)\cdot\frac{(zF)^2}{T}}_{\sigma_{\mathrm{eff}}}\cdot\frac{\Delta\phi}{d^E}, \tag{4.9}$$

so that an effective electrical conductivity σ_{eff} can be defined:

$$\sigma_{\text{eff}} = \left(L_{\text{OO}} - \frac{L_{\text{Oq}}^2}{L_{\text{qq}}}\right) \cdot \frac{(zF)^2}{T}. \tag{4.10}$$

Under these circumstances, the measured electrical conductivity is not only dependent on the pure ionic conductivity L_{OO} but also on the cross conductivity L_{Oq} and the thermal conductivity L_{qq}. Most studies do not take this dependency into consideration, so that their measured conductivity might over- or underestimated, misleading the interpretation of results [65].

To prove the feasibility of this approach, the conductivities were first calculated, making use of Molecular Dinamics (MD) simulations for ordered crystals of 8YSZ, i.e., a model for the bulk conductivity alone at $T = 1300\,\text{K}$ and zero pressure. The basic idea consists in extracting the frequency dependency of the impedance (or its inverse, the admittance): if one could determine the impedance curve from the conductivities it is also conceivable that obtaining the conductivities from the impedance curve should be possible. This is one important aspect pursued in this thesis. The comparison of this model to experimental values is limited to single crystals, since the MD simulation only considers the microfluxes in a lattice structure with no disorder, i.e. grain boundaries, between lattice elements.

Heitjans and Indris [80] express the fluctuation-dissipation theorem expressed by the Kubo formula to obtain the frequency-dependent conductivity from the auto correlation function (ACF):

$$\sigma(\omega) = \frac{L^d}{k_{\text{B}} \cdot d} \frac{1}{T} \int_0^\infty \langle j(0) j(t) \rangle \cdot e^{i\omega t}\, \mathrm{d}t, \tag{4.11}$$

where L is the length of the modeled system, d the dimension of the system so that L^d becomes the volume of the system, integrated over time. The auto correlation function (ACF) necessary for this approach was previously obtained from a MD study [37]. In that work, the microfluxes J_{i} are calculated using classical Equilibrium Molecular Dynamics (EMD). Then the auto correlation functions of these fluxes $J_{\text{i}}(0)J_{\text{i}}(t)$ and the cross correlation functions $J_{\text{i}}(0)J_{\text{j}}(t)$ are obtained in a similar manner to the Green-Kubo relations, which provide an expression to determine the phenomenological coefficients or conductivities L_{ij}. [81], [82]

Valadez et al [37] calculated the conductivities L_{ij} using the Green-Kubo formula:

$$L_{\text{ij}} = \frac{V}{3k_{\text{B}}} \int_0^\infty \langle J_{\text{i}}(0) J_{\text{j}}(t) \rangle \mathrm{d}t, \tag{4.12}$$

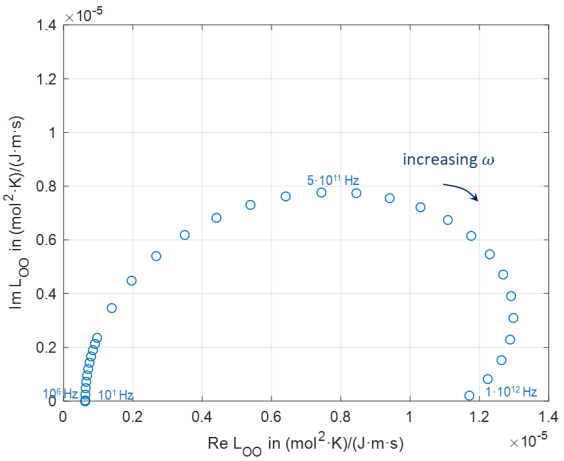

Figure 4.6: Complex ionic transport coefficient L_{OO} dependency on frequency, originally published on *Solid State Ionics* [65]

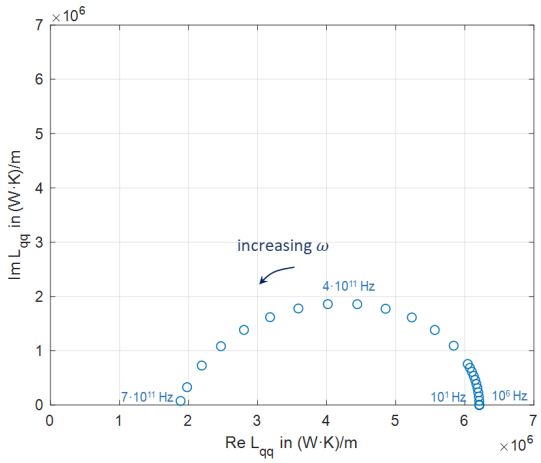

Figure 4.7: Complex thermal energy conductivity L_{qq} dependency on frequency, originally published on *Solid State Ionics* [65]

so that combining both equations results in the frequency dependent conductivities $L_{ij}(\omega)$:

$$L_{ij}(\omega) = \frac{V}{3k_B}\int_0^\infty \langle J_i(0)J_j(t)\rangle e^{i\omega t}dt, \tag{4.13}$$

The conductivity L_{OO} can be obtained from the ACF of the ionic microflux: The first integration attempt was limited to the frequency range technically possible, ie. $10^{-3} < f \text{ in Hz} < 10^6$, which delivered a single dot on the abscissa, as reported in literature for the bulk conductivity of YSZ single crystals at high temperatures ($T > 873\,\text{K}$) [83]. The frequency range was thereafter increased until a semicircle was obtained, as depicted in Fig. 4.6, completing the semicircle at $f = 10^{12}\,\text{Hz}$. This fact shows that the relaxation time at $T = 1300\,\text{K}$ for the bulk conduction is too low for the current EIS devices. Validating this model would require to decrease the operation temperature to increase the relaxation time, thus decreasing the characteristic frequency to the measurable range. Decreasing the temperature would lead to difficulties in obtaining good correlation functions, since the low temperature decreases the ion mobility and the interaction between them within the lattice. In the complex graphical plane, the ionic conductivity L_{OO} shows a bow-alike behaviour, where the high frequency tail decreases its real part.

$$L_{OO}(\omega) = \frac{V}{3k_B}\int_0^\infty \langle J_{O^{2-}}(0)J_{O^{2-}}(t)\rangle e^{i\omega t}dt, \tag{4.14}$$

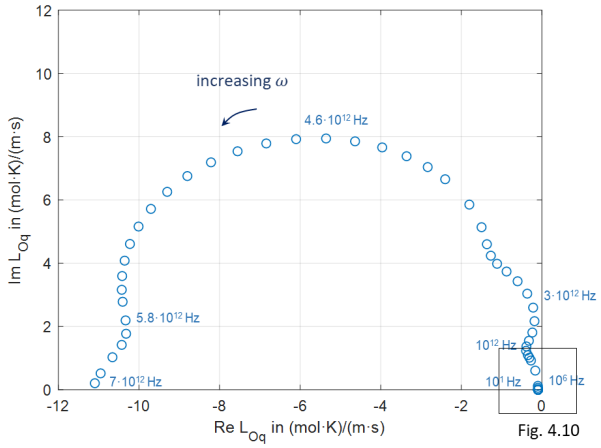

Figure 4.8: Complex cross transport coefficient L_{Oq} dependency on frequency, originally published on *Solid State Ionics* [65]

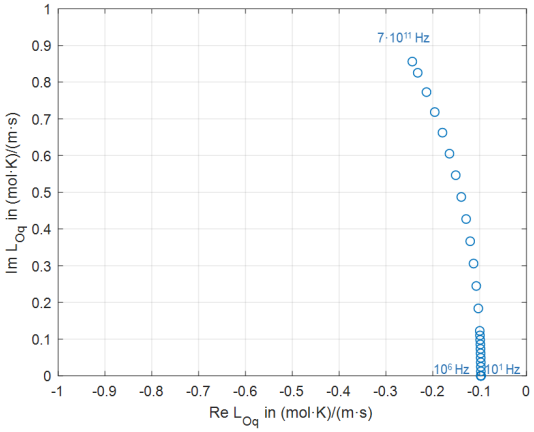

Figure 4.9: Detail of the complex cross transport coefficient L_{Oq}, limited to the common frequency range to the three transport coefficients. Originally published on *Solid State Ionics* [65]

The ACF of the heat microflux delivers the conductivity L_{qq}:

$$L_{\mathrm{qq}}(\omega) = \frac{V}{3k_{\mathrm{B}}} \int_0^\infty \langle J_{\mathrm{q}}(0) J_{\mathrm{q}}(t) \rangle \mathrm{e}^{i\omega t} \mathrm{d}t, \tag{4.15}$$

which was integrated at increasing frequency ranges similarly to L_{OO}, resulting in the curve depicted in Fig. 4.7 for the frequencies $10^1 < f \,\text{in Hz} < 10^{11}$. The direction of L_{qq} at increasing frequencies is the opposite of L_{OO}, which was to be expected from Eq. 4.10, since L_{qq} is in the denominator. If this equation is written in the complex plane, the following Eq. results:

$$\sigma_{\mathrm{eff}} = \left(|L_{\mathrm{OO}}| \cdot \mathrm{e}^{i\phi_{\mathrm{OO}}} - \frac{|L_{\mathrm{Oq}}|^2}{|L_{\mathrm{qq}}|} \cdot \mathrm{e}^{i(2\phi_{\mathrm{Oq}} - \phi_{\mathrm{qq}})} \right) \frac{(zF)^2}{T}, \tag{4.16}$$

so that the contribution of the thermal conductivity L_{qq} to the effective conductivity σ_{eff} increases at increasing frequencies (the module of $|L_{\mathrm{qq}}|$ decreases with increasing frequency, thus its inverse $1/|L_{\mathrm{qq}}|$ increases).

The cross transport coefficient $L_{\mathrm{Oq}} = L_{\mathrm{qO}}$ cannot be directly obtained from the ACFs of the ionic and heat microfluxes, since they have different physical backgrounds; the cross correlation function (CCF) was defined, after several mathematical attempts, as:

$$\langle J_{\mathrm{O^{2-}}}(0) J_{\mathrm{q}}(t) \rangle = \frac{1}{2} \Big[\langle J_{\mathrm{O+q}}(0) J_{\mathrm{O+q}}(t) \rangle - \langle J_{\mathrm{O^{2-}}}(0) J_{\mathrm{O^{2-}}}(t) \rangle - \langle J_{\mathrm{q}}(0) J_{\mathrm{q}}(t) \rangle \Big], \tag{4.17}$$

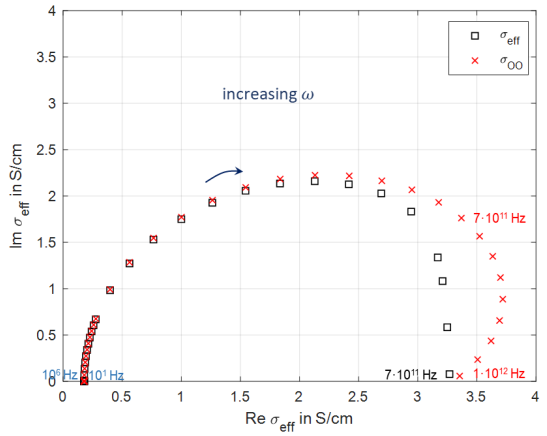

Figure 4.10: Complex effective conductivity σ_{eff} and ionic conductivity σ_{OO} dependency on frequency, originally published on *Solid State Ionics* [65]

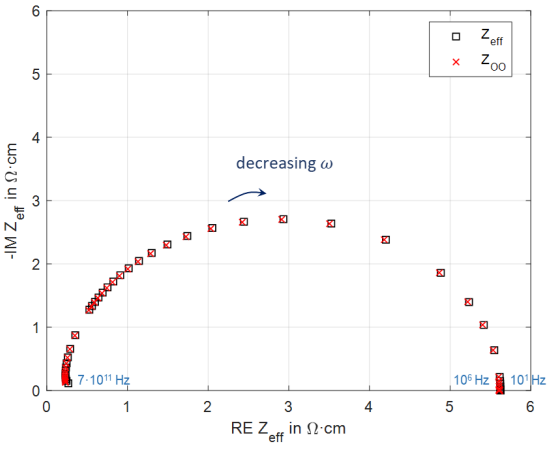

Figure 4.11: Complex effective impedance Z_{eff} and ionic impedance Z_{OO} dependency on frequency, originally published on *Solid State Ionics* [65]

so that the conductivity L_{Oq} can now be calculated:

$$L_{\text{Oq}}(\omega) = \frac{V}{3k_{\text{B}}} \int_0^\infty \langle J_{\text{O}^{2-}}(0) J_{\text{q}}(t) \rangle \text{e}^{i\omega t} \text{d}t, \tag{4.18}$$

which shows a very unsual behaviour, as seen in Fig. 4.8; showing at least four arcs/semicircles and reaching further on behalf of frequencies than the other conductivities, up to $7 \cdot 10^{12}$ Hz. Its real part is negative, opposite to both the ionic and heat flux, thus diminishing both the mass transport $J_{\text{O}^{2-}}$ and the thermal energy transport J_{q}. Nevertheless, when σ_{eff} is calculated, only the frequency range common to the three conductivities is considered, so that only the portion of L_{Oq} depicted in Fig. 4.9 matters. The odd curve observed might be a result of obtaining the transport coefficient at the expense of an artificial CCF, thus increasing the final uncertainty due to statistical propagation.

The effective conductivity $\sigma_{\text{eff}}(\omega)$ from Eq. 4.10 is depicted in Fig. 4.10 and compared to σ_{OO}, the pure ionic conductivity dependends only on L_{OO}, ie. obtained from Eq. 4.10 neglecting the effect of the other transport coefficients results in:

$$\sigma_{\text{OO}} = |L_{\text{OO}}| \text{e}^{i\phi_{\text{OO}}} \frac{(zF)^2}{T}, \tag{4.19}$$

showing that neglecting the other transport coefficients does have an influence, mostly at high frequencies. This effect is nevertheless small when the complex impedance is studied, as

observed in Fig. 4.11, which is calculated as the inverse of the complex conductivity:

$$\tilde{Z}_{\text{eff}} = \frac{1}{\tilde{\sigma}_{\text{eff}}}, \tag{4.20}$$

where both effective and pure ionic impedance Z_{eff}, Z_{OO} show a similar frequency dependency, unlike the conductivity.
This section presented a relationship between the transport coefficients in solid oxide electrolytes and the frequency dependent impedance. It has been shown that the complex impedance curves, as known from EIS as Nyquist plots, can be artificially obtained from the conductivities L_{ij} defined by NET. If the frequency dependent impedance $Z(\omega)$ can be determined from the transport coefficients L_{ij} it should be possible to obtain these conductivities from the impedance curve. This hypothesis is the heart of this doctoral thesis and will be validated and revised in Sec. 6.1.

4.2 Modeling the polymer electrolyte

There is a vast literature on nafion membranes based on experiments, such as the ones developed by Los Alamos laboratory and reproduced here in Sec. 3.2.1. From those empirical relationships many models were developed, although the water content postulates were proven to be not entirely correct [60] , [57].
Since the widespread measurement model approach has shown its limitation, much more can be won from the process model approach, consisting in solving the governing equations of the electrochemical system [84] rather than fitting parameters to a pre-established equivalent circuit.
As previously mentioned in Sec. 3.2.1, the ionic conductivity of Nafion membranes depends to a great extend on the water content, putting emphasis to a non-equilibrium approach and adding a third thermodynamic flux when compared to solid oxide electrolytes. The complexity of water transport can be limited by carrying on experiments with two hydrogen electrodes, so that no water is produced at the cathode.

4.2.1 EIS applied to Nafion membranes

A typical PEM fuel cell, ie. consisting of a nafion membrane as an electrolyte, a fuel electrode supplied with hydrogen and a air electrode supplied either with air or oxygen can be modeled under open circuit (OC) conditions using the equivalent circuit of Fig. 4.12. (The electrodes consist moreover of a conductive current collector or bipolar-plate (BPP), a gas diffusion layer

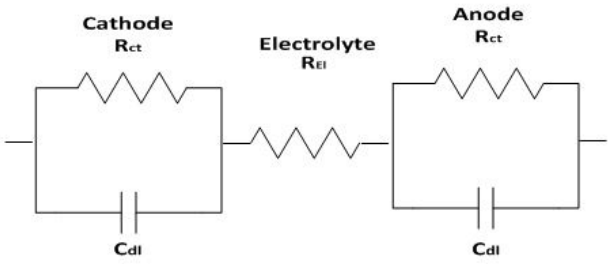

Figure 4.12: Equivalent circuit for a complete PEM fuel cell with H_2/O_2 electrodes at OC

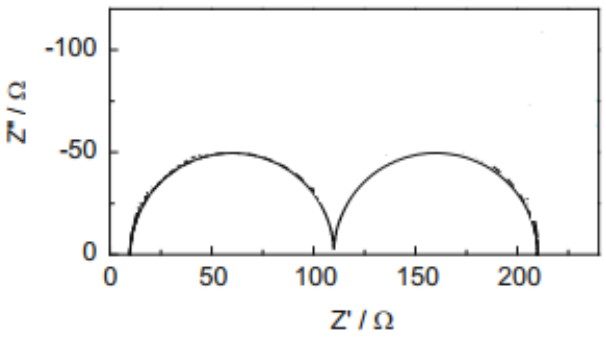

Figure 4.13: Impedance complex representation of the electric circuit from Fig. 4.12 given by Lasia. [85].

(GDL) and a suitable catalyst layer (CL)). The resistor R_{El} represents the ohmic resistance of the electrolyte, while the elements $R_{\mathrm{ct}}//C_{\mathrm{dl}}$ do so for the electrodes, as already explained in Sec. 2.8.1. If this electric circuit is investigated by means of EIS, a Nyquist plot similar to the one depicted in Fig. 4.13 should be obtained. Both electrodes should have relaxation times three orders of magnitude apart from each other in order to obtain good results, as it has been pointed out by MacDonald [17]. This condition has been experimentally confirmed, though seldom [85], [23].

Since the cathode losses at the cathode are much larger than the anode losses, a more appropiate equivalent circuit must be proposed for the test cell of nafion membrane with two hydrogen electrodes. Rezaei Niya and Hoorfar [86] based their process model on the empirical relationships derived from Springer et al [12] to determine the impedance of the hydrogen electrode, while Kjelstrup, Pugazhendi and Bedeux [87] made use of NET to determine the impedance of the hydrogen electrode. Both arrive to the same equivalent circuit, as depicted in Fig. 4.15. Previously, Rezaei Niya and Hoorfar [84] had also developed a process model for the nafion membrane N117, together with the interface nafion membrane/electrode, taking into consideration the water transport resistance in both membrane and electrode, resulting in an equivalent circuit reproduced in Fig. 4.14.

This membrane-interface equivalent circuit can be split in three parts, according to Rezaei Niya. The first resistance R_0 represents the pure ohmic resistance of the membrane at high frequencies, also known as high frequency resistance (HFR), the parallel circuit of $R_1//C$ is considered as the water transport in the membrane, while the circuit $R_1//(R_2 - L)$ shall represent the water transport in the diffusion medium (GDL), part of the electrode.

This model was validated with experimental data for both H_2/O_2 and H_2/H_2 electrodes. The water transport in the membrane and in the GDL was experimentally observed in

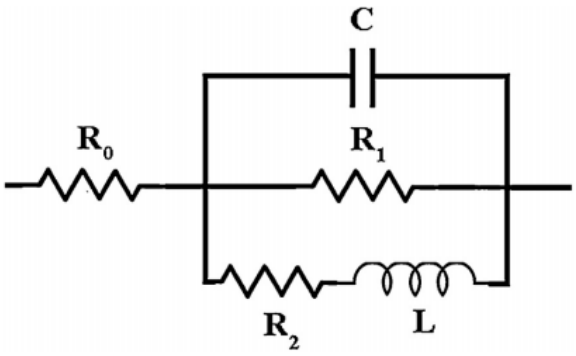

Figure 4.14: Equivalent circuit proposed by Rezaei Niya et al [84] to model the electrode/electrolyte impedance

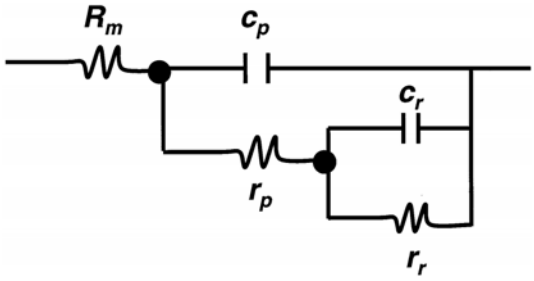

Figure 4.15: Equivalent circuit proposed independently by Kjelstrup et al. [87] and Rezaei Niya et al. [86] to model the electrode impedance.

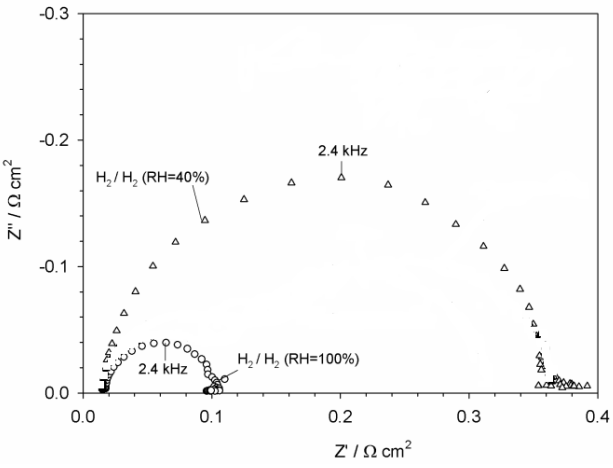

Figure 4.16: Nyquist plot of a PEM cell with a nafion electrolyte and two hydrogen electrodes at different humidification rates given by Malevich, Halliop et al. [88].

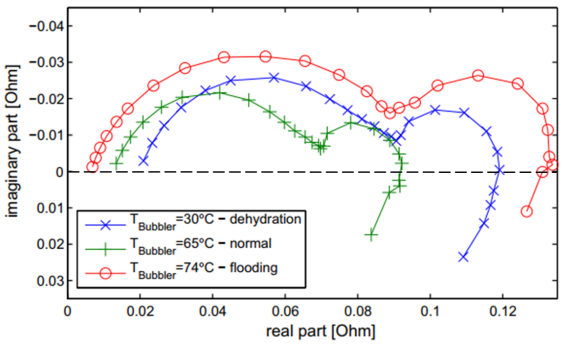

Figure 4.17: Nyquist plot of a PEM cell with a nafion electrolyte and H_2/air electrodes at different humidification rates given by Kadyk, Hanke-Rauschenbach et al. [89].

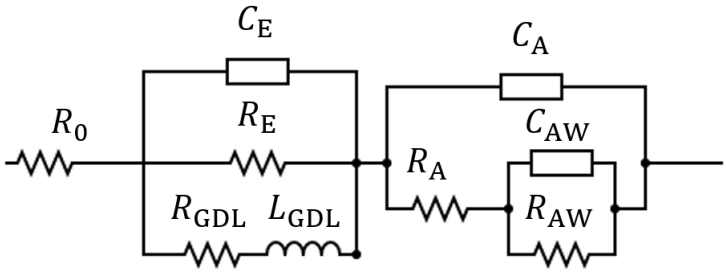

Figure 4.18: Proposed equivalent circuit for the PEM cell with two hydrogen electrodes

EIS measurements by Malevich, Halliop et al [88] (see Fig. 4.16) as well as by Kadyk, Hanke-Rauschenbach et al [89] (depicted in Fig. 4.17). Both studies consider that the water transport can be seen at low frequencies ($f < 1\,\mathrm{Hz}$), an expected fact taking into consideration that chemical diffusion in solids is a slow process when compared to electronic conduction.
All these experiments and models are isothermal, i.e. temperature is considered to be constant, so that the effect of a temperature gradient given by the cross conductivity $L_{\phi q}$ is neglected. For the approach proposed in this thesis, which is based on the experiments shown above, the temperature gradient is considered to contribute to all the processes relevant within the electrolyte (electrolyte itself, water transport through the membrane and interface electrolyte/electrode), so that the experimental work to be carried out shall be modeled by means of an equivalent circuit similar to the one depicted in Fig. 4.18. The basic idea of this proposal shall be explained below.
In the proposed equivalent circuit, the first and second element represent the electrolyte (and a part of the electrode), given by the resistance R_0. This refers to the HFR, ie. the ohmic resistance to the proton motion for a given temperature and water chemical potential; the circuit $R_E//C_E$ represents the water transport impedance in the electrolyte, while the circuit $R_E//(R_{GDL} - L_{GDL})$ accounts for the water transport impedance in the gas diffusion medium. The third element represents the electrode, so that the element $R_{AW}//C_{AW}$ refers to the chemical reaction impedance, while the element $R_A//C_A$ represents the surface polarisation.
Based on the proposed equivalent circuit shown in Fig. 4.18, the expected Nyquist plot should consists of an abscissa intercept followed by two semicircles/arcs. The intercept shall deliver R_0, the first semicircle or middle frequency (MF) should determine the coefficients C_E, R_E, R_{GDL} and C_{GDL}; to separate the contribution from water transport in the electrode, different gas diffusion media should be implemented. The second semicircle or low frequency (LF) return the electrodes' parameters, C_A, R_A, R_{AW} and C_{AW}. The determination of the

conductivities L_{ij} from these electrical passive elements is adressed in the following section. This all depends on the differences in the relaxation time.

4.2.2 NET applied to Nafion membranes

This section is partially based on the modeling presented in previous works by Siemer et al. [90] and Marquardt et al. [15].
Similar to solid oxides, Nafion membranes have a negligible electronic conductivity, so that the external current is proportional to the protonic current through the electrolyte $J_{\mathrm{H_2}} = j/2F$, thus mass and charge transport fluxes are proportional to each other.
With this assumption considered, the following thermodynamic fluxes depicted in Fig. 4.19 resulting from the Non-Equilibrium approach for the polymer electrolyte result:

$$J_{\mathrm{q}}^{'} = -L_{\mathrm{qq}}\frac{1}{T^2}\frac{\mathrm{d}T}{\mathrm{d}y} - L_{\mathrm{q}\mu}\frac{1}{T}\frac{\mathrm{d}\mu_{\mathrm{H_2O}}}{\mathrm{d}y} - L_{\mathrm{q}\phi}\frac{1}{T}\frac{\mathrm{d}\phi}{\mathrm{d}y}, \tag{4.21}$$

$$J_{\mathrm{H_2O}} = -L_{\mu\mathrm{q}}\frac{1}{T^2}\frac{\mathrm{d}T}{\mathrm{d}y} - L_{\mu\mu}\frac{1}{T}\frac{\mathrm{d}\mu_{\mathrm{H_2O}}}{\mathrm{d}y} - L_{\mu\phi}\frac{F}{T}\frac{\mathrm{d}\phi}{\mathrm{d}y}, \tag{4.22}$$

$$j = -L_{\phi\mathrm{q}}\frac{1}{T^2}\frac{\mathrm{d}T}{\mathrm{d}y} - L_{\phi\mu}\frac{1}{T}\frac{\mathrm{d}\mu_{\mathrm{H_2O}}}{\mathrm{d}y} - L_{\phi\phi}\frac{1}{T}\frac{\mathrm{d}\phi}{\mathrm{d}y}. \tag{4.23}$$

Similar to solid oxides, the conductivities L_{ij} shall be considered to be bulk properties, small perturbations ought to be applied, so that $\mathrm{d}\varkappa \approx \Delta\varkappa$ is a valid assumption, which leads to $\mathrm{d}y \approx d^{\mathrm{E}}$. The NET equations now read:

$$J_{\mathrm{q}}^{'} = -L_{\mathrm{qq}}\frac{1}{T^2}\frac{\Delta T}{d^{\mathrm{E}}} - L_{\mathrm{q}\mu}\frac{1}{T}\frac{\Delta\mu_{\mathrm{H_2O}}}{d^{\mathrm{E}}} - L_{\mathrm{q}\phi}\frac{1}{T}\frac{\Delta\phi}{d^{\mathrm{E}}}, \tag{4.24}$$

$$J_{\mathrm{H_2O}} = -L_{\mu\mathrm{q}}\frac{1}{T^2}\frac{\Delta T}{d^{\mathrm{E}}} - L_{\mu\mu}\frac{1}{T}\frac{\Delta\mu_{\mathrm{H_2O}}}{d^{\mathrm{E}}} - L_{\mu\phi}\frac{F}{T}\frac{\Delta\phi}{d^{\mathrm{E}}}, \tag{4.25}$$

$$j = -L_{\phi\mathrm{q}}\frac{1}{T^2}\frac{\Delta T}{d^{\mathrm{E}}} - L_{\phi\mu}\frac{1}{T}\frac{\Delta\mu_{\mathrm{H_2O}}}{d^{\mathrm{E}}} - L_{\phi\phi}\frac{1}{T}\frac{\Delta\phi}{d^{\mathrm{E}}}. \tag{4.26}$$

The third equation allows the direct characterisation by means of EIS, since both the potential $\Delta\phi$ and a current j are known.

However, when comparing Eq. 4.26 to the equivalent circuit presented in Fig. 4.18, it can be observed that there are too many electric elements to be estimated. It has to be kept in mind that this equivalent circuit is a proposal. It is not known if it successfully reproduces the electrochemical system. Moreover, the literature does so far not consider any temperature gradients ΔT, at least not simultaneously with a gradient in water chemical potential $\Delta\mu_{\mathrm{H_2O}}$.

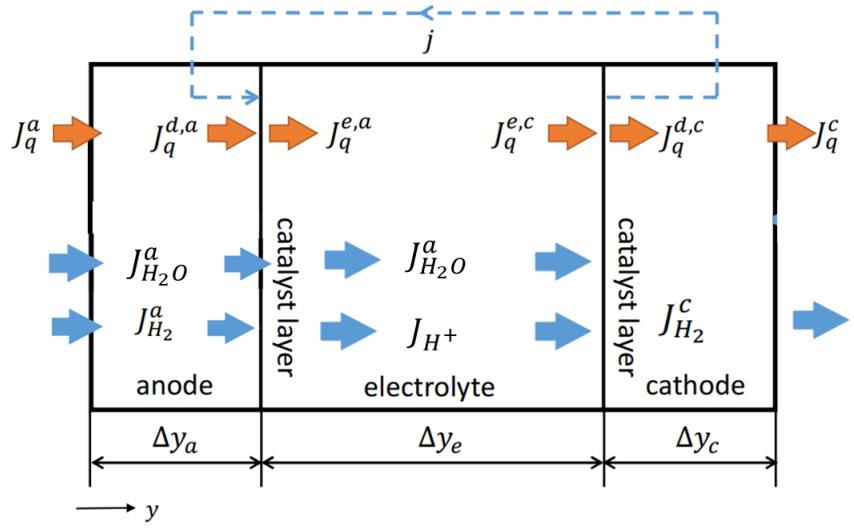

Figure 4.19: Scheme of the fluxes through a polymer electrolyte with two hydrogen electrodes

The equivalent circuit also shows, that the water transport in the membrane cannot be separated from the water transport in the gas diffusion layer, introducing new unknowns to the problem, ie. the transport coefficients $L_{ij}^{a,c}$ of the electrodes' GDL. The problem becomes more complicated when the LF elements, corresponding to the electrodes/catalyst layers are not well delimited, so that the MF and LF arcs have similar relaxation times, as observed by Kjelstrup, Pugazhendi et al. [87]

It becomes clear that a characterisation of the polymer electrolyte standing alone based on EIS, in terms of NET coefficients L_{ij} as already proposed for the solid oxide electrolyte, is not possible. It becomes extremely important to reduce the contribution of both the GDL and the CL to the impedance curve before trying to approximate them by passive elements of the proposed equivalent circuit, since these elements are partially dependent on the transport coefficients of the other fuel cell components, as shown by Rezaei Niya [84], [91] in several occasions.

Nevertheless, a more pragmatic approach allows a first approximation of the electrolyte conductivities, as elaborated in the following subsections.

4.2.2.1 Determination of $L_{\phi\phi}$

When at both sides of the membrane the temperature is the same, in a first approximation no temperature gradient $\Delta T = 0$ is assumed. The electrolyte could still show a temperature profile due to dissipation. In a similar manner, when the chemical potential of water is

the same at both sides, no gradient in the chemical potential is assumed, to hold true approximately for the membrane $\Delta\mu_{H_2O} = 0$, and the electric current j is only driven by the electric potential $U = \Delta\phi$:

$$j = -\frac{L_{\phi\phi}}{T}\frac{\Delta\phi}{d^M} \tag{4.27}$$

The applied signal X in EIS contains two parts, $\bar{X}$ is frequency independent (as in direct current) and $\tilde{X}$ is frequency dependent (as in alternate current), $X = \bar{X} + \tilde{X}$, being X either current or voltage (galvanostatic or potentiostatic). Considering that in the general case of galvanostatic EIS a periodic current $I = \bar{I} + \tilde{I}$ is applied, the test cell reacts by giving a periodic voltage answer $U = \bar{U} + \tilde{U}$:

$$\frac{1}{A}(\bar{I} + \tilde{I}) = -\frac{L_{\phi\phi}}{T}(\bar{U} + \tilde{U})\frac{1}{d} \tag{4.28}$$

In case of OC, $\bar{I} = 0$ and the OCV is also zero, since no voltage results from symmetrical hydrogen electrodes, ($\bar{U} = 0$) so that:

$$\frac{\tilde{U}}{\tilde{I}} = \tilde{Z}_{\omega\to\infty} = -\frac{d}{A}\cdot\frac{T}{L_{\phi\phi}}. \tag{4.29}$$

Thus the conductivity $L_{\phi\phi}$ can be determined from the high frequency intercept with the abscissa (high frequency resistance HFR) of the impedance curve, since the conductivity is a real value. In that case, a relationship between L_{OO} and the resistance R_0 from the equivalent circuit, Fig. 4.18 can be found:

$$\tilde{Z}_{\omega\to\infty} = R_0 = -\frac{d}{A}\cdot\frac{T}{L_{\phi\phi}} \tag{4.30}$$

A graphical description is given in Fig. 4.20.

Thereafter two separate cases shall be considered experimentally: the variation of temperature while the water chemical potential in the membrane is kept constant and secondly the variation of the water chemical potential while the membrane temperature is kept constant.

4.2.2.2 Determination of $L_{\phi\mu}$

Shall the temperature of the electrolyte be constant, the temperature gradient again is absent, $\Delta T = 0$ and Eq. 4.26 results in:

$$j = -L_{\phi\mu}\frac{1}{T}\frac{\Delta\mu_{H_2O}}{d^E} - L_{\phi\phi}\frac{1}{T}\frac{\Delta\phi}{d^E}. \tag{4.31}$$

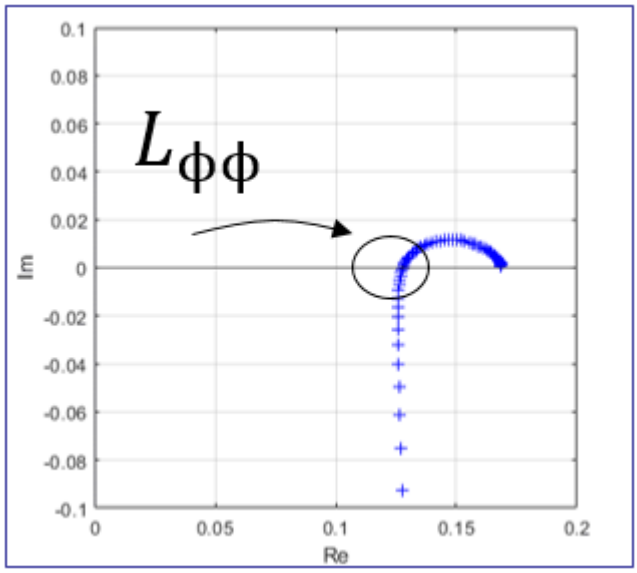

Figure 4.20: From the high frequency intercept with the abscissa it is possible to determine the conductivity $L_{\phi\phi}$

If the electric circuit of the test cell is kept open while increasing the gradient of the water chemical potential across the electrolyte, the OCV increases proportionally:

$$0 = -L_{\phi\mu}\Delta\mu_{\mathrm{H_2O}} - L_{\phi\phi}\Delta\phi. \tag{4.32}$$

Solving for the conductivity gives:

$$L_{\phi\mu} = -L_{\phi\phi}\frac{\Delta\phi}{\Delta\mu_{\mathrm{H_2O}}}, \tag{4.33}$$

making possible to approximate the conductivity $L_{\phi\mu}$ from the slope of the $U_{\mathrm{OC}} - \Delta\mu$ curve. This approximation considers the potential loss at the electrodes to be negligible.

4.2.2.3 Determination of $L_{\phi\mathbf{q}}$

On the other hand, if the water chemical potential is kept constant at both sides of the polymer membrane, i.e. $\Delta\mu = 0$ and the test cell is open, Eq. 4.26 results in:

$$0 = -L_{\phi\mathrm{q}}\frac{1}{T^2}\frac{\Delta T}{d^{\mathrm{E}}} - L_{\phi\phi}\frac{1}{T}\frac{\Delta\phi}{d^{\mathrm{E}}}, \tag{4.34}$$

so that the conductivity $L_{\phi q}$ can be obtained proportional to the slope of the $U_{OC} - \Delta T$ when the electrolyte is exposed to a temperature gradient ΔT:

$$L_{\phi q} = -L_{\phi\phi} \cdot T \frac{\Delta\phi}{\Delta T} \tag{4.35}$$

Although in both electrolyte types transport coefficients of similar meaning shall be modelled and determined by the same technique, i.e. electrochemical impedance spectroscopy, the methods to obtain them differ notoriously. The conductivities of the solid oxide electrolyte should be determined more directly, as the charge is only couple to a heat transport. This approach cannot be transferred to the polymer electrolyte, since water vapour is also transported through. The extra flux adds up to six conductivities. The task becomes impractical to solve if proper assumptions are not taken. These assumptions weres presented in the previous sections (see Sec. 4.2.2.2-4.2.2.3).

Chapter 5

Materials and Methods

The experiments presented in this chapter were carried out at the facilities of the Institute of Thermodynamics, Leibniz University Hannover, mostly at the fuel cell laboratory. The laboratory offers a high temperature test bench (FuelCon GmbH) depicted in Fig. 5.1 and test bench for a PEM stack of 16 cells with a single temperature conditioning system, which is located inside a laboratory extractor. The facilities also offer another extractor to place a PEM single cell test bench, which is to be designed and assembled. The test bench is presented in Fig 5.2. More about its design can be found in the following sections.

5.1 The high temperature test bench for solid oxide electrolytes

The test bench used for the characterization of the 3YSZ electrolyte is an Evaluator C1000-HT from FuelCon GmbH, which allows a fully automated operation at high temperatures. It consists of an insulated furnace with a testing device inside, as shown in Fig. 5.3. The testing device is composed of a versatile housing, called TrueXessory-HT ®, to test cells, stacks and electrolytes. The testing device is depicted in Fig. 5.4.

The alumina housing consists of two casings, the top casing (TC) and the bottom casing (BC). In between there is a ceramic sealing for the test object. The TC has two boreholes, one at the top to place the ceramic bar that supports the current bar and a small one at the front to measure the voltage. In the inside it is hollow to place the nickel block that acts as a fuel flow field and a current collector (which is connected to the current bar). The fuel side flow field consists of milled parallel channels (width 1.5 mm., height 1.5 mm.). To enlarge the contact area, a nickel mesh is included between nickel block and electrode. The BC has

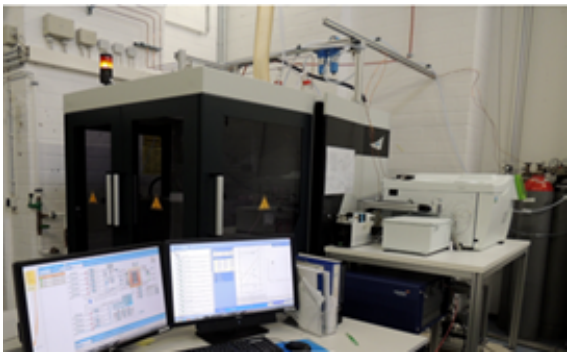

Figure 5.1: High temperature test bench Evaluator C1000-HT from Fuel-Con GmbH.

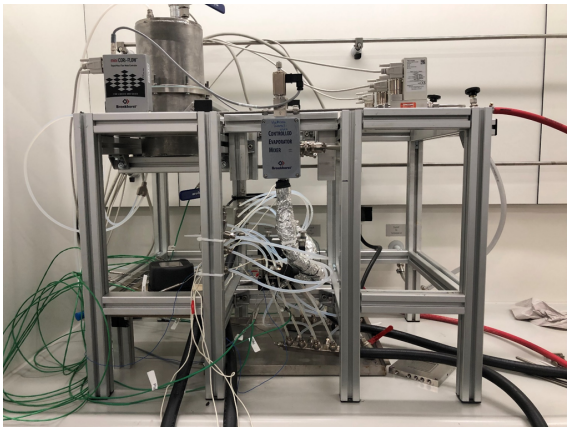

Figure 5.2: PEM single cell test bench. Design and assembly by the Institute of Thermodynamics, Leibniz University Hannover.

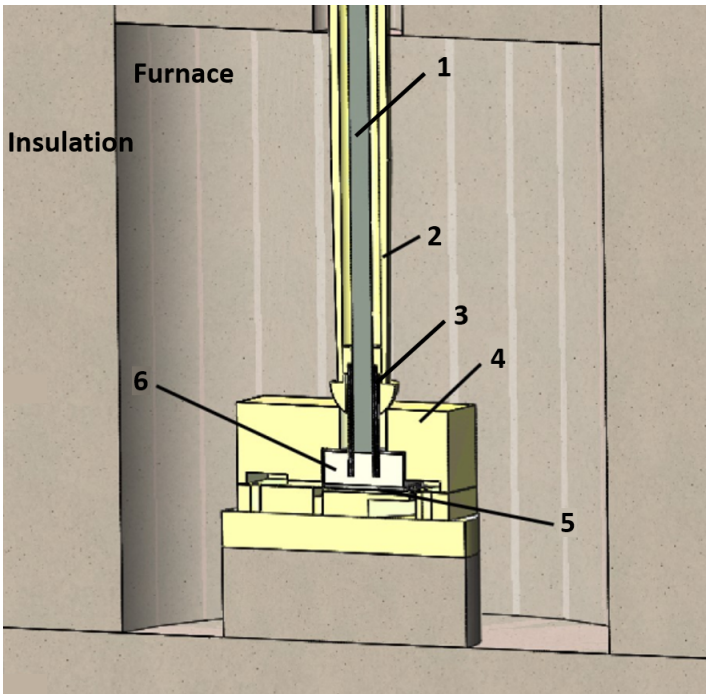

Figure 5.3: CAD cross section of the test bench furnace: 1) current bar, 2) ceramic housing of the current bar, 3) external heater, 4) cell housing, 5) test cell and 6)nickel block

four boreholes on its bottom, that account for the fuel and air streams, each of them having an inlet and an outlet. The BC is in the centre milled to form a flow field for the air side, with similar sizes as at the fuel side. Above the flow field a platinum mesh is placed. This mesh has two terminals, one to connect the current circuit and one to measure the voltage. Between TC and BC there is room for a sealing gasket, which was designed for cells but cannot be used for electrolyte experiments due to the differences in thickness. Lastly, the test cells are placed between TC and BC.

The test rig allows the incorporation of an extra heater in the ceramic bar around the current bar. This electric heater, shown in Fig. 5.4, lies on a circular groove present in the nickel block. The extra heat flux flows from the heater to the nickel block and thereafter to the cell/electrolyte.

A natural temperature gradient through the test objects (cells and/or electrolytes) has been observed, even though the external heater was switched off. It is suspected to be a consequence of design, as the oven insulation is thinner at the bottom of the oven compared to its walls and at its top. Several attempts were made to improve the insulation, resulting in a decrease of the gradient and a decrease in the electrical power of the oven for a given temperature. However, it was not possible to get completely rid of it. Since no temperature gradient is allowed to corroborate the absence of electric potential (given that the chemical potential is also the same at both electrodes), it becomes necessary to counteract this "natural" temperature gradient. Therefore another external heater was placed at the air side. It consisted of a heating wire (Block RD100/0, 2. $R = 15.6\,\Omega/\mathrm{m}$) insulated with a fiber glass hose (Techflex GmbH, $\phi = 0.3\,\mathrm{mm}$.). This wire heater was placed on the channels of the air side flow field and powered by a generic power supply unit. It has proven to be effective to compensate the natural temperature gradient, so that finally no temperature difference across the electrolyte was present. Depending on the set temperature, the necessary power to fully compensate the temperature gradient was $1 - 20\,\mathrm{W}$.

In the original configuration temperatures were measured with thermocouples type N class 1 (Omega Engineering GmbH) in two positions: at the nickel block (above the upper electrode, T1) and at the bottom part of the housing (below the down electrode, T2). That is why the measurement equipment of the test bench must be modified to better measure and control the experimental conditions around the electrolyte. The first modification consisted in changing the position from T1 to T3 to measure the electrolyte temperature at the top, since placing a thermocouple at T1 is extremely difficult, as it has to go through a tight borehole in the heater. Several thermocouples broke while attempting to place it. Moreover, it is not possible to check if the measuring end of the thermocouple is in contact with the nickel block or if it

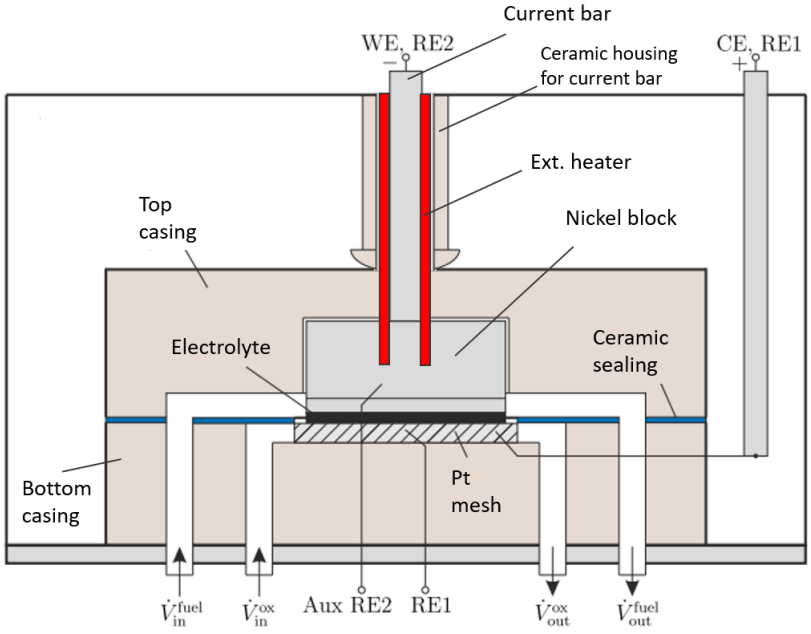

Figure 5.4: Housing (TrueXessory-HT) for the characterization of electrolytes in the high temperature test bench Evaluator C1000-HT. Modified from Hollmann [31].

floats somewhere else, measuring the hollow air temperature, hence underestimating the real temperature. T3 is, on the contrary, easily accesible from the side, making posible to check the contact between thermocouple end and nickel block.

It is extremely important to measure the temperature difference at both sides of the electrolyte. Since thermocouples have large error tolerances at high temperatures, measuring the temperature difference with two independent thermocouples would lead to an error in the difference of at least twice the tolerances, reaching in some cases $\delta\Delta T = 15\,\text{K}$. Considering that the test rig can apply a temperature gradient of, at the highest, $\Delta T = 20\,\text{K}$ it is important to reduce the instrument tolerance, which could represent more than 100% of the measured value (e.g. considering each thermocouple type N class 2 has a tolerance of at least 2.5 K, the temperature difference would present a tolerance of at least 5 K, which would lead to an experimental error of 100% when measuring a temperature difference of 5 K). To overcome this difficulty, a differential thermocouple $\text{diff}\,T = \text{diff}\,T_{\text{top}} - \text{diff}\,T_{\text{bottom}}$ was built by bridging two thermocouples as shown in Fig. 5.5.

The main disadvantage of this approach is the lack of an absolute temperature at the electrolyte sides. That is why T3 was used as an absolute temperature measurement, as it measures one of the electrolyte surfaces, parallel to the differential temperature $\text{diff}\,T_{\text{t}}$. Fig. 5.6 shows the positioning of the mentioned thermocouples.

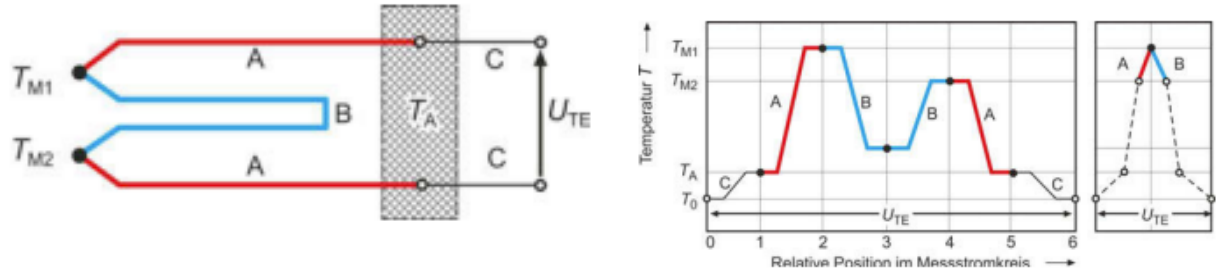

(a) Two thermocouples connected to each other to measure temperature difference

(b) Analysis of the measure circuit

Figure 5.5: Concept of a temperature difference measure with two thermocouples short-circuited on one pole, given by [92].

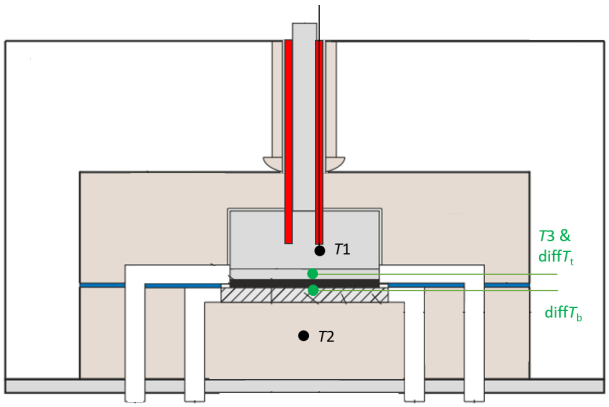

Figure 5.6: Positioning of thermocouples in the housing of the high temperature test bench. Modified from Hollmann [31].

5.1.1 The solid oxide test cell

The cells were obtained by brushing platinum paste (71% Pt, ChemPur GmbH) on thick 3YSZ blocks (Zell Quarzglas GmbH). The size of the blocks was $(40 \cdot 40)$ mm. in two different thicknesses, 5 and 10 mm.. The platinum electrodes were calcined in the FuelCon test rig at 1270 K during 5 hours at a heating rate of 2 K/min, following the procedure given by Toghan et al. [93].

5.1.2 The solid oxide electrolyte experiments

Once the bottom thermocouples ($T2$, diff T_b) and the wire heater were placed, the platinum mesh was laid on the BC, followed by the holder frame and the test cell. After that the fuel side platinum mesh and the nickel block were put on the test cell, followed by the top thermocouples ($T3$, diff T_t) and finally the TC. Afterwards the ceramic bar containing the current bar is placed on the TC, its terminals (power source for the heater, wires, connectors

for the EIS) are connected and finally the oven is closed.
The measurement series consists of a variation of temperature and temperature difference across the electrolyte. Three temperatures were examined, $T = 373, 500, 600\,\mathrm{K}$ as well as three temperature differences $\Delta T = 0, 10, 20\,\mathrm{K}$. The temperature difference limitation of $\Delta^E T = 20\,\mathrm{K}$ is given by the test bench, when reaching this maximum an alarm is triggered and the power supply is turned out. Since it is a safety issue, this feature cannot by switched off.
The set of experiments started by setting the desired temperature.Due to the heating rate of $1\,\mathrm{K/min}$ it takes several hours to reach a steady state inside the housing. Once the steady state is achieved, the gas mass flows rates are set at the mass flow control meters. In order to check if there is a dependency on the gas stream, the gas mass flows were varied in the range $0.2 - 1\,\mathrm{Nl/min}$ as well as different gases were supplied, such as oxygen, nitrogen and compressed air.
Secondly, the compensation wire heater is turned on and the supplied power is adjusted until the temperature difference thermocouple showed $0 \pm 2.6\mu\mathrm{V}$, which is approximately $0 \pm 0.1\mathrm{K}$. After that, the open circuit voltage (OCV) was measured during five minutes. Thereafter electrochemical impedance spectroscopy (EIS) was taken, also in open circuit conditions. The measurement was galvanostatic with an amplitude of $0.5 - 3\,\mu\mathrm{A}$ (depending on the resulting impedance) in the frequency range $10^6 - 1\,\mathrm{Hz}$, taking care that the voltage response do not exceed 20 mV. Both measurements were carried out with a device ModuLab (Ametek GmbH) containing a Potentiostat 1 MS/s (PSTAT) and a Frequent Response Analyzer (FRA) 10 µHz - 1 MHz. After that, the external heater was turned on and the electric power was slowly increased until it reached steady state, which took several hours. The open circuit measurement followed by EIS was repeated and the next desired temperature difference was set by increasing the power supplied to the external heater and checking steady state with the differential thermocouple. This procedure was repeated until all the desired measurements were carried out.
It was observed that, at high temperatures, the thick electrolyte ($d^E = 10\,\mathrm{mm}$) does not reach the temperature difference of 20 K when the maximum heating power is supplied.

5.2 The low temperature test bench for polymer electrolytes

As mentioned before, this low temperature test bench had to be designed and assembled before the measurement series could be started, that is why the experimental data is not as

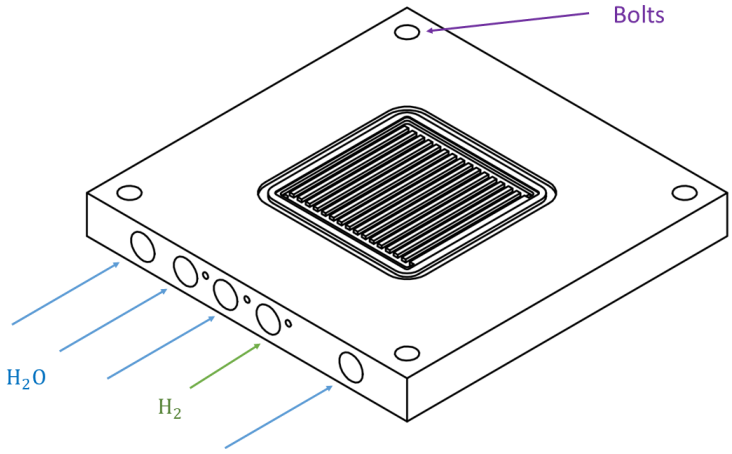

Figure 5.7: Mono-polar plates employed in the low temperature test bench. Original from Marquardt et al. [16].

extensive as the high temperature ones.

The bipolar plates were already available, in this case they ought to be named monopolar plates, since only one surface is milled to obtain the flow field. They consist of stainless steel plates (DIN 1013 - 1.4541), as seen in Fig. 5.7. They have four boreholes through their width to adjust their temperature with a thermal working fluid. The fifth borehole conducts the gas mixture (hydrogen/water) to the flow field. The contact area ($A^{\mathrm{Cell}} = 25\,\mathrm{cm}^2$) was, as mentioned before, milled on one of their surfaces and the flow fields were milled afterwards in this area, creating a gap between the top of the grooves and the top of the plates to place the GDLs. The channels are rectangular with a width $w = 1.50\,\mathrm{mm}$ and a depth $h = 1.30\,\mathrm{mm}$. In the first concept, the individual layers of the test cell were compressed by means of bolts, nuts and a torque wrench, using the four boreholes in the corners of the plates, see Figs. 5.7 and 5.8. This method proved to be highly inefficient, since the preliminary results were not reproducible: after disassembling and assembling again, the measured impedance scattered unacceptably. It was also observable, that the pressure applied by the corner bolts was not distributed homogeneously over the active surface.

This first concept for cell assembly included an indirect humidification by means of a bubbler, as depicted in Fig. 5.8. The hydrogen gas bubbles from the bottom of a closed tank filled in with distilled water, whose temperature can be adjusted by a thermostat. Determining the relative humidity of the outgoing gas stream was not possible. To circumvent this deficit, it was considered that the gas stream leaving the bubbler is saturated, so that the water partial pressure is determined by the bubbler temperature. Given the height of the bubbler this assumption is plausible. Much effort was dedicated to make this device work, nonetheless for

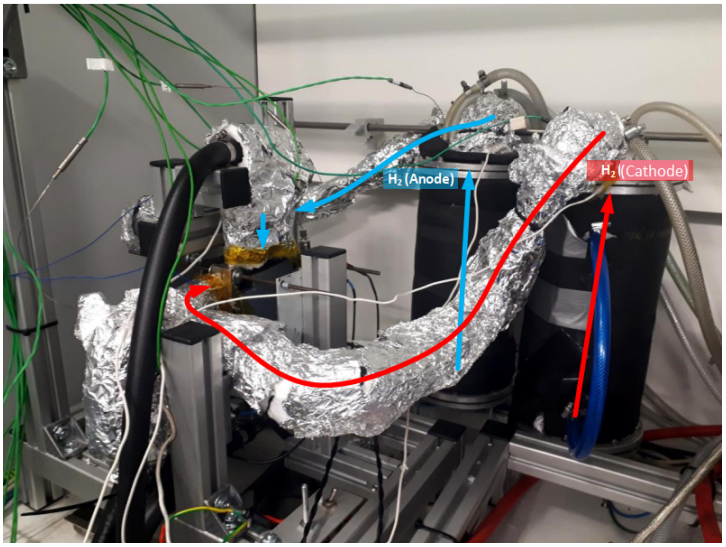

Figure 5.8: First PEM test bench used. Figure by Meyer [94].

several reasons it was not possible to obtain a steady state for longer periods of time. This makes impossible to measure EIS, as these measurements need stable conditions for a long period.

Therefore it was decided to design a more accurate test bench, where the partial pressure of water vapour could be measured or at least more precisely set. A scheme of the resulting test bench is depicted in Fig.5.9. It allows to control the conditions of the electrodes $i = \mathrm{A}, \mathrm{C}$ independently from each other, such as temperature T^i, water mass flow $\dot{m}^i_{\mathrm{H_2O}}$ and hydrogen mass flow $\dot{m}^i_{\mathrm{H_2}}$.

The temperature of the electrodes T^i can be controlled by thermostats within $\pm 0.01\mathrm{K}$. The thermal working fluid flows through four boreholes in the monopolar plates to give an homogeneous temperature along the flow field. To assure this homogeneous temperature at the cell surface area, the plates are sufficiently large and the boreholes are evenly spaced. The plate temperature is measured close to the flow field.

The gas streams are controlled by thermal mass flow controllers (MFC) (Bronkhorst, Model EL-FLOW Prestige, $\dot{V}_{\mathrm{H_2}} = 0.1 - 5\,\mathrm{Nl/min}$). The water flows are controlled by coriolis mass flow controllers (Bronkhorst, Model mini CORI-FLOW, $\dot{m}_{\mathrm{H_2O}} = 10 - 100\,\mathrm{g/h}$). Both streams are mixed and then brought to the desired temperature in evaporators, which consist of mixing chambers followed by heat exchangers (Bronkhorst, Model W-202A CEM). The evaporator temperature controllers were designed and constructed at the institute by Mr. Larki Harchegani. The gases were obtained from gas cylinders (purity 99.999%, Linde AG), and the distilled water came from a purification plant Milli-Q® Elix Advantage UV (Merck Millipore, $\sigma \leq 0.067\,\mu\mathrm{S/cm}$). The distilled water was kept in a pressurized tank, so that

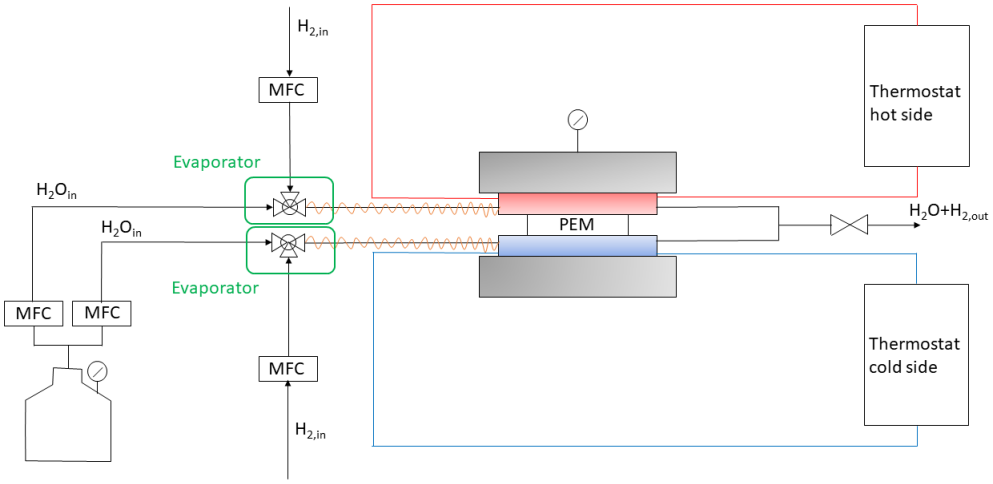

Figure 5.9: Scheme of the test bench for the polymer test cell. Based on a figure by Reißner [95].

both fluids enter the mixing chamber at the same pressure. While the gas pressure was regulated with pressure valves and reducers, the water tank was pressurized with compressed air previously filtered. The pipeline between evaporator and test cell was heated with a heating cord (Horst GmbH, Model HS42, 350 W) powered by a generic power supply unit, to avoid heat losses and condensation. The supplied power ($6 - 30\,\mathrm{W}$) was mostly dependant on the water mass flow, it was adjusted to keep the temperature at the cell inlet $3 - 5\,\mathrm{K}$ above the plate temperature.

All temperatures were measured with thermocouples type K class 2 (TC Direct GmbH) previously calibrated for the temperature range $10 - 110\,°\mathrm{C}$ with a dry block calibrator (Isotech 580 Oceanus-6) where the reference temperature was given by a thermometer PT25 (measure bridge Isotech).

The compression system based on bolts and nuts was replaced by a compression hardware (LeanCat, Model AC-50) depicted in Fig. 5.10. It was operated with compressed air, the contact area between compression hardware and test object is limited to $(90 \cdot 90)\,\mathrm{mm}$. This is important in order to determine the actual pressure applied to the test cell.

The commissioning of the compression hardware showed that the milled surface of the MPP was not perfectly even, since one corner was about $10\,\mu\mathrm{m}$ deeper. That is why the GDL had to be changed in order to assure sealing and proper contact to the membrane. The tests to control the pressing consisted in piling the test cell components between the mono-polar plates, inserting a PRESCALE®pressure film (Fujilm GmbH) in between, varying

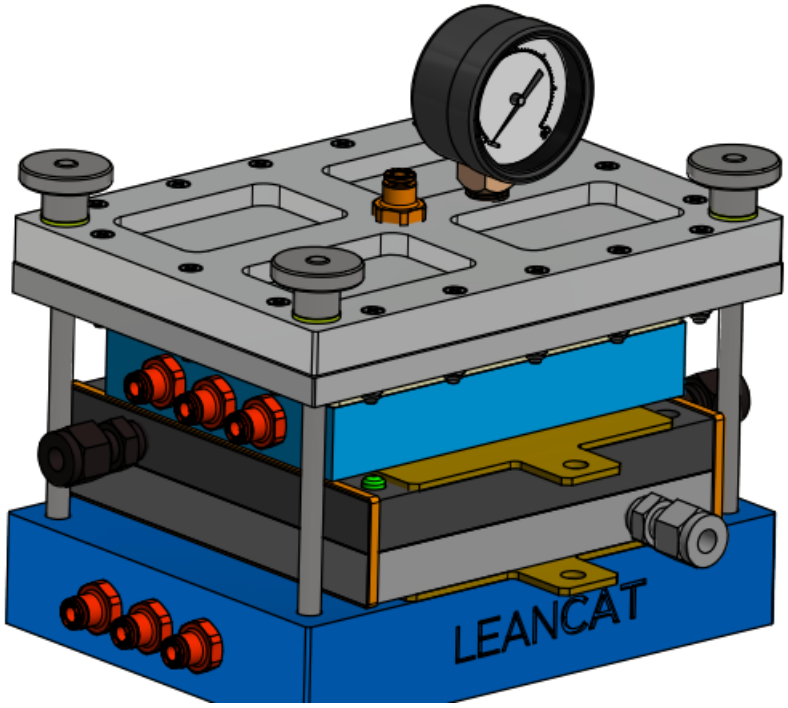

Figure 5.10: Scheme of the compression hardware by Leancat®[96].

their position in the stack.

5.2.1 The polymer test cell

The electrolyte consisted of Nafion® membranes N1110. As one membrane has a thickness of $d^{\mathrm{M}} = 254\,\mu\mathrm{m}$, and due to its fairly good thermal conductivity, it turns out necessary to pile up more than one membrane, so that moderate gradients can be obtained. After a feasibility study it was chosen to form the electrolyte with five membranes. Therefore a total thickness of $d^{\mathrm{M}} = 1.27\,\mathrm{mm}$ is achieved. A series of studies was carried out with squared laboratory cells of $100\,\mathrm{mm}^2$, which were not satisfactory due to edge effects. That is why it was decided to use larger membranes, which had a surface area of $(100 \cdot 100\,\mathrm{mm})$. The membranes facing the plates were coated within a surface area of $(50 \cdot 50\,\mathrm{mm})$ with a platinum catalyst layer, the loading was $0.3\,\mathrm{mg/cm}^2$ (Ion Power GmbH). Both GDLs were selected to fill the gap ($\approx 300\,\mu\mathrm{m}$) between the plate surface and the flow field grooves. Carbon paper treated with PTFE (commercially known as Teflon®) is the widespread material used as GDL, available with a thickness of $150 - 300\,\mu\mathrm{m}$ and a compressibility of $10 - 20\%$ under operating pressures. Given the gap present in the plates at one corner, other options had to be considered, so that it was chosen to use a carbon cloth (CT, Model W1S1011, $d = 410\,\mu\mathrm{m}$) with a thickness of $\approx 350\,\mu\mathrm{m}$ at 1.0 MPa. Carbon cloths offer a better mechanical stability because of their

thickness at the expense of a higher electrical resistance.
The test sealing was achieved by PTFE foils of 50 µm (High-tech-flon GbR). The components were assembled and kept at a constant pressure given by the compression hardware. Due to the ratio piston area to cell area, a pressure of 3 bar applied to the piston results in a cell pressure of:

$$p_{\mathrm{Cell}} = p_{\mathrm{piston}} \cdot \frac{A_{\mathrm{piston}}}{A_{\mathrm{Cell}}} = 3.1\,\mathrm{bar} \cdot \frac{81\,\mathrm{cm}^2}{25\,\mathrm{cm}^2} \approx 10\,\mathrm{bar} \tag{5.1}$$

5.2.2 The polymer electrolyte experiments

The measurement series includes two temperatures, $T = 333$ and 348 K and two membrane relative humidity levels $\mathrm{rH}^{\mathrm{M}} = 60$ and 85%, which corresponds to water contents of $\lambda^{\mathrm{M}} = 4.2$ and 8.4, respectively. Each of these four measuring points shall be exposed to temperature differences of $T = 0, 5, 10, 15$ and 20 K as well as water chemical potential differences of $\mu_{\mathrm{H_2O}} = 0, 180, 360, 540, 720$ and 900 J/mol.
Once the test cell has been assembled and has been positioned in the test bench, it can be powered up. Firstly, the thermostats are set to the desired temperature, the heating cords are turned on and adjusted to deliver enough energy to keep the gas inlet temperature as previously specified. Afterwards, the gas flow is released followed by a gradual release of the water flow. The cell must now be humidified long enough to assure a homogeneous partial water vapour pressure through the membrane assembly, which was achieved after several hours of gas flow at the water saturation pressure. This was carried out during night.
A series of experiments starts in the morning by adjusting the temperatures of the thermostats and adjusting the power of the heating cords. The constant temperature at the plates is reached within half an hour. Meanwhile the water stream is also adjusted. After achieving the desired conditions the system is given at least 45 minutes to reach a steady state. This waiting time is necessary to obtain a homogeneous humidity (and thermal conductivity) of the electrolyte.
The steady state condition is checked up with the open circuit voltage (OCV), which is measured five minutes with a rate of 2 samples per second. After that the electrochemical impedance spectroscopy (EIS) measurements were initiated, in an open circuit condition. The measurement was galvanostatic with an amplitude of $1 - 5$ mA (depending on the resulting impedance) in the frequency range $10^5 - 10^{-1}$ Hz. After that, some minutes were given to the system in order to recover steady state. Finally $U - j$ characteristics were taken. The scanning rate varied in the range $5 - 20$ µA/s, depending on the OCV. A series of three electrical measurements were carried out with the same device described in 5.1.2

Afterwards the next measuring point was set, following the previously mentioned order (thermostat, heating cord, MFCs).
Considering that the chemical potential of water vapour at the reaction layers (i = am, cm) (see Sec. 2.2)

$$\mu_{\mathrm{W}}^{\mathrm{am}}(p, T^{\mathrm{am}}, x_{\mathrm{W}}) = G_{\mathrm{m,W}}(T^{\mathrm{am}}) + RT^{\mathrm{am}} \cdot \ln\left(\frac{p_{\mathrm{W}}^{\mathrm{am}}}{p^{\Theta}}\right), \tag{5.2}$$

$$\mu_{\mathrm{w}}^{\mathrm{cm}}(p, T^{\mathrm{cm}}, x_{\mathrm{W}}) = G_{\mathrm{m,W}}(T^{\mathrm{cm}}) + RT^{\mathrm{cm}} \cdot \ln\left(\frac{p_{\mathrm{W}}^{\mathrm{cm}}}{p^{\Theta}}\right), \tag{5.3}$$

is dependent not only on the water partial pressure at the reaction layer $p_{\mathrm{W}}^{i}/p_{\mathrm{W}}^{S}$ (indirectly given by the set point of the water coriolis mass flow controller) but also on its temperature T^{i}, it turns out necessary to calculate the temperature, which is extremely difficult. From a macroscopic point of view it is difficult to place a thermocouple between the reaction layer without disturbing the electrochemical mechanisms severely. Thus it was decided to calculate T^{i} based on the plates temperatures T^{i} (i = A, C). Given that every layer (plates, GDL, membrane) has a bulk thermal conductivity independent on the position ($k_{\mathrm{i}} = f(T) \neq f(y)$), the temperature profile across the test cell will develop as presented in Fig. 5.11. The electrolyte's thermal conductivity k_{M}, dependent on the water content λ_{W}, as expressed by Khandelwal et al. [97] is given by Eq. 5.4:

$$k_{\mathrm{Naf}} = \frac{\frac{\lambda_{\mathrm{W}}}{\rho_{\mathrm{W}}} \cdot k_{\mathrm{W}} + \frac{1}{c_{\mathrm{SO3-}} \cdot M_{\mathrm{W}}} \cdot k_{\mathrm{Naf,Dry}}}{\frac{1}{c_{\mathrm{SO3-}} \cdot M_{\mathrm{W}}} + \frac{\lambda_{\mathrm{W}}}{\rho_{\mathrm{W}}}}, \tag{5.4}$$

where k_{W} is the water thermal conductivity in (W/(m · K)), $c_{\mathrm{SO_3^-}}$ the sulfonic ion concentration in Nafion in mol/l, ρ_{W} the density of water in kg/m^3, M_{W} the molar mass of water in kg/kmol and $k_{\mathrm{Naf,Dry}}$ the thermal conductivity of the dry Nafion membrane. This last value can be approximated, according to a previous publication of Marquardt, Valadez Huerta et al [16], by:

$$k_{\mathrm{Naf,Dry}} = -0.0009 \cdot T + 0.4432. \tag{5.5}$$

An iterative estimation of the heat flux J_{q} through the test cell, neglecting the contributions from the other terms from Eq. 4.6, results in:

$$J_{\mathrm{q}} = \sum_{\mathrm{n}} \frac{1}{r_{\mathrm{n}}} \cdot \Delta T = \frac{k_{\mathrm{n}}}{d_{\mathrm{n}}} \cdot \Delta T \tag{5.6}$$

The temperatures at the reaction layers can now be calculated as:

$$T^{\mathrm{am}} = T^{\mathrm{A}} + J_{\mathrm{q}} \cdot (r_{\mathrm{P}} + r_{\mathrm{GDL}}), \tag{5.7}$$

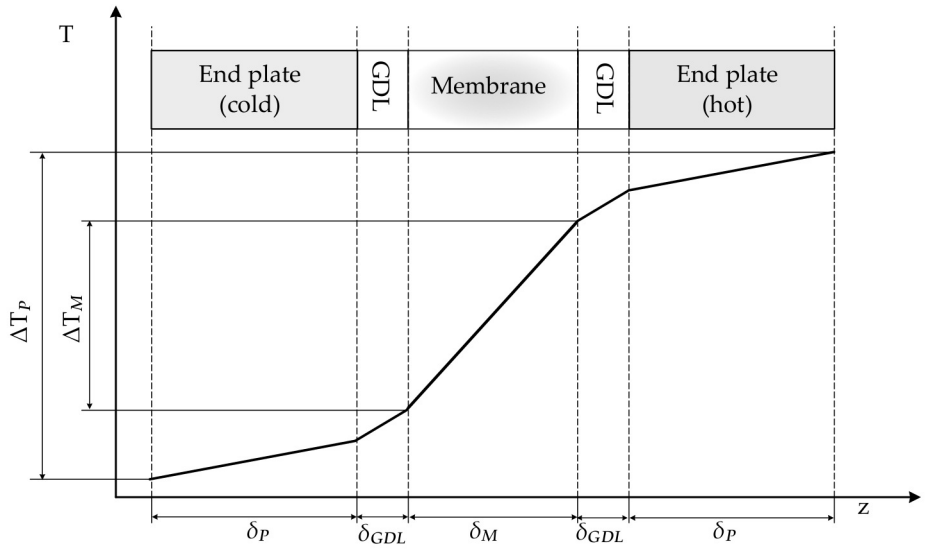

Figure 5.11: Temperature profle across the cell, modified from Marquardt et al. [16].

$$T^{\mathrm{cm}} = T^{\mathrm{C}} - J_{\mathrm{q}} \cdot (r_{\mathrm{P}} + r_{\mathrm{GDL}}), \tag{5.8}$$

so that once the temperatures $T^{\mathrm{am}}, T^{\mathrm{cm}}$ are known, the water chemical potential at the reaction layers can be estimated by an iteration procedure, taking the water partial pressure $(p_{\mathrm{w}}^{\mathrm{am}}, p_{\mathrm{w}}^{\mathrm{cm}})$ as the iterated value. It is then necessary to adjust the water mass flow at every electrode for the measurement series to achieve $\Delta\mu_{\mathrm{H_2O}} = 0$.

Chapter 6

Results and Discussion

The solid oxide electrolyte 3YSZ as well as the polymer electrolyte Nafion N1110 were extensively investigated by means of, among others, $U-j$ characteristics and Electrochemical Impedance Spectroscopy (EIS). Measurements were carried out when the test cells showed constant values, so that a steady state could be assumed. The directly measured values, eg. $x = T, \dot{m}, U, I$, are recorded at a frequency f over a period of time t so that n measured points are obtained, $n = 1 \dots i \dots n$. Averaging x gives the mean value $\overline{x}$ and the quality of the mean value is estimated with the standard deviation σ_{x}:

$$\overline{x} = \frac{1}{n^2}\Big(\sum_{\mathrm{i}=1}^{\mathrm{n}} x_{\mathrm{i}}\Big), \tag{6.1}$$

$$\sigma_{\mathrm{x}} = \sqrt{\frac{1}{n^2}\sum_{\mathrm{i}=1}^{\mathrm{n}}(x_{\mathrm{i}} - \overline{x})^2}, \tag{6.2}$$

so that they can be expressed as $x = \overline{x} \pm \sigma_{\mathrm{x}}$. Moreover, the quantities that are not measured, but which dependent on measured variables through functions $y = f(x_1, \dots, x_{\mathrm{j}}, \dots, x_{\mathrm{m}})$, are also subject to experimental errors, which can be approximated by means of the propagation of uncertainty, in which case the error is estimated as the differential of the function $\mathrm{d}y$:

$$\sigma_{\mathrm{y}} \approx \mathrm{d}y = \sum_{\mathrm{j}=1}^{m} \Big|\frac{\partial y}{\partial x_{\mathrm{j}}}\Big|\sigma_{\mathrm{x_j}} \tag{6.3}$$

and they are to be expressed as $y = y(\overline{x}_{\mathrm{j}}) \pm \sigma_{\mathrm{y}}$ thereafter.
The temperature, voltage and pressure raw data was collected with measuring cards and chassis from National Instruments and their software Labview, in their version 2018. The EIS was collected with the software provided by Solartron Analytical, XM studio ECS. All

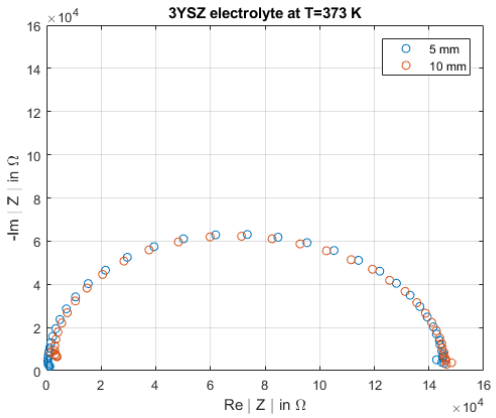

Figure 6.1: Nyquist plot measured for 3YSZ electrolytes in two thicknesses, $5-10\,\mathrm{mm}$ at $T = 373\,\mathrm{K}$

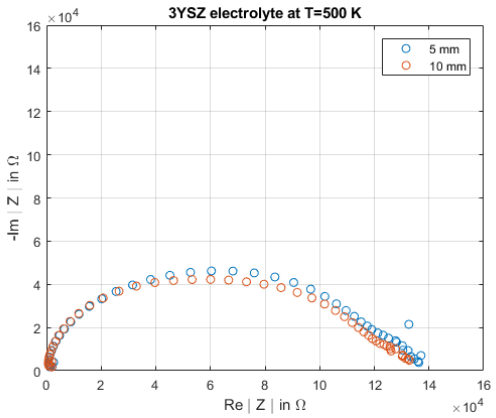

Figure 6.2: Nyquist plot measured for 3YSZ electrolytes in two thicknesses, $5-10\,\mathrm{mm}$ at $T = 500\,\mathrm{K}$

calculations and iterations have been carried out in Matlab®version 2017b. Fitting data was done with the user interface of the program XM studio ECS.

6.1 The solid oxide electrolyte

The ionic transport coefficient L_{OO} can be calculated from the diameter of the first semicircle (HF) of the Nyquist plot, given that no temperature gradient is present. From Eq. 4.8 it is known that the current density is given by:

$$\frac{\tilde{I}}{A} = -L_{\mathrm{OO}} \cdot \frac{(zF)^2}{T} \frac{\tilde{\Delta}\phi}{d^{\mathrm{E}}}. \tag{6.4}$$

Solving for the impedance $Z = \frac{\tilde{\Delta}\phi}{\tilde{I}}$ and considering that in the limit of frequencies ($f \to \infty$) the capacitance tends to zero, the impedance results in a resistance:

$$R_{\mathrm{f}\to\infty} = -\frac{1}{L_{\mathrm{OO}}} \frac{T}{(zF)^2} \frac{d^{\mathrm{E}}}{A} \tag{6.5}$$

The impedance spectra obtained experimentally were fitted using a series connection of 3 $R//C$ elements, as explained in Sec. 4.1.1 and depicted in Fig. 4.1. The 3YSZ pellets used as electrolytes presented two different thicknesses, $d^{\mathrm{E}} = 5$ and $10\,\mathrm{mm}$, in order to verify the geometry dependency of the sample, as both resistance R and capacitance C depend on the

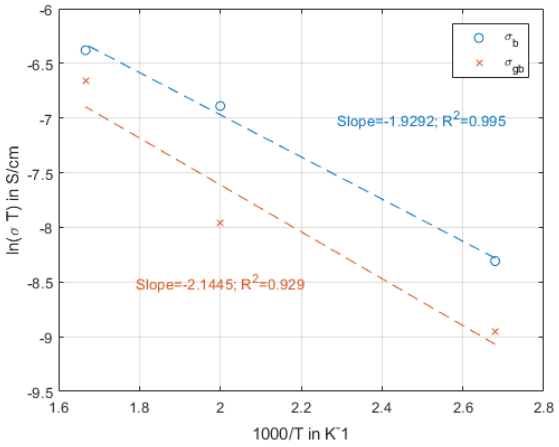

Figure 6.3: Arrhenius plot of the experimental bulk conductivity σ_b and grain boundary conductivity σ_gb for the 3YSZ electrolyte with thickness of 5 mm

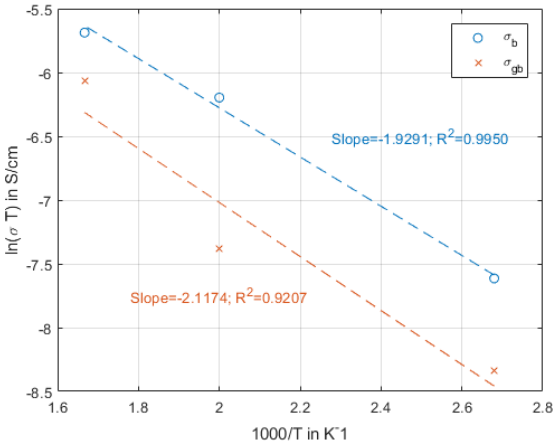

Figure 6.4: Arrhenius plot of the experimental bulk conductivity σ_b and grain boundary conductivity σ_gb for the 3YSZ electrolyte with thickness of 10 mm

geometry themselves. For a rectangular prism of height d and surface area A they result in:

$$R = \frac{1}{\sigma}\frac{d}{A}, \tag{6.6}$$

$$C = \varepsilon\frac{A}{d}, \tag{6.7}$$

where ε indicates the permittivity of the material, which is the material's ability of storing electric energy. The peak of the semicircle occurs at the characteristic frequency. Its inverse, the relaxation time τ of the electrochemical process, defined as the product of $R \cdot C$, so that the capacitance of the process can be calculated. The Nyquist plots for the 3YSZ electrolytes with both thicknesses are depicted in Fig. 6.1 for $T = 373\,\mathrm{K}$ and in Fig. 6.2 for $T = 500\,\mathrm{K}$. In both cases the impedance spectra show no observable difference, although both resistance and capacitance depend on the thickness d^E. This fact becomes more obvious when the measured conductivity is depicted vs. temperature, as shown in the Arrhenius plots of Fig. 6.3 for the pellet of $d^\mathrm{E} = 5\,\mathrm{mm}$ and Fig. 6.4 for the sample of $d^\mathrm{E} = 10\,\mathrm{mm}$. The conductivity is a specific property, thus independent on the geometry and therefore both samples should deliver the same line. This is not the case because the measurements of the thicker sample resulted in a higher conductivity. They show similar slopes, thus presenting a similar activation energy, which, as expected, should not dependent on geometry.

Compared to the values collected in the literature and summed up in Fig. 4.3 and Fig. 4.4 for bulk and grain boundary conductivity respectively, the conductivity measured from the

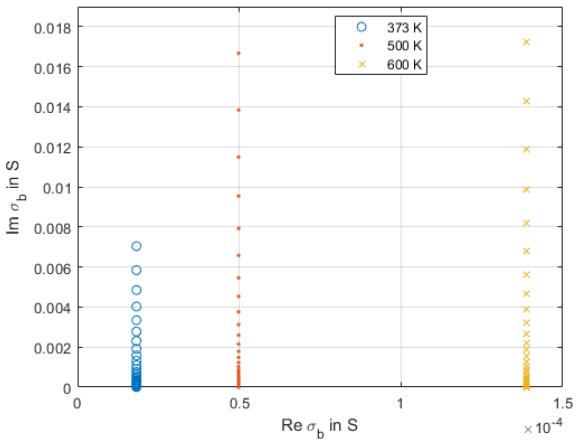

Figure 6.5: Measured bulk conductivity σ_b of the 3YSZ electrolyte at different temperatures for the frequency range $1 - 1 \cdot 10^6$ Hz, thickness 5 mm

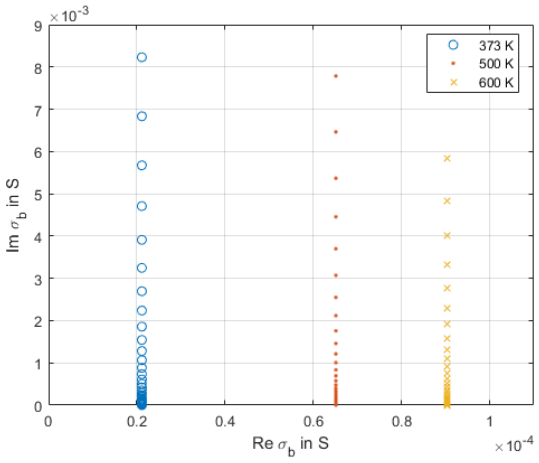

Figure 6.6: Measured bulk conductivity σ_b of the 3YSZ electrolyte at different temperatures for the frequency range $1 - 1 \cdot 10^6$ Hz, thickness 10 mm

samples in this study were considerably lower, at least 2 orders of magnitude. It becomes clear that the determination of the transport coefficients L_{ij} can now only be qualitative. For a quantitative approach it is necessary to reproduce values from literature with the test bench. Much effort was put in finding the source of these large deviations, which led to small improvements only. Unfortunately they proved to be insufficient for the purpose aimed for. The obtained bulk conductivity spectra were calculated as indicated in Eq. 4.20, and the results for the frequency range $1 - 1 \cdot 10^6$ Hz are depicted in Fig. 6.5 for the 5 mm sample and in Fig. 6.6 for the 10 mm electrolyte. When compared to the simulated curve illustrated in Fig. 4.10 it becomes clear that it is not possible to differentiate the effect of the transport coefficients in this range. The hypothesis of reducing the temperature to increase the relaxation time of the ionic bulk conduction seems to be correct but insufficient, since the relaxation time is still too low for the lowest measurement point presented from this setup.
The effect of the coupled coefficient L_{Oq} has been, however, observed, as shown in Fig. 6.7 and 6.8 for temperatures $T = 500$ K and $T = 600$ K, respectively. This means that it is still possible to approximate this conductivity, which is explained in Sec. 6.1.2. For the lowest temperature, $T = 373$ K the complete spectra remained unchanged despite of the applied temperature difference, so that it was discarded for further analysis.

Table 6.1: Calculated ionic transport coefficient L_{OO} of 3YSZ at different temperatures from samples of two thicknesses

L_{OO} in 10^{-12} $\frac{mol^2K}{J\,m\,s}$	$T = 373\,K$	$T = 500\,K$	$T = 600\,K$
$d = 5\,mm$	-0.57	-2.09	-5.82
$d = 10\,mm$	-1.32	-5.47	-13.78

6.1.1 The conductivity L_{OO}

The conductivity L_{OO} was calculated from R_b from Eq. 6.5, the results are summed up in Table 6.1. As previously stated there is a difference in the conductivity obtained for the different samples, which cannot be explained physically, since this value ought to be independent from the geometry. It is believed that the reasons for these deviations lie in the test bench, as its complex parts have caused experimental distortions in the past. Nevertheless, the conductivity increases at increasing temperatures, as expected.
It is believed that the commercial blocks used for the measurements have some impurities in the composition, which could explain the deviations observed. Another cause could be the electrodes used, since it was not possible to determine quantitatively how homogeneous the Pt-layer was, and if its thickness varied from sample to sample. Moreover, not having calcined the Pt-meshes to the brushed electrodes could also cause an increased contact resistance.
All these factors of influence must be studied in detail before a precise quantitative determination of the coefficients is carried out. The time this work would consume was out of the scope of this thesis.

6.1.2 The conductivity L_{Oq}

As the conductivity spectra show no variation in the measured frequency range, it is not possible to calculate the transport coefficients based on the model presented. Also it was not possible control the heat flux in a manner that a zero net heat flux could be measured and corrected. One approach to calculate the conductivity L_{Oq} is based on the definition of the Seebeck coefficient as the variation of the electric potential when a temperature difference is applied and no current flows through the system. If Eq. 4.8 is solved for the ratio $\Delta\phi/\Delta T$, Eq. 6.8 results:

$$\left(\frac{\Delta\phi}{\Delta T}\right)_{j=0} = \frac{L_{Oq}}{L_{OO}}\frac{1}{zFT} \tag{6.8}$$

Obtaining the coupled coefficient L_{Oq} from the slope of the $U_{OC} - \Delta T$ becomes difficult in this case, because the samples showed a base potential of around 6 mV. It was found that

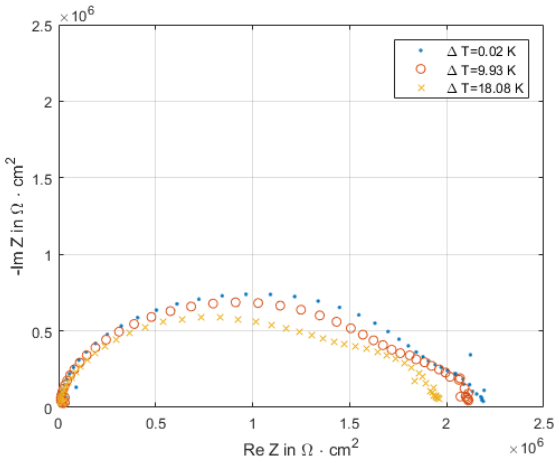

Figure 6.7: Measured Nyquist plot of the 3YSZ electrolyte at $T = 500\,\mathrm{K}$ and different applied temperature gradients. Thickness 5 mm

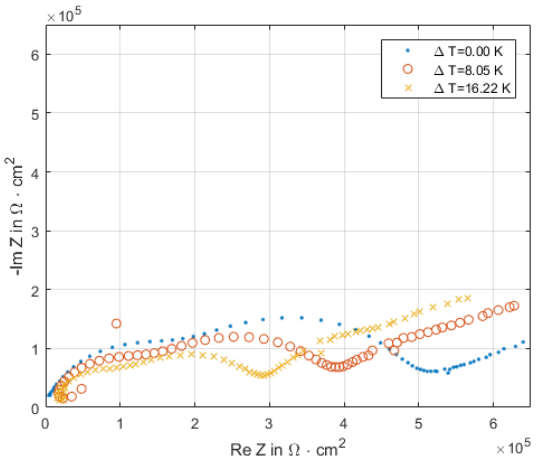

Figure 6.8: Measured Nyquist plot of the 3YSZ electrolyte at $T = 600\,\mathrm{K}$ and different applied temperature gradients. Thickness 5 mm

the cleaning process applied, as described from Toghan, [93] was insufficient to obtain clean samples, i.e. that would deliver zero electric potential when neither temperature nor chemical potential gradients were applied. The samples were polished thereafter with diamond-hard discs to reach this zero potential condition. Unfortunately, after brushing once more the Pt-paste to obtain the electrodes, the offset potential was observed again. The small temperature gradients which the test bench allows to apply caused a raise in the electric potential, but the increase of less than 1 mV was still in the uncertainty region of the measured offset. Therefore it was decided to approximate L_{Oq} from another point of view. In the experimental case, the net heat flux J_{q} was not absent, so that the measured temperature difference, as from Eq. 4.6, in this case results in:

$$\frac{\Delta T}{d^{\mathrm{E}}} = -\frac{T^2}{L_{\mathrm{qq}}}\Big(J_{\mathrm{q}} + L_{\mathrm{Oq}}\frac{zF}{T}\frac{\Delta\phi}{d^{\mathrm{E}}}\Big). \tag{6.9}$$

Replacing the temperature difference in electric current, in this case Eq. 4.8 reads:

$$j = \frac{L_{\mathrm{Oq}}}{L_{\mathrm{qq}}} zF J_{\mathrm{q}} - \Big(L_{\mathrm{OO}} - \frac{L_{\mathrm{Oq}}^2}{L_{\mathrm{qq}}}\Big)\frac{(zF)^2}{T}\frac{\Delta\phi}{d^{\mathrm{E}}}. \tag{6.10}$$

Solving for the electric potential to determine the impedance afterwards gives:

$$\frac{\Delta\phi}{d^{\mathrm{E}}} = \Big[j - \frac{L_{\mathrm{Oq}}}{L_{\mathrm{qq}}} zF J_{\mathrm{q}}\Big]\Big(-\frac{T}{(zF)^2}\frac{L_{\mathrm{OO}}L_{\mathrm{qq}} - L_{\mathrm{Oq}}^2}{L_{\mathrm{qq}}}\Big). \tag{6.11}$$

Table 6.2: Calculated conductivity L_{Oq} at different temperatures for two thicknesses

L_{Oq} in $(10^{-4})\,\frac{\mathrm{mol\,K}}{\mathrm{m\,s}}$	$T = 500\,\mathrm{K}$	$T = 600\,\mathrm{K}$
$d = 5\,\mathrm{mm}$	-3.93	-4.04
$d = 10\,\mathrm{mm}$	-2.69	-6.78

Considering that the square of the cross-coupled coefficient is much smaller than the product of the main coefficients, i.e. $L_{\mathrm{Oq}}^2 << L_{\mathrm{OO}} L_{\mathrm{qq}}$, it can be concluded for the electric potential:

$$\Delta\phi \approx \frac{1}{L_{\mathrm{OO}}} \frac{T}{(zF)^2} \frac{A}{d^{\mathrm{E}}} I + \frac{L_{\mathrm{Oq}}}{L_{\mathrm{OO}} L_{\mathrm{qq}}} zF \frac{A}{d^{\mathrm{E}}} J_{\mathrm{q}}. \tag{6.12}$$

In Eq. 6.12 the thermodynamic forces and fluxes should be close to local equilibrium. The total current I results as the sum of a direct current $\overline{I}$ and a periodic current $\tilde{I}$, $I = \overline{I} + \tilde{I}$. Impedance spectroscopy imposes the periodic one. As it has been stated before, the periodic excitation causes a periodic response, so that the steady state part can be considered negligible. Eq. 6.12 is now rewritten and divided by $\tilde{I}$ to finally obtain the frequency dependent impedance:

$$\frac{\Delta\tilde{\phi}}{\tilde{I}} = \frac{1}{L_{\mathrm{OO}}} \frac{T}{(zF)^2} \frac{A}{d^{\mathrm{E}}} + \frac{L_{\mathrm{Oq}}}{L_{\mathrm{OO}} L_{\mathrm{qq}}} zF \frac{A}{d^{\mathrm{E}}} \frac{\tilde{J}_{\mathrm{q}}}{\tilde{I}}, \tag{6.13}$$

where the first term can be identified as the impedance when no temperature gradient is present, Eq. 6.4, so that the second term must represent the difference.

The heat flux can only be approximated by neglecting the coupled term, so that the transport coefficient L_{Oq} can be approximated by means of the temperature difference, which was indeed measured. All these assumptions taken, the calculated conductivity is given in Table 6.2. The transport coefficient is temperature dependent, as expected. The Seebeck coefficient has shown to be temperature dependent for other materials at the same temperature range [98], [99].

On the other hand, the coupled conductivity shows a thickness dependency, which contradicts the linear approach in NET, that transport coefficients do not depend on the thermodynamic force. They are calculated from the temperature gradient (the thermodynamic force) applied to the electrolyte, both thicknesses should deliver the same value. It is believed that the assumptions made during the deduction of Eq. 6.13 have a larger influence than thought and they shall be revised. Alternatively, the temperature difference could be imposed in smaller steps to prove if this behaviour is observed again. This would require, however, more precise thermocouples, otherwise the thermocouples uncertainty will be larger than the measured

Table 6.3: Approximation of the phenomenological coefficients with classical transport coefficients given by Kjelstrup and Bedeux [14]

NET coefficient	KJE orig.[14]	Auxiliary equation(s)
$L_{\phi\phi}$	$\sigma^M \cdot T$	[3.4], [3.5]
$L_{\phi\mu}$	$\frac{t}{F} \cdot L_{\phi\phi}$	[3.6]
$L_{\phi \mathrm{q}}$	$S \cdot T \cdot L_{\phi\phi}$	[2.31]

value. Furthermore, the direction of the thickness dependency is contradictory, increasing at $T = 600\,\mathrm{K}$ and decreasing at $T = 500\,\mathrm{K}$. This could also be a hint of experimental error, supporting the previous idea of coefficients independent of thickness.
Finally, the general size of the samples could influence the measurements. They were chosen big enough to discard boundary effects and thick enough to make the coupling observable. One could argue that they might be too thick; Kjelstrup and Tomii [100] measured the Seebeck coefficient of YSZ with a thicker sample, $d = 150\,\mathrm{mm}$, so that it is strongly believed that the size of the samples used in this setup is appropriate.
More care should be taken, however, in the composition and manufacture of the samples. For further investigation it is recommendable to use laboratory pellets of a more homogeneous composition rather than the commercially available pellets. The provider of the samples used could say neither how the precursor powder was obtained nor how the blocks were shaped, so that no conclusions can be made from the sample prehistory.

6.2 The polymer electrolyte

The results here presented have been partially presented at the *DECHEMA Thermodynamik Kolloquium 2021*, held virtually in September 2021.

Since NET is not a widespread model approach, there are not many experimental values for the special transport coefficients available in the literature which are needed in this approach. As already mentioned, one possibility consists of approximating the phenomenological coefficients with classical coefficients; this approach was extendely used by Kjelstrup and Bedeux [14] for the PEM fuel cell, and more precisely, the polymer electrolyte. In that case, the main coefficients L_{ii} are calculated based on the proportionality factors of the mono-causal transport equations, see Sec. 2.4, whereas the cross coefficients $L_{\mathrm{ij}}(i \neq j)$ are defined by means of the proportionality factors of coupled transport processes, as already expressed in

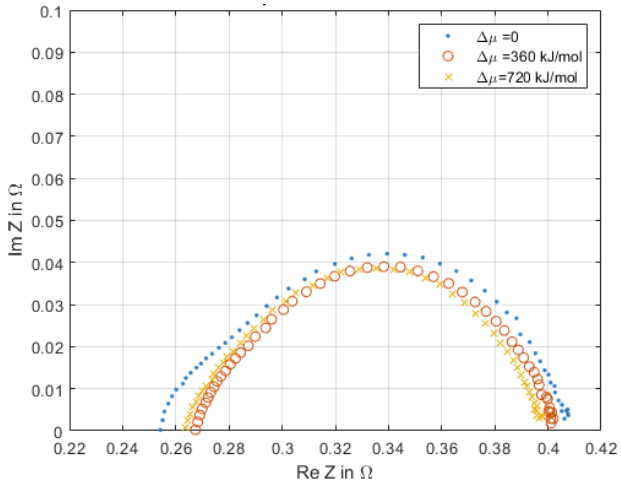

Figure 6.9: Nyquist plot of the polymer electrolyte fuel cell at a constant temperature $T = 333\,\mathrm{K}$ and a mean water activity $\frac{p_\mathrm{W}}{p_\mathrm{W}^\mathrm{S}} = 0.60$ under variation of the water chemical potential.

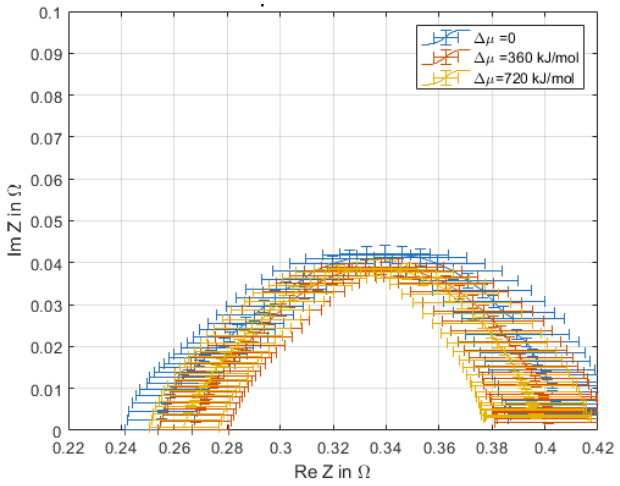

Figure 6.10: Nyquist plot of the polymer electrolyte fuel cell at a constant temperature $T = 333\,\mathrm{K}$ and a mean water activity $\frac{p_\mathrm{W}}{p_\mathrm{W}^\mathrm{S}} = 0.60$ considering the measurement uncertainty

Sec. 2.5. The resulting equations are summed up in Table 6.3. The original approach of Kjelstrup and Bedeux, shorten **KJE orig.**, approximates the ionic conductivity with the first experimental data from Los Alamos Laboratory, making use of too many assumptions since they did not have other experimental values. As already mentioned, measures of water content versus water activity at $T = 353\,\mathrm{K}$ have shown that the polynomial for $T = 303\,\mathrm{K}$ is not valid for this temperature [57]. Therefore, the water content for the nafion membrane in the temperature range $T = 303 - 353\,\mathrm{K}$ should be corrected using a weighted mean:

$$\lambda^\mathrm{M}(T) = \lambda^\mathrm{M}_{303}\Big(\frac{353 - T}{50}\Big) + \lambda^\mathrm{M}_{353}\Big(\frac{T - 303}{50}\Big), \tag{6.14}$$

where λ^M_{303} is obtained from Eq. 3.4 and λ^M_{353} by means of Eq. 3.8. This modified value is then used to calculate the ionic conductivity and referred to as **KJE modif.**

As previously stated in Sec. 4.2, the water transport $J_{\mathrm{H_2O}}$ in the membrane shall be visible in the low frequency region of the impedance curve. In the experiments carried out it was not possible to investigate this region because of the measuring conditions: the OCV showed a sinusoidal-like behaviour with neither non-negligible amplitude nor frequency(-ies). In statistical terms the OCV standard deviation is small in comparison to the mean OCV, but its frequency(-ies) interferes with the EIS frequency. These disturbances influenced the $U - j$ characteristics in a way, that they cannot be included in this analysis. An shown by Fig. 6.12 for the test cell measured at $T = 333\,\mathrm{K}$ and a mean water activity $a_{\mathrm{H_2O}} = 0.60$ imposed to a

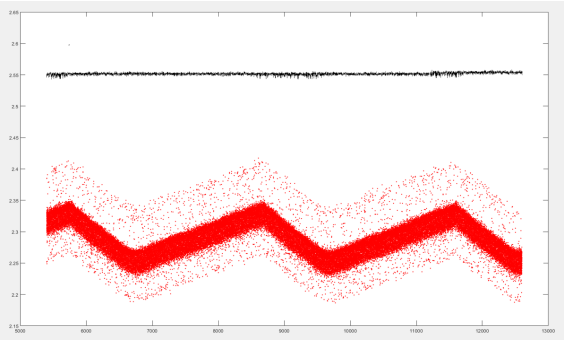

Figure 6.11: Measured pressure of compressed air in line (black) and at the top of the water tank (red). The curves are qualitative, thus out of scale.

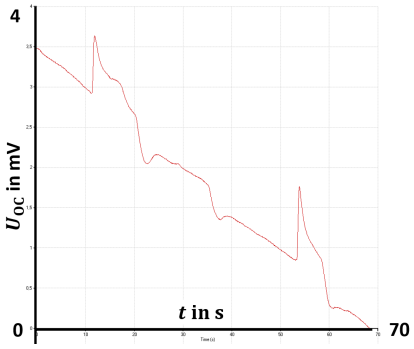

Figure 6.12: U_{OC} vs. time measured for the PEM test cell at a constant temperature $T = 333\,\mathrm{K}$ and a mean water activity $\frac{p_W}{p_W^S} = 0.60$, exposed to a water chemical potential of $360\,\mathrm{J/mol}$.

water chemical potential difference of $360\,\mathrm{J/mol}$ the OCV did not remain constant over time. A closer look in the system showed that this frequency was observed not in the compressed air line but in the water tank, as shown in Fig. 6.11. This observation can be explained by the function principle of the inlet valves of the coriolis mass flow controllers for water. As for the observed frequencies (one for each CMC), the inlet valve appears to follow an ON/OFF actuator, which is in accordance with the very small water mass flow rates ($10 - 100\,\mathrm{g/h}$). A possible solution could be the introduction of a buffer system between evaporator and test cell, so that the mass flow fluctuations can be reduced. Even with this changes it can not be assured that the OCV will be constant enough for the EIS in the low frequency range ($1 - 10^{-3}\,\mathrm{Hz}$). Such modifications are unfortunately outside the time scope of the thesis work presented here, considering the time-consuming assembly and adjustment of the test bench.

Nevertheless, it must be pointed out that even with stable measuring conditions it becomes challenging to observe the influence of water transport by means of EIS, i.e. of the coupled coefficient $L_{\phi\mu}$. As already mentioned, Kadyk et al. [89] measured the impedance of a H_2/air cell in the frequency range $10^3 - 10^{-2}\,\mathrm{Hz}$, as given in Fig. 4.17. It can be observed how the inductive loop shows the influence of the water transport at the lowest frequencies, as well as the scatter of these points and their large uncertainties. More recently, Kosakian and Secanell [101] reached $10^{-1}\,\mathrm{Hz}$, in this case for a H_2/O_2 cell, their Nyquist plots are depicted in Fig. 6.13 for low current densities and in Fig. 6.14 for higher current densities. The experimental data is compared to their simulations (plotted to $10^{-4}\,\mathrm{Hz}$). As it can be observed, they are qualitatively in good agreement, but the measured impedance spectra shows larger relaxation times than the simulated ones, so that the characteristic frequency of the loop is found at lower frequencies.

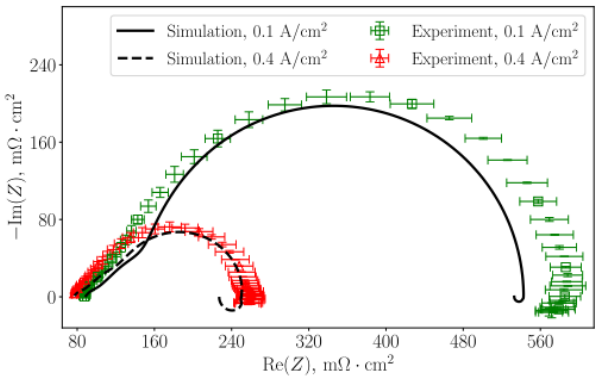

Figure 6.13: Kosakian and Secanell [101] experimental data compared to simulated Nyquist plots of the water transport in a H_2/O_2 cell at $T = 353\,\mathrm{K}$ and $\mathrm{rH} = 50\%$ at low current densities.

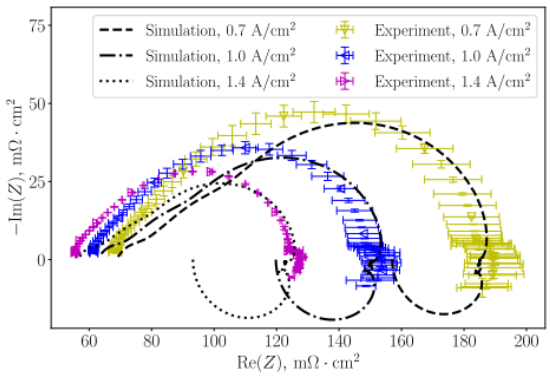

Figure 6.14: Kosakian and Secanell [101] experimental data compared to simulated Nyquist plots of the water transport in a H_2/O_2 cell at $T = 353\,\mathrm{K}$ and $\mathrm{rH} = 50\%$ at high current densities.

It is believed that their test bench was also fluctuating during the low frequency measurements, therefore they did not go further down. As it can be seen, there is multiple evidence of the inductive loop being caused by the water transport, however, it is up to date difficult to obtain constant conditions in the test facilities. Measuring under $10^{-2}\,\mathrm{Hz}$ takes several hours, meanwhile the electrochemical system must remain very stable and invariant.

6.2.1 The conductivity $L_{\phi\phi}$

The conductivity $L_{\phi\phi}$ was calculated from the High Frequency Resistance (HFR) as previously explained in Sec. 4.2.2.1, so that from Eq. 4.30 the conductivity $L_{\phi\phi}$ is obtained as:

$$L_{\phi\phi} = -\frac{d \cdot T}{A \cdot R_0}. \tag{6.15}$$

Table 6.4: Experimental values for the conductivity $L_{\phi\phi}$ compared to the calculated conductivity, as proposed by Kjelstrup and Bedeux, the original approach [14] (KJE orig.) and a modified one with Eq. 6.14 (KJE modif.)

	$T = 333\,\mathrm{K}$		$T = 348\,\mathrm{K}$	
	$\frac{p_W}{p_W^S} = 0.60$	$\frac{p_W}{p_W^S} = 0.85$	$\frac{p_W}{p_W^S} = 0.60$	$\frac{p_W}{p_W^S} = 0.85$
This work	-684.04 ± 34.20	-1300.13 ± 65.00	-595.61 ± 29.78	-1384.34 ± 69.21
KJE mod.	-593.84	-1149.21	-615.56	-1097.95
KJE orig.	-879.37	-1962.00	-1082.90	-2416.10

The obtained values are summarised in Table 6.4.
The original approach, ie. KJE orig. found in the literature, overestimates the coefficient L_{OO} at all four measured temperatures and water chemical potentials, with a deviation up to $\Delta L_{OO} \approx 90\%$. This shows that the approach can only be considered for temperatures and relative humidity levels close to the original measurements. When compared to the values obtained with the water content weighted mean KJE modif., it is observable that the experimental data obtained here agrees with the ones obtained from the model, showing a deviation of $\Delta L_{OO} = 3 - 15\,\%$. Moreover, the deviation is stochastic, ie. for some cases positive and for some negative, so that no systematic can be recognised. The ionic conductivity dependency on the water content expressed in Eq. 3.5 was also measured only for $T = 303\,\mathrm{K}$. Using this value for higher temperatures might also not be entirely correct; the lack of more data makes it necessary to determine it experimentally.

6.2.2 The conductivity $L_{\phi\mu}$

As previously stated in Sec. 4.2.2.2, the conductivity $L_{\phi\mu}$ can be calculated from the slope of the $U - \Delta\mu$ curve. As this approach calculates the phenomenological coefficient proportional to L_{OO}, it is preferred to compare the experimental raw data, i.e. the slopes, rather than the calculated coefficients, to avoid the deviation propagation ΔL_{OO} stated in the previous section. To obtain the accurate slope, it turns out that it is necessary to determine the chemical potential of water vapour at the boundary surfaces of the membrane. Since Eqs. 5.2 and 5.3 depend on assumptions, their calculation should only be considered as an approximation. In this case, the temperature across the cell is constant, so that the water chemical potential depends only on the water partial pressure at the triple phase boundary (TPB). As a direct measurement of the relative humidity is per se complicated, it becomes almost impossible to do so for an uncertain location, given that the TPB is only a few nm thick. It is, however, possible to calculate the chemical potential at the membrane knowing the water partial pressure at the cell inlet, which can be fixed to a certain value. Different studies have shown different parameterisation [86], [87] of the water transport through the GDL. For that reason,

Table 6.5: Slopes of the $U - \Delta\mu$ curves obtained experimentally.

t in $\frac{\mathrm{mV}}{\mathrm{kJ/mol}}$	$\frac{p_W}{p_W^S} = 0.60$	$\frac{p_W}{p_W^S} = 0.85$
$T = 333\,\mathrm{K}$	7.187	4.859
$T = 348\,\mathrm{K}$	7.219	8.015

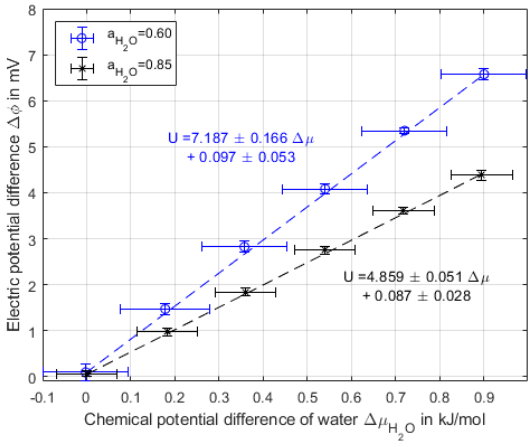

Figure 6.15: $U_{\mathrm{OC}} - \Delta\mu$ curves measured at $T = 333\,\mathrm{K}$ and water activities $\frac{p_{\mathrm{W}}}{p_{\mathrm{W}}^{\mathrm{S}}} = 0.60, 0.85$

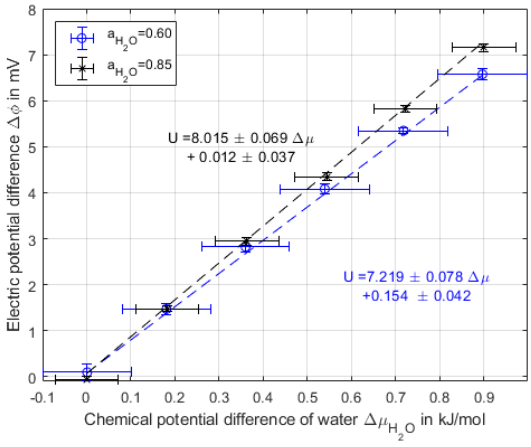

Figure 6.16: $U_{\mathrm{OC}} - \Delta\mu$ curves measured at $T = 348\,\mathrm{K}$ and water activities $\frac{p_{\mathrm{W}}}{p_{\mathrm{W}}^{\mathrm{S}}} = 0.60, 0.85$

as a first approach, the water activity was considered to be constant through the GDL. This assumption shall be discussed further in light of the results.

The measured electric potentials versus the water chemical potential difference at the membrane $\Delta^{\mathrm{M}}\mu$ at the water activities $\frac{p_{\mathrm{W}}}{p_{\mathrm{W}}^{\mathrm{S}}} = 0.60$ and 0.85 are depicted in Fig. 6.15 for $T = 333\,\mathrm{K}$ and in Fig. 6.16 for $T = 348\,\mathrm{K}$. The experimental values are summed up in Table 6.5.

According to the approach given in KJE orig., the slope of the $U_{\mathrm{OC}} - \Delta\mu$ curve determines the transfer number t:

$$\frac{\Delta\phi}{\Delta\mu} = \frac{t}{F}. \tag{6.16}$$

KJE orig. modeled the transport coefficient $L_{\phi\mu}$ with a transfer number measured by Ottøy [102], who obtained $t = 1.2$ at $T = 298\,\mathrm{K}$. In that case, the slope $\frac{\Delta\phi}{\Delta\mu}$ results $12.437\,\mathrm{mV/(kJ/mol)}$. They assume this value to be constant for all temperatures. When compared to the experimental values of this work (Table 6.5), it is clear that this value overestimates the transfer number. If the value obtained for $T = 353\,\mathrm{K}$ and $\frac{p_{\mathrm{W}}}{p_{\mathrm{W}}^{\mathrm{S}}} = 0.85$ is excluded (it can be considered as an outlier, as at a given temperature the transference number should be constant or increase at increasing water activity), the deviation from the model is around 40% (more precisely $35 < \Delta L_{\phi\mu}\,\mathrm{in}\,\% < 42$).

From the experimental data obtained, the transfer number depends on both temperature and water activity, contradicting the observations from Zawodzinski et al. [59]. As shown by the contradictory results obtained at similar laboratory conditions from Springer et al.[12] and from Fuller and Newman, [58] the region of low water activity requires a deeper investigation, as it might take longer than expected to reach equilibrium in this situation. The chemical

potential of water vapour as determined in this study is very uncertain. This could be one cause for the large deviation between the literature data and this study. It was assumed here that an hour should be sufficient for water vapour to humidify the five membranes homogeneously, which can be questioned considering the results obtained here.
Another cause of deviations could lie in other components present in the test cell used. The largest source of uncertainty lies within the unknown water transport at the GDL: considering the water activity to be constant through the GDL might underestimate the transfer number of the membrane, as it neglects the water concentration losses due to diffusion. Up to date and as far as concerned, there is no model available in the literature for carbon cloth based GDLs, so even modeling the concentration loss analogously to carbon paper GDLs would not be entirely correct, thus this is a possible improvement for future work in this matter.
Furthermore, the GDLs might cause distortions larger than what has been expected, given their thickness of 2/3 of the electrolyte thickness. As pointed out by Rezaei Niya, [84] the GDLs also present a transfer number t_{GDL}, which can be neglected if they are thin compared to the membrane and if the latter is sufficiently humidified. For this study it was not possible to reduce the GDL thickness due to the deepening of the flow field found in the mono-polar plate.
When compared to other experimental data, it must be pointed out that they are based mostly on ex-situ methods: neither Mottøy nor Zawodzinksi investigated the membranes in situ; they measured the potential of half cells in equilibrium with HCl solutions. This method might facilitate the determination of the water content, but could lead to an overestimation of the parameters in question, as the membrane is in ideal conditions, see Sec. 2.7 for further details.
More important to determine the deviation between KJE orig. approach and the experimental data is to map the temperature and water activity functions. As it can be seen from the values obtained, two temperatures and two water partial pressures are not sufficient to conclude how the conductivity $L_{\phi\mu}$ depends on these thermodynamic quantities in detail.

6.2.3 The conductivity $L_{\phi\mathbf{q}}$

In analogy to $L_{\phi\mu}$, the phenomenological coefficient $L_{\phi\mathrm{q}}$, coupling the electric potential to the temperature gradient, is proportional to the conductivity L_{OO}, so that the raw experimental data, in form of the slopes of the $U_{\mathrm{OC}} - \Delta\ T$ curves, is evaluated carefully. In this case, the slope of electric potential vs. temperature difference at open circuit turns out to be the Seebeck coefficient:

$$\left(\frac{\Delta\phi}{\Delta T}\right)_{\mathrm{j}=0} = S. \tag{6.17}$$

Table 6.6: Slopes of the $U - \Delta T$ curves experimentally obtained

S in mV/K	$\frac{p_W}{p_W^S} = 0.60$	$\frac{p_W}{p_W^S} = 0.85$
$T = 333\,\mathrm{K}$	0.600	0.692
$T = 348\,\mathrm{K}$	0.580	0.631

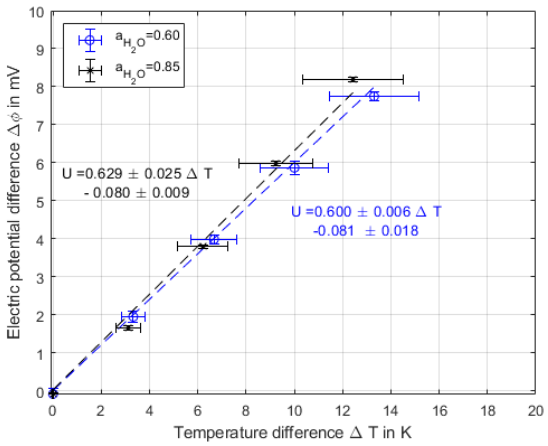

Figure 6.17: $U_{OC} - \Delta\, T$ curves measured at $T = 333\,\mathrm{K}$ and water activities $\frac{p_W}{p_W^S} = 0.60, 0.85$

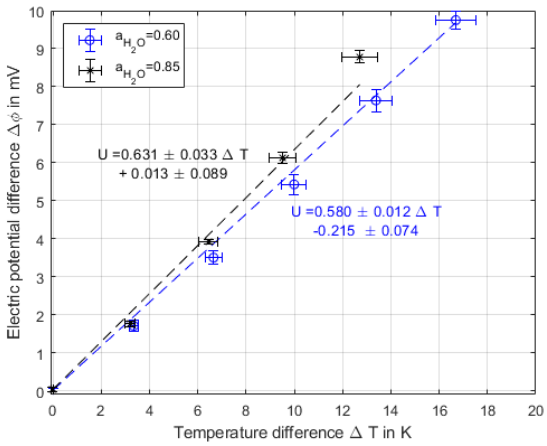

Figure 6.18: $U_{OC} - \Delta\, T$ curves measured at $T = 348\,\mathrm{K}$ and water activities $\frac{p_W}{p_W^S} = 0.60, 0.85$

To determine the Seebeck coefficient of the electrolyte requires the evaluation of the temperature difference at its boundary surfaces, i.e. at the TPB. Inserting thermocouples, whose diameter exceeds the TPB thickness did not seem appropriate when the test cell was designed. Instead of this, the temperatures needed were simulated with the model approach given in Sec. 5.2.2. Moreover, the potential losses at the electrodes are considered negligible for this case. The measured electric potentials versus the temperature difference $\Delta^M T$ for water activities $\frac{p_W}{p_W^S} = 0.60$ and 0.85 are depicted in Fig. 6.17 for $T = 333\,\mathrm{K}$ and in Fig. 6.18 for $T = 348\,\mathrm{K}$. The experimental values are summed up in Table 6.6.

KJE orig. models the coefficient $L_{\phi q}$ with the Peltier coefficient, which they calculated from the Seebeck coefficient using the Thomson relation ($\Pi = S \cdot T$). This approach introduces a further error source. Their attempts to measure the Peltier effect for the nafion membrane with two hydrogen electrodes [87] were not successful, but they could measure the Seebeck coefficient with a fair accuracy. In that study, the coefficient was determined to be $S = 0.67 \pm 0.05\,\mathrm{mV/K}$ at $T = 340\,\mathrm{K}$ for three membranes N1110 with a maximum temperature difference of $\Delta^M T \approx 25\,\mathrm{K}$. With a slightly different setup, Yang, Sun et al. [103] obtained $S = 0.531\,\mathrm{mV/K}$ at $T = 333\,\mathrm{K}$ with a membrane N117 and for a maximum

Table 6.7: Coupled conductivities $L_{\phi\mu}$ and $L_{\phi\mathrm{q}}$, experimentally obtained at $T = 333 - 348\,\mathrm{K}$ and $\frac{p_\mathrm{W}}{p_\mathrm{W}^\mathrm{S}} = 0.60 - 0.85$

	$T = 333\,\mathrm{K}$		$T = 348\,\mathrm{K}$	
	$\frac{p_\mathrm{W}}{p_\mathrm{W}^\mathrm{S}} = 0.60$	$\frac{p_\mathrm{W}}{p_\mathrm{W}^\mathrm{S}} = 0.85$	$\frac{p_\mathrm{W}}{p_\mathrm{W}^\mathrm{S}} = 0.60$	$\frac{p_\mathrm{W}}{p_\mathrm{W}^\mathrm{S}} = 0.85$
$L_{\phi\mu}$ in $\frac{\mathrm{K\,mol}}{\mathrm{m\,V\,s}}$	-4.916 ± 0.255	-6.317 ± 0.323	-4.300 ± 0.220	-11.095 ± 0.563
$L_{\phi\mathrm{q}}$ in $\frac{\mathrm{K\,A}}{\mathrm{m}}$	-136.74 ± 6.98	-272.54 ± 17.36	-120.21 ± 6.48	-304.23 ± 21.94

temperature difference of $\Delta^\mathrm{M}T = 15.3\,\mathrm{K}$. Their setup was a closed loop so that no hydrogen was consumed during their experiments, but it was recirculated between the electrodes, so that this internal circulation could have diminished the Seebeck effect to a small extend.
From the experimental data obtained in this work, reproduced in Table 6.7, it can be concluded that the conductivity slope depends on both temperature and water content, although the measured effect of increasing temperature and water content lies within the experimental uncertainty. The assumption can be supported by the values of Kjelstrup, Vie et al. [26], who measured it at water activities higher than 1, i.e. in the supersaturated range, reporting a higher Seebeck coefficient than the ones presented here.
Moreover, the calculation of the temperatures at the PTB instead of measuring (or trying to measure) them might underestimate the temperature difference at the electrolyte, thus underestimating the Seebeck coefficient of the membrane. Thus the data presented here is seen to be preliminary data, but it has proven the concept proposed in this work.

6.3 Further remarks on the polymer electrolyte results

As already proposed by Marquardt, Kube et al. [16], approximating the phenomenological coefficients L_ij to classical (mono-causal) transport coefficients might be valid only close to the measurement point. The greater the gradients are, the larger the deviations of the model will be, as shown here. Moreover, the empirical equations, e.g. for the water transport, obtained in the 1990s and early 2000s from data fitting have no physical background. Feasible explanations were developed to explain why the water content of Nafion remains fairly constant at increasing activities of water vapour for the regions of low water activity ($a_{\mathrm{H_2O}} = 0.2 - 0.8$, see Fig. 3.6). Two data gaps can be clearly recognised, reducing the quality of the fitting. Much effort was devoted into modeling the behaviour of Nafion, making use of the empirical equations obtained for a single temperature instead of actually measuring the water uptake

of the polymer at other temperatures, as well as the ionic conductivity at other temperatures and water contents.
In that sense, NET proves to be a powerful tool to explain the transport processes, as it follows a physical approach. The studies carried out here show that the phenomenological coefficients must be measured for different temperatures, water contents and loads; the latter was unfortunately not covered by this investigation. Approximating multi-causal transport coefficients L_{ij} to mono-causal coefficients (σ, κ, S, Π) reduces the advantages of the physical model of NET over the classical approaches.

Chapter 7

Conclusions and Outlook

Fuel cells convert chemical energy directly into electric energy without intermediate steps, thus reducing intermediate losses and circumventing limitation imposed by the Carnot efficiency. This direct energy conversion is possible due to the main component of the fuel cell, its electrolyte, separating electrical charges.

In this work, the complex transport mechanisms that occur in a fuel cell electrolyte were investigated. Two different electrolytes were studied, the polymer electrolyte used in low temperatures fuel cells (PEMFC), typical for mobile applications and the solid oxide electrolyte in high temperature fuel cells (SOFC), more appropriate for stationary operation.

The fluxes of mass, charge and thermal energy through the electrolyte were studied considering Non-Equilibrium Thermodynamics, a theory proposing multi-causality to explain the interaction between the thermodynamic forces acting within the electrolyte. This multi-causal approach has been proven to be more accurate than classical mono-causal approaches for membrane and/or electrochemical processes. By means of this theory it became possible to quantify the local entropy production rate, fundamental for an appropriate fuel cell design: the best entropy is the one which is never produced (by irreversibilities).

Non-Equilibrium Thermodynamics defines a set of proportionality factors between the linearised fluxes and thermodynamic forces; these coefficients are called transport coefficients or conductivities. The possible determination of the transport coefficients in an electrolyte applying Electrochemical Impedance Spectroscopy is the main hypothesis of this study. The Impedance Spectroscopy is a material characterisation technique widespread in the fuel cell research and electrochemical research. A time periodic electric signal is applied to an electrochemical system and its electric response is measured to determine the impedance of the system under investigation.

The challenge is to extract the different phenomenological coefficients out of the EIS signal

knowing about all assumptions and boundary conditions. Two different approaches were developed to find the relation between transport processes and impedance spectroscopy, one for each type of electrolyte.

The proposed model for the solid oxide electrolyte creates a relation between the transport mechanisms of ions and thermal energy and the frequency dependent impedance. Unfortunately, the very low relaxation time of some of these electrochemical transport processes made it very difficult to validate this approach with experimental data. The low relaxation time requires too large frequencies, which is a challenge for the EIS to detect. Furthermore, the test facilities presented here are believed to cause some distortion in the measurement (e.g. the OCV of the PEM test cell, the offset voltage of the solid oxide electrolyte), so that reproduction of well established literature values was difficult. The differences between the measurements carried out here and reported in literature could be connected to the samples structure, however. One possible factor is the concentration of impurities in the commercial ceramic samples. No post-mortem analysis has been carried out yet, because the samples had to be used by the research team after the experimental work presented here. That is one reason why it is not possible to determine the homogeneity of the samples on behalf of their composition.

Nevertheless, an approximate calculation of the transport coefficients was carried out. The ionic conductivity was obtained from the Middle Frequency Resistance (MFR) of the impedance spectrum, prior fitting to an equivalent circuit consisting of 3 $R//C$ elements. Furthermore, on behalf of the influence of the heat and coupled transport, which has been experimentally observed, an approximate qualitative method to determine the coupled transport coefficient has been proposed. The results are conclusive to a limited extend only, as they show contradictions in temperature dependencies. As far as concerned, there are no studies that have determined these transport coefficients for 3YSZ ceramics at intermediate temperatures ($T = 300 - 600\,\mathrm{K}$), so that it was not possible to compare the values obtained here with literature data.

As for the polymer electrolyte, an equivalent circuit to determine the transport coefficients of the electrolyte has been proposed. This equivalent circuit is based on the process modeling approach and some special equivalent circuits already established in the literature, adapting them to the experimental conditions of this work, i.e. the condition of two hydrogen electrodes. The fitting of the measured impedance to the proposed model was possible only to a limited extend, due to the large contribution from the gas diffusion layers to the overall impedance. Moreover, the function principle of the mass flow controllers for water is believed to cause a sinusoidal distortion in the cell inlet water flow, as the same frequency of this control system

has been observed in the electric potential measured at the test cell. This induced some low frequencies in the same range of the characteristic frequency of the water transport in the GDL and in the membrane, thus turning the determination of the coupled conductivity from the impedance spectra impractical. Fitting the spectra delivered poor results and was therefore discarded, even though this is a promising approach which should be followed in the future.

The ionic transport coefficient was obtained from the High Frequency Resistance (HFR) of the impedance spectrum, similar to the ionic conductivity. The coupled coefficients, i.e. the coupled heat and ionic conductivity as well as the coupled water and ionic conductivity, were calculated from the slopes of the $U - \Delta T$ and $U - \Delta\mu$ curves, respectively. A direct determination from impedance spectra was difficult due to the large distortions in the low frequency (LF) region, where they are to be observed. These values have been compared to an approach found in literature, where the transport coefficients are approximated to classical mono-causal coefficients. The coupling between water and ionic transport introduces a large deviation, which can be explained by the assumptions made by the authors. As for the coupling of heat and ionic transport, the results agree with the experimental findings presented in this work, taking into consideration the different water contents of the polymer electrolyte.

The experimental findings showed that coupling effects are observable and that the multi-causal approach given by Non-Equilibrium Thermodynamics cannot be neglected. A precise determination of the transport coefficients, either by means of EIS or OCV curves, requires a very precise and stable control of the test bench, enabling steady measuring conditions for days. It would be ideal to automatise the modifications carried out in both test benches, so that small deviations could be corrected as soon as possible. For example, temperature variations within 0.1 K cause measurable OCV deviations, so that they must be avoided. These conditions necessary to extract data at very low frequencies were not enabled in the setup presented here.

More experimental determination of the transport coefficients in the solid oxide electrolyte will require a new housing concept. The housing should allow the assembly of both heaters, external and compensation, in an easier way, so that it can be double checked if they are positioned correctly, otherwise it is difficult to determine whether they are in contact with the other elements of the housing or not. Moreover, the assembly of thermocouples should be enabled externally, preferably with extra boreholes, so that they do not lie within the flow field, obstructing the gas stream. Furthermore, the type and class of the thermocouples might be adequate for fuel cell research but insufficient for electrolytes. If possible, the temperatures

shall be measured with thermocouples type S, class 1, which have an uncertainty of max. 1 K at $T < 1300$ K, allowing also experiments at lower temperature differences.
In addition, the ceramic samples ought be traceable, i.e. composition and thermal prehistory should be available. Only in this manner it is possible to categorise the deviation sources and discard the influence of the chemical composition. The samples should be preferably developed and prepared for these experiments, rather than be commercially available samples. A post-mortem analysis (XRD, Raman Spectroscopy) should be carried out, as transverse homogeneity is extremely important for these experiments.
Similar modifications are desirable in the low temperature test rig for polymer electrolytes. The low temperatures enable the measurerement of the temperatures with PT100 thermometers, which are more precise than thermocouples type K. The temperature and potential at the electrolyte sites should be measured and not calculated (as it was the case in this study). Care should be taken when assembling these measuring devices, as it has already been reported in the literature, that they might hinder the mass/charge transport and disturb the chemical reaction. As for the mono-polar plates, it is important to design them especially for these experiments; the flow fields should be optimized for the experimental procedure. The groove between plate surface area and flow field should be reduced or eliminated, and the assembly should form, together with the sealing, a gas-tight housing, so that the membranes cannot exchange water/humidity with the ambient air.
The PEM test cell ought to be especially designed for the EIS characterisation. Stacking even a small amount of membranes to form a thick electrolyte introduces contact resistances that disturb the measurement. The resistance can be reduced by increasing the pressing pressure, but if the pressure is too high the GDL are too much compressed and obstruct the gas transport from electrode to the TPB. As stated for the solid oxide electrolyte, it is desirable to self design the membranes, so that thick membranes of $d > 1$ mm can be obtained. The coupling effect can also be enlarged by reducing the thermal conductivity of the polymer. Moreover, the selection of the GDL should be considered of vital importance, since the water transport in the membrane is coupled to the water transport in the GDL. In the experiments it was not possible to choose other GDLs than the ones used because of the grooves present in the mono polar plates. The carbon cloth in the given thickness creates an electric resistance three times larger than carbon paper and the diffusion resistance could go as high as ten times more. Furthermore, the activation of the chemical reactions has been considered to be negligible when compared to the losses in the electrolyte due to the platinum density of the catalyst layer. This assumption ought to be verified. Finally, the test cells could be pre-pressed in order to reduce the contact resistance, as it is common practice

in carbon paper based fuel cell engineering.
The experimental determination of transport coefficients in electrolytes, and moreover, in all other components such as gas diffusion median and catalyst layers, is vital to locate and reduce fuel cell losses, which allows an optimal design of fuel cells, making them more attractive for commercial use. The idea of measuring them by means of an inexpensive and relative easy technique as the Impedance Spectroscopy remains attractive and should be broadened and enhanced, considering the problems encountered and described in this work. Alternative technologies to fossil-based and established devices/power plants ought to be not only carbon neutral, greenhouse gases free but also efficient. Fuel cells are no exception as they still show some room for improvement when accurate modeling and precise experimental analysis extracts the avoidable irreversibilities.

Bibliography

[1] S. Mohr, J. Wang, G. Ellem, J. Ward, and D. Giurco. "Projection of world fossil fuels by country". In: *Fuel* 141 (2015), pp. 120–135.

[2] N. Abas, A. Kalair, and N. Khan. "Review of fossil fuels and future energy technologies". In: *Futures* 69 (2015), pp. 31–49.

[3] J. Neumann. "Climatic change as a topic in the classical Greek and Roman literature". In: *Climatic Change* 7.1 (1985), pp. 441–454.

[4] A. A Chan, G. Clancey, and H. Loy. *Historical Perspectives On East Asian Science, Technology And Medicine*. World Scientific Publishing Company, 2002.

[5] C. J. Glacken. *Traces on the Rhodian Shore*. Berkeley: University of California Press, 1976.

[6] P. S. Arrhenius. "XXXI. On the influence of carbonic acid in the air upon the temperature of the ground". In: *The London, Edinburgh, and Dublin Philosophical Magazine and Journal of Science* 41.251 (1896), pp. 237–276.

[7] N. Stenhouse, E. Maibach, et al. "Meteorologists' views about global warming: A survey of American meteorological society professional members". In: *Bulletin of the American Meteorological Society* 95.7 (2014), pp. 1029–1040.

[8] K. F. Hünemörder. *Die Frühgeschichte der globalen Umweltkrise und die Formierung der deutschen Umweltpolitik (1950 - 1973)*. Franz Steiner Verlag, 2004.

[9] E. Robinson and R. Robbins. *Sources, abundance, and fate of gaseous atmospheric pollutants. Final report and supplement*. Stanford Research Institute, 1968.

[10] J. Hovi, D. F. Sprinz, and G. Bang. "Why the United States did not become a party to the Kyoto Protocol: German, Norwegian, and US perspectives". In: *European Journal of International Relations* 18.1 (2012), pp. 129–150.

[11] I. Tiseo. *Carbon dioxide (CO2) emissions in the European Union from 1965 to 2020*. 2021. URL: https://www.statista.com/statistics/450017/co2-emissions-europe-eurasia/ (visited on 11/28/2021).

[12] T. E. Springer, T. A. Zawodzinski, and S. Gottesfeld. "Polymer Electrolyte Fuel Cell Model". In: 138.8 (1991), pp. 2334–2342. URL: https://doi.org/10.1149/1.2085971.

[13] S. Kjelstrup, D. Bedeaux, E. Johannessen, and J. Gross. *Non-equilibrium thermodynamics for engineers*. World Scientific Publishing, 2010.

[14] S. Kjelstrup and D. Bedeaux. *Non-equilibrium thermodynamics of Heterogeneous Systems*. World Scientific Publishing, 2008.

[15] T. Marquardt, G. Valadez-Huerta, and S. Kabelac. "Modeling a thermocell with proton exchange membrane and hydrogen electrodes". In: *International Journal of Hydrogen Energy* 43.43 (2018), pp. 19841–19850.

[16] T. Marquardt, J. Kube, P. Radici, and S. Kabelac. "Experimental investigation of a thermocell with proton exchange membrane and hydrogen electrodes". In: *International Journal of Hydrogen Energy* 45.23 (2020), pp. 12680–12690.

[17] J. R. Macdonald. *Impedance Spectroscopy Emphasizing Solid Materials and Systems*. John Wiley and Sons, Inc., 1987.

[18] S. K. und R. Hanke-Rauschenbach. Brennstoffzellen und Wasserelektrolyse. Lecture at the Leibniz University Hannover. 2018.

[19] H. Baehr and S. Kabelac. *Thermodynamik*. Springer-Lehrbuch. Springer Berlin Heidelberg, 2006.

[20] URL: https://i.pinimg.com/originals/ba/f5/27/baf527e72afaa8c9672c9b8f-2785bbb1.jpg (visited on 11/15/2021).

[21] X. Li and I. Sabir. "Review of bipolar plates in PEM fuel cells: Flow-field designs". In: *International Journal of Hydrogen Energy* 30.4 (2005), pp. 359–371.

[22] F. Barbir. *PEM Fuel Cells*. 2005.

[23] R. O'hayre, S.-W. Cha, F. B. Prinz, and W. Colella. *Fuel cell fundamentals*. John Wiley & Sons, 2016.

[24] P. Atkins. *Physikalische Chemie*. VCH, 1988.

[25] P. Heitjans and J. Kärger, eds. *Diffusion in condensed matter: Methods, materials, models*. Springer Verlag Berlin Heidelberg, 2005, pp. 210–222.

[26] S. Kjelstrup, P. Vie, L. Akyalcin, P. Zefaniya, J. Pharoah, and O. Burheim. “The Seebeck coefficient and the Peltier effect in a polymer electrolyte membrane cell with two hydrogen electrodes”. In: *Electrochimica Acta* 99 (2013), pp. 166–175.

[27] L. Onsager. “Reciprocal relations in irreversible processes. I.” In: *Physical Review* 37.4 (1931), pp. 405–426.

[28] L. Onsager. “Reciprocal relations in irreversible processes. II”. In: *Physical Review* 38.12 (1931), pp. 2265–2279.

[29] O. Burheim, P. J. S. Vie, J. G. Pharoah, and S. Kjelstrup. “Ex situ measurements of through-plane thermal conductivities in a polymer electrolyte fuel cell”. In: *Journal of Power Sources* 195.1 (2010), pp. 249–256.

[30] S. Brunauer, P. H. Emmett, and E. Teller. “Adsorption of Gases in Multimolecular Layers”. In: *Journal of the American Chemical Society* 60.2 (1938), pp. 309–319.

[31] J. Hollmann. “Experimentelle Validierung und Erweiterung eines Modells zur Beschreibung des Betriebsverhaltens einer umkehrbaren Festoxidzelle (ReSOC)”. Case study/Studienarbeit. Leibniz University Hannover, 2018.

[32] W. Choi, H.-C. Shin, J. Kim, J.-Y. Choi, and W.-S. Yoon. “Modeling and Applications of Electrochemical Impedance Spectroscopy (EIS) for Lithium-ion Batteries”. In: *Journal of Electrochemical Science and Technology* 11.1 (2020), pp. 1–13.

[33] B.-K. Lee, Y.-H. Yu, et al. “Electrical characterization of the platinum/YSZ interfaces in SOFCs via micro-contact impedance spectroscopy”. In: *Journal of Electroceramics* 17 (2006), pp. 735–739.

[34] M. Schönleber and E. Ivers-Tiffée. “Approximability of impedance spectra by RC elements and implications for impedance analysis”. In: *Electrochemistry Communications* 58 (2015), pp. 15–19.

[35] H. Huang, M. Nakamura, P. Su, R. Fasching, Y. Saito, and F. B. Prinz. “High-Performance Ultrathin Solid Oxide Fuel Cells for Low-Temperature Operation”. In: 154.1 (2007), B20.

[36] S. Fop. “Solid oxide proton conductors beyond perovskites”. In: *Journal of Materials Chemistry A* 9.35 (2021), pp. 18836–18856.

[37] G. V. Huerta, A. Kelle, and S. Kabelac. “A phenomenological study of yttria-stabilized zirconia at 1300 K with the Green-Kubo formulation and equilibrium molecular dynamics”. In: *Chemical Physics* 485 (2017), pp. 108–117.

[38] N. Geesmann. “Modellierung des elektrochemischen Verhaltens eines Festoxidelektrolyten für SOFC Anwendungen”. Bachelor thesis. Leibniz University Hannover, 2019.

[39] S.-H. Guan and Z.-P. Liu. “Theoretical aspects on doped-zirconia for solid oxide fuel cells: From structure to conductivity”. In: *Chinese Journal of Chemical Physics* 34.2 (2021), pp. 2334–2342.

[40] M. Aldesoki. “Elektrische und mechanische Eigenschaften von Yttrium stabilisiertem Zirkoniumoxid (3YSZ)”. Bachelor thesis. Leibniz University Hannover, 2020.

[41] A. Brune, M. Lajavardi, D. Fisler, and J. Wagner. “The electrical conductivity of yttria-stabilized zirconia prepared by precipitation from inorganic aqueous solutions”. In: *Solid State Ionics* 106 (2015), pp. 89–101.

[42] S. Heiroth, T. Lippert, A. Wokaun, M. Döbeli, J. Rupp, B. Scherrer, and L.J.Gauckler. “Yttria-stabilized zirconia thin films by pulsed laser deposition: Microstructural and compositional control”. In: *Journal of the European Ceramic Society* 30 (2010), pp. 489–495.

[43] B. Scherrer, M. Schlupp, et al. “On Proton Conductivity in Porous and Dense Yttria Stabilized Zirconia at Low Temperature”. In: *Advanced Functional Materials* 23 (15 2012), pp. 1957–1964.

[44] J.-H. Ryu, H.-S. Kil, J.-H. Song, D.-Y. Lim, and S.-B. Cho. “Glycothermal synthesis of 3 mol% yttria stabilized tetragonal ZrO2 nano powders at low temperature without mineralizers”. In: *Powder Technology* 221 (2012), pp. 228–235.

[45] U. Abend, X. Huang, and W. Weppner. “Electrical and Structural Modifications of TZP”. In: *Ionics* 3 (1997), pp. 426–435.

[46] D. Daiki Etoh, T. Takashi Tsuchiya, M. Takayanagi, T. Higuchi, and K. Terabe. “Oxide ion and proton conduction controlled in nano-grained yttria stabilized ZrO2 thin films prepared by pulse laser deposition”. In: *Japanese Journal of Applied Physics* 58 (2019).

[47] P. Duran, P. Recio, J. R. Jurado, C. Pascual, F. Capel, and C. Moure. “Y (E)-doped tetragonal zirconia polycrystalline solid electrolyte”. In: *Journal of materials science* 24.2 (1989), pp. 717–725.

[48] M. Weller and H. Schubert. “Internal Friction, Dielectric Loss, and Ionic Conductivity of Tetragonal ZrO2-3% Y2O3 (Y-TZP)”. In: *Journal of the American Ceramic Society* 69 (1986), pp. 573–577.

[49] R. Ramamoorthy, D. Sundararaman, and S. Ramasamy. “Ionic conductivity studies of ultrafine-grained yttria stabilized zirconia polymorphs”. In: *Solid State Ionics* 123 (1999), pp. 271–278.

[50] V. Srdić and R. Omorjan. “Electrical Conductivity of Sol–Gel Derived Yttria-Stabilized Zirconia”. In: *Ceramics International* 27 (2001), pp. 859–863.

[51] Y. Chen, L. Zhang, Y. Zhang, H. Gao, and H. Yan. “Large-area perovskite solar cells – a review of recent progress and issues”. In: *RSC Advances* 8 (2018), pp. 10489–10508.

[52] P. Lacorre, A. Selmi, G. Corbel, and B. Boulard. “On the flexibility of the structural framework of cubic LAMOX compounds, in relationship with their anionic conduction properties”. In: *Inorganic Chemistry* 45.2 (2006), pp. 627–635.

[53] T. Gottschalk. “Modellierung des elektrochemischen Verhaltens einer Polymerelektrolytmembra unter Berücksichtigung der Thermodynamik irreversibler Prozesse”. Master thesis. Leibniz University Hannover, 2020.

[54] L. Vasquez. *Fuel cell research trends*. 2007, pp. 1–486.

[55] P. S. Kumar and C. F. Carolin. “Polymer Electrolyte Membranes”. In: *Diffusion Foundations* 23 (Sept. 2019), pp. 82–89.

[56] T. A. Zawodzinski, M. Neeman, L. O. Sillerud, and S. Gottesfeld. “Determination of water diffusion coefficients in perfluorosulfonate ionomeric membranes”. In: *The Journal of Physical Chemistry* 95.15 (1991), pp. 6040–6044.

[57] J. T. Hinatsu, M. Mizuhata, and H. Takenaka. “Water Uptake of Perfluorosulfonic Acid Membranes from Liquid Water and Water Vapor”. In: 141.6 (1994), pp. 1493–1498.

[58] T. F. Fuller and J. Newman. “Experimental Determination of the Transport Number of Water in Nafion 117 Membrane”. In: *Journal of The Electrochemical Society* 139.5 (1992), pp. 1332–1337.

[59] T. Zawodzinski, J. Davey, J. Valerio, and S. Gottesfeld. “The water content dependence of electro-osmotic drag in proton-conducting polymer electrolytes”. In: *Electrochimica Acta* 40.3 (1995), pp. 297–302.

[60] L. M. Sánchez. “Experimental characterization of water sorption and transport properties of polymer electrolyte membranes for fuel cells”. Dissertation. 2012. URL: `https://hal.univ-lorraine.fr/tel-02074195`.

[61] M. Siemer. “Lokale Entropieproduktionsraten in der Polymerelektrolyt-Membran-Brennstoffzelle”. Dissertation. 2007.

[62] W. Neubrand. “Modellbildung und Simulation von Elektromembranverfahren”. Dissertation. 1999.

[63] J. Peron, A. Mani, et al. “Properties of Nafion® NR-211 membranes for PEMFCs”. In: *Journal of Membrane Science* 356.1-2 (2010), pp. 44–51.

[64] S.-A. Samaei, G. Bakeri, and M. Lashkenari. “Performance of the sulfonated poly ether ether ketone proton exchange membrane modified with sulfonated polystyrene and phosphotungstic acid for microbial fuel cell applications”. In: *Journal of Applied Polymer Science* 138.20 (2021).

[65] P. Radici, G. Valadez Huerta, N. Geesmann, and S. Kabelac. “A novel method to determine the transport coefficients of an YSZ electrolyte based on impedance spectroscopy”. In: *Solid State Ionics* 363 (2021).

[66] R. Hölzle. *Elektrokeramische Materialien: Grundlagen und Anwendungen.* Vol. B1. Jülich Forsch-ungszentrum, 1995, pp. 1–14.

[67] S. Thiemann, R. Hartung, H. Wulff, J. Klimke, H.-H. Möbius, U. Guth, and U. Schönauer. “Modified Au/YSZ electrodes - Preparation, characterization and electrode behaviour at higher temperatures”. In: *Solid State Ionics* 86-88.PART 2 (1996), pp. 873–876.

[68] B. van Hassel, B. Boukamp, and A. Burggraaf. “Electrode polarization at the Au, O2 (g) / yttria stabilized zirconia interface. Part II: electrochemical measurements and analysis”. In: *Solid State Ionics* 48.1-2 (1991), pp. 155–171.

[69] M. Rösch, G. Reinhardt, and W. Göpel. “In-situ spectroscopic investigations of silver electrodes on stabilized zirconia”. In: *Solid State Ionics* 136-137 (2000), pp. 791–799.

[70] A. Momma, H. Numata, and S. Haruyama. “Study of the mechanism of YSZ/metal, O2 electrode by the application of harmonics current measurement”. In: *Nippon Seramikkusu Kyokai Gakujutsu Ronbunshi/Journal of the Ceramic Society of Japan* 101.1172 (1993), pp. 410–415.

[71] M. E.-S. Ali, O. A. Abdelal, and A. A. Hassan. “Impedance spectroscopy of YSZ electrolyte containing CuO for various applications”. In: *Solid State Ionics* 178.25 (2007), pp. 1463–1466.

[72] P. Mondal, A. Klein, W. Jaegermann, and H. Hahn. “Enhanced specific grain boundary conductivity in nanocrystalline Y2O3-stabilized zirconia”. In: *Solid State Ionics* 118.3 (1999), pp. 331–339.

[73] X. Guo and Z. Zhang. “Grain size dependent grain boundary defect structure: case of doped zirconia”. In: *Acta Materialia* 51 (2003), pp. 2539–2547.

[74] F. Ciacchi, K. Crane, and S. Badwal. “Evaluation of commercial zirconia powders forsolid oxide fuel cells”. In: *Solid State Ionics* 73.1 (1994), pp. 49–61.

[75] F. Boulc’h, L. Dessemond, and E. Djurado. “Dopant size effect on structural and transport properties of nanometric and single-phased TZP”. In: *Solid State Ionics* 154-155 (2002), pp. 143–150.

[76] G. Valadez-Huerta, V. Flasbart, T. Marquardt, P. Radici, and S. Kabelac. “Impact of Multi-Causal Transport Mechanisms in an Electrolyte Supported Planar SOFC with (ZrO2)x1(Y2O3)x Electrolyte”. In: *Entropy* 20 (2018), p. 469.

[77] G. Valadez Huerta, M. Siemen, and S. Kabelac. “Approach to the Coulomb Contribution of Thermodynamic Properties from the Mean Electrostatic Potential of the Ions in (ZrO2)1-x(Y2O3)x”. In: *Journal of Physical Chemistry C* 122.1 (2018), pp. 62–70.

[78] I. Valov, V. Rührup, et al. “Ionic and electronic conductivity of nitrogen-doped YSZ single crystals”. In: *Solid State Ionics* 180.28 (2009), pp. 1463–1470.

[79] M. Kilo, M. Taylor, et al. “Modeling of cation diffusion in oxygen ion conductors using molecular dynamics”. In: *Solid State Ionics* 175.1 (2004), pp. 823–827.

[80] P. Heitjans and S. Indris. “Diffusion and ionic conduction in nanocrystalline ceramics”. In: *Journal of Physics Condensed Matter* 15.30 (2003), R1257–R1289.

[81] T. Arima, S. Yamasaki, Y. Inagaki, and K. Idemitsu. “Evaluation of thermal properties of UO2 and PuO2 by equilibrium molecular dynamics simulations from 300 to 2000K”. In: *Journal of Alloys and Compounds* 400.1 (2005), pp. 43–50.

[82] T. Arima, S. Yamasaki, K. Yamahira, K. Idemitsu, Y. Inagaki, and C. Degueldre. “Evaluation of thermal conductivity of zirconia-based inert matrix fuel by molecular dynamics simulation”. In: *Journal of Nuclear Materials* 352.1 (2006), pp. 309–317.

[83] S. Ikeda, O. Sakurai, K. Uematsu, N. Mizutani, and M. Kato. “Electrical conductivity of yttria-stabilized zirconia single crystals”. In: *Journal of Materials Science* 20.12 (1985), pp. 4593–4600.

[84] S. Niya and M. Hoorfar. “Process modeling of the ohmic loss in proton exchange membrane fuel cells”. In: *Electrochimica Acta* 120 (2014), pp. 193–203.

[85] A. Lasia. *Electrochemical impedance spectroscopy and its applications*. Springer, 2014, pp. 1–367.

[86] S. Rezaei Niya and M. Hoorfar. “Process modeling of electrodes in proton exchange membrane fuel cells”. In: *Journal of Electroanalytical Chemistry* 747 (2015), pp. 112–122.

[87] S. Kjelstrup, P. Pugazhendi, and D. Bedeaux. “Impedance of the hydrogen polymer fuel cell electrode. theory and experiments”. In: *Zeitschrift fur Physikalische Chemie* 214.7 (2000), pp. 895–916.

[88] D. Malevich, E. Halliop, B. Peppley, J. Pharoah, and K. Karan. “Effect of Relative Humidity on Electrochemical Active Area and Impedance Response of PEM Fuel Cell”. In: *ECS Transactions* 16 (2008), pp. 1763–1774.

[89] T. Kadyk, R. Hanke-Rauschenbach, and K. Sundmacher. “Nonlinear frequency response analysis of PEM fuel cells for diagnosis of dehydration, flooding and CO-poisoning”. In: *Journal of Electroanalytical Chemistry* 630.1 (2009), pp. 19–27.

[90] M. Siemer, T. Marquardt, G. Huerta, and S. Kabelac. “Local entropy production rates in a polymer electrolyte membrane fuel cell”. In: *Journal of Non-Equilibrium Thermodynamics* 42.1 (2017), pp. 1–30.

[91] S. Rezaei Niya, R. Phillips, and M. Hoorfar. “Process modeling of the impedance characteristics of proton exchange membrane fuel cells”. In: *Electrochimica Acta* 191 (2016), pp. 594–605.

[92] F. Bernhard, ed. *Handbuch der Technischen Temperaturmessung*. VDI-Buch. Springer-Verlag Berlin Heidelberg, 214.

[93] A. Toghan, M. Khodari, F. Steinbach, and R. Imbihl. “Microstructure of thin film platinum electrodes on yttrium stabilized zirconia prepared by sputter deposition”. In: *Thin Solid Films* 519.22 (2011), pp. 8139–8143.

[94] M. Meyer. “Experimentelle Untersuchung eines elektrochemischen Energiewandlers mit zwei Wasserstoffselektroden”. Bachelor thesis. Leibniz University Hannover, 2020.

[95] J. Reißner. “Konzeptionierung, Aufbau und Inbetriebnahme eines Versuchsstands zur experimentellen Untersuchung eines thermoelektrochemischen Energiewandlers mit zwei Waserstoffelektroden”. Bachelor thesis. 2021.

[96] URL: `https://www.lean-cat.com/testing-equipment-services/single-cell-5-50` (visited on 10/10/2021).

[97] M. Khandelwal and M. M. Mench. “Direct measurement of through-plane thermal conductivity and contact resistance in fuel cell materials”. In: *Journal of Power Sources* 161.2 (2006), pp. 1106–1115.

[98] M. Grundmann. *The physics of semiconductors: An introduction including devices and nanophysics*. 2006, pp. 1–689.

[99] H. Morkoç and U. Özgür. *Zinc Oxide: Fundamentals, Materials and Device Technology*. 2009, pp. 1–477.

[100] S. K. Ratkje and Y. Tomii. "Transported Entropy in Zirconia with 3 to 12 Mole Percent Yttria". In: *Journal of The Electrochemical Society* 140.1 (1993), pp. 59–66.

[101] A. Kosakian, L. Urbina, A. Heaman, and M. Secanell. "Understanding single-phase water-management signatures in fuel-cell impedance spectra: A numerical study". In: *Electrochimica Acta* 350 (2020).

[102] M. Ottøy. "Mass and Heat Transfer in Ion-Exchange Membranes Applicable to Solid Polymer Fuel Cells". Dissertation. 1996. URL: `https://www.osti.gov/etdeweb/servlets/purl/527379`.

[103] L. Yang, H. Sun, S. Wang, L. Jiang, and G. Sun. "A solid state thermogalvanic cell harvesting low-grade thermal energy". In: *International Journal of Hydrogen Energy* 42.41 (2017), pp. 25877–25881.

Appendix A

Appendix

A.1 Parameters from the fitting for 3YSZ, d=5 mm

Table A.1: Passive elements in Ω or F

element	$T = 373$	$T = 500$	$T = 600$
R1	44969	30080	7212
C1	1,82E-06	3.59E-08	2,74E-09
R2	80371	64676	14693
C2	$2.17E-10$	2,83E-10	6,34E-09
R3	20735	24510	930,3
C3	1,82E-06	2,83E-10	2,74E-09

A.2 Parameters from the fitting for 3YSZ, d=10 mm

Table A.2: Passive elements Ω or F

element	$T = 373$	$T = 500$	$T = 600$
R1	47294	25352	11067
C1	1,31E-09	5,12E-08	9,29E-10
R2	87507	66018	16217

C2	1,8047E-10	1,19E-09	6,46E-09
R3	13790,9	30249	6089,8
C3	1,38E-10	2,0485E-10	2,72E-10

A.3 Resistance differences for 3YSZ

Differences in resistance and temperature used to calculate the conductivity L_{Oq}.

Table A.3: Resistance difference in Ω, temperature difference in K

T in K	d in m	ΔR	ΔT
500	5,00E-03	7392	8,64
500	5,00E-03	14234	19,08
600	5,00E-03	2662,6	8,05
600	5,00E-03	4107,9	16,22
500	1,00E-02	4642	9,92
500	1,00E-02	9231	18,08
600	1,00E-02	2798	7,53
600	1,00E-02	7285,9	17,15